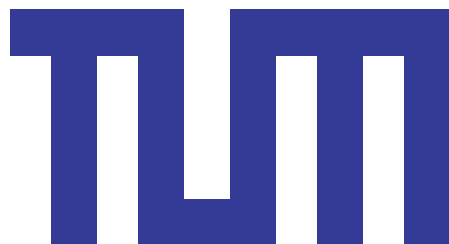


TECHNISCHE UNIVERSITÄT MÜNCHEN

Physik-Department: ENE, Teilchenphysik bei niedrigen Energien

The N4DP Instrument

Lukas Werner



TECHNISCHE UNIVERSITÄT MÜNCHEN

Physik-Department ENE Teilchenphysik bei niedrigen Energien

The N4DP Instrument

Lukas Werner

Vollständiger Abdruck der von der Fakultät für Physik der Technischen Universität München zur Erlangung des akademischen Grades eines

Doktors der Naturwissenschaften (Dr. rer. nat.)

genehmigten Dissertation.

Vorsitzender: Prof. Dr. Andreas Weiler

Prüfer der Dissertation: 1. Prof. Dr. Bastian Märkisch
2. Prof. Dr. Lothar Oberauer

Die Dissertation wurde am 17.08.2020 bei der Technischen Universität München eingereicht und durch die Fakultät für Physik am 28.09.2020 angenommen.

Zusammenfassung

Die zerstörungsfreie, nukleare Neutronentiefenprofilanalyse (NDP) ist hervorragend geeignet, um Dünnschichtsysteme, die bestimmte Elemente wie Lithium und Bor enthalten, zu analysieren. Der hohe Wirkungsquerschnitt für den Neutroneneinfang an Lithium erlaubt Präzisionsstudien an selbst kleinsten Mengen. NDP ermöglicht eine hervorragende Tiefenauflösung bis zu 10 nm. Die Analysetechnik erlaubt es, dünne Schichten mit dicken im μm -Bereich zu untersuchen. Dies macht NDP zu einem mächtigen Werkzeug zur Studie von beispielsweise Lithiumionenbatterien.

Im Rahmen dieser Arbeit wurde das N4DP Instrument entworfen, gebaut und an der Forschungsneutronenquelle (FRM II) des Heinz-Maier-Leibnitz Zentrums (MLZ) in Betrieb genommen. NDP erfordert eine hohe Neutronenflussdichte, welche der Strahlplatz der Prompten Gamma Aktivierungsanalyse (PGAA) des FRM II liefert. Das Design des Instruments ermöglicht ein hervorragendes Signal zu Untergrund Verhältnis. Dieses hochmoderne N4DP Instrument wurde bereits erfolgreich in mehreren Messkampagnen eingesetzt. Hier ist die erste *operando* Messung mit Flüssigelektrolytbatterien am N4DP Instrument hervorzuheben.

Im nächsten Entwicklungsschritt wird das Instrument zeit- und orts aufgelöste NDP ermöglichen. Hierfür wurden, im Rahmen dieser Arbeit, Ausleseelektronik sowie Detektoren entwickelt. Die selbstentwickelte Elektronik, Firmware und Software erlauben Zeit und positionsaufgelöste (4D) NDP Messungen mit der selben Tiefenauflösung, die im klassischen NDP System erreicht wurde.

Abstract

The non-destructive nuclear analytical technique of Neutron Depth Profiling (NDP) is uniquely suited to probe thin layer structures containing certain elements, like lithium or boron. The high reaction cross section for neutrons with lithium enables precision studies even of trace amounts. With NDP good depth resolution down to 10 nm is achieved. The technique is well suited for layer thicknesses in the μm -range, thereby making NDP an excellent tool to study, for example, lithium ion batteries.

In the scope of this thesis, the N4DP instrument was designed, built and set up at the Forschungsneutronenquelle (FRM II) of the Heinz-Maier-Leibnitz Zentrum (MLZ). The intense neutron beam required for NDP is provided by the Prompt-Gamma-Activation-Analysis (PGAA) beamline of the FRM II. The design of the instrument allows for an excellent signal-to-background ratio, thereby pushing down the detection threshold for trace amounts of isotopes. This state of the art NDP instrument has been used successfully in several experimental campaigns. One prominent example is the first *operando* measurement of liquid electrolyte lithium ion batteries at the N4DP instrument.

In the next development stage, the instrument will provide time resolved, position sensitive NDP. To achieve these goals, readout electronics and detectors have been developed in the scope of this thesis. The custom made electronics, firmware and software developed for this purpose enable time and position resolved (4D) NDP while providing the same depth resolution as the classical NDP setup.

Contents

1. Introduction	1
2. Neutron Depth Profiling (NDP)	3
2.1. Basics of NDP	3
2.2. Cold neutron capture	5
2.3. Energy loss	9
2.4. Experimental limitations	11
2.5. Application examples	13
3. The N4DP Instrument	15
3.1. The experimental Site	15
3.2. Chamber Design	16
3.3. Sample/Target Stage	19
3.4. Instrument Control	19
3.5. Detectors and Electronics	21
4. N4DP: Performance with surface barrier detectors	23
4.1. Background	23
4.2. Calibration	27
4.3. Energy and Depth Resolution	30
4.4. Systematic Uncertainties	33
5. Measurements and analysis at the N4DP instrument	37
5.1. Borofloat glasses	37
5.2. Cobalt-rhenium based superalloys	38
5.3. Lithium ion batteries	40
5.4. Prussian blue analog based batteries	44
6. Position resolved (4D) NDP	47
6.1. Position resolved NDP	47
6.2. 4D implementation at the N4DP instrument	48
7. Electronics for position resolved measurements at the N4DP instrument	51
7.1. The SKIROC ICs	51
7.2. Hardware implementation	54
7.3. Firmware: Controlling and readout of the SKIROCs	56
7.4. Performance	61
8. Detector for 4D NDP	69
8.1. Detector performance needed for N4DP	69
8.2. Commercially available silicon strip detectors	71

8.3. Prototypes	73
9. Summary and Outlook	75
A. List of Publications	79
B. Slowcontrol Registers	81
C. Additional Figures for Chapter 7	95

1. Introduction

Free neutrons, as electrically neutral particles interact with matter significantly different than for example protons. This means, that neutrons are able to penetrate even thick layers of dense materials, like lead. Free neutrons are usually produced in reactors or in spallation sources. Often-times these neutrons are then slowed down before they are used in experiments. This slow down results in a number of different neutron temperatures (energies) which are available at scientific neutron sources. The neutrons mass (939.5654 MeV) will lead to *de-Broglie* wave lengths for thermal neutrons ($E \approx 0.025$ eV) of $\lambda \approx 2$ Å. The typical wave lengths, the nature as a heavy, electrically neutral particle, and the unique scattering and absorption cross sections (high for several light elements, low for some very heavy elements) make neutrons ideally suited for material analysis techniques.

The non-destructive nuclear analytical technique of Neutron Depth Profiling (NDP) is well suited for the investigation of thin layer structures using neutrons. The NDP active elements lithium and boron have a high significance as active and passive materials in many industrial applications, like lithium ion batteries. Combined with the relatively low cross sections for neutrons with other materials commonly used in such applications, like carbon, this makes NDP well suited for isotope specific probing of such samples.

The nuclear reactions on which NDP is based (the most important are listed in Table 2.2), such as the ${}^6\text{Li}(n,\alpha){}^3\text{H}$ reaction provide unique advantages. The charged particles produced in NDP reactions quickly lose energy when passing through matter (in most solids they are stopped within the first few μm). The neutrons momentum is negligible, when compared with the momentum of the ejected particles, meaning that the particles are effectively produced in a two body decay, and therefore with known energies. The energy loss experienced by such a charged particle can be determined straightforward by measuring the remaining energy. If sufficient information about the traversed material is available, the production depth of the particle can be determined (as detailed in Chapter 2). Thereby a depth profile of NDP active isotopes can be determined.

When compared with other material analysis techniques, NDP occupies a specific niche. It allows for depth resolutions in the 10 nm region. While these are surpassed by techniques such as Secondary-Ion-Mass-Spectroscopy (SIMS) and Elastic-Rutherford-Backscattering (ERB), NDP offers a wider accessible depth range, and has the advantage of being non-destructive, thereby enabling further investigation of the samples or even performing measurements on *operando* samples. The high cross sections for NDP specific reactions, combined with the efficiencies possible in charged particle detection, allow for the detection of even trace amounts of NDP isotopes within a sample. Therefore NDP is well suited for the investigation of lithium based energy storage systems.

Planned phase-out of fossil fuel based energy generation, as well as the shift to power creation via intermittent, renewable systems is one of the main motivations for the further development of lithium based energy storage systems [Che09, Age18]. While it is still not clear how large scale energy storage will be performed (aqueous alkali batteries are possible candidates, see Section 5.4

and [Che09, Kim14]), the high energy density achievable in lithium ion batteries make them the system of choice for mobile applications (mobile phones, laptops, electric cars) [Arm08, Tar01].

In the scope of this thesis a new NDP instrument, the N4DP instrument, for use at the Forschungsneutronenquelle München (FRM II) was developed, to aid with investigations into these pressing research topics. The instrument is designed for use with the powerful cold neutron source of the FRM II, and is deployed at the PGAA facility. The instrument itself is detailed in Chapter 3. The instrument control and the sample environment are detailed in the same chapter. The use of silicon surface barrier detectors together with custom-made high resolution electronics, enables depth resolutions in the 5 nm region. The achieved resolutions, alongside several other benchmarks and tests are detailed in Chapter 4.

Several measurements performed with the N4DP instrument are presented and analysed in Chapter 5. The chapter presents numerous different applications of NDP. Especially remarkable in this regard is the first *operando* NDP measurement of a liquid electrolyte based lithium ion battery [Lin20], which was performed at the N4DP instrument. This was possible due to the high neutron flux density at the instrument, the high signal-to-background ratio, the event-by-event data taking at the instrument, and due to a specialized battery design.

The second part of this thesis discusses the upgrade of the N4DP instrument to enable measuring position resolved depth profiles. Modern detector technologies enable the use of detectors which provide laterally resolved energy information in NDP applications. These detectors allow to add lateral position information to a depth profile, thereby providing 3D information on the isotope distribution in an investigated sample. Using time stamped data, even 4D measurements are possible. Several options of implementing such a capability are discussed in Chapter 6. As detailed in the same chapter, double-sided silicon microstrip detectors (DSSDs) provide the best option for 4D measurements at the N4DP instrument. The high signal densities inherent to such a design demand the use of highly integrated readout electronics. The choice of electronics, the implementation of the readout chain, and the performance of the resulting system are detailed in Chapter 7. The high performance electronics need to be combined with a well designed detector to provide optimal performance for the N4DP instrument. The characteristics needed for such a detector are detailed in Chapter 8. A commercially available detector is compared to the requirements using measurements performed with the new N4DP electronics, showing a performance not sufficient for high resolution NDP applications. The chapter concludes with measurements performed with a detector prototype specifically designed with the N4DP requirements in mind. As is shown the performance is comparable to the performance available with the current N4DP configuration.

2. Neutron Depth Profiling (NDP)

To understand the technique of NDP, it is first necessary to take a look at the underlying nuclear reactions. After a brief introduction into NDP, these reactions are dealt with in more detail in Section 2.2. General aspects of cold neutron capture reactions are discussed. A more detailed account of (n, α) reactions, using the so called cluster model, is given. Besides the underlying nuclear reactions, energy loss is a central part in understanding NDP. Section 2.3 presents some energy loss models commonly used to describe the energy loss of ions in matter. The chapter continues by dealing with some of the most important experimental limitations inherent to NDP. It concludes by briefly sketching some applications of NDP.

2.1. Basics of NDP

NDP is a non-destructive, nuclear, analytical technique which was first introduced in the 1970's by Ziegler et al. [Zie72]. Since then, NDP has been and is used at numerous neutron sources around the world. Table 2.1 presents some of these facilities. In general terms, NDP uses neutron capture reactions, which produce an excited, unstable compound nucleus. This nucleus then decays almost instantly into two charged particles. [Zie72]

Institution	Location	Neutron flux $\frac{n}{\text{cm}^2\text{s}}$	Route
NIST	Gaithersburg, MD, USA	$1.2 \cdot 10^9$	[Dow93]
CMRR	Mianyang, Sichuan, China	$2.1 \cdot 10^8$	[Li15]
HANARO	Daejeon, Republic of Korea	$1.8 \cdot 10^8$	[Par14]
NARS, Ohio State	Columbus, Ohio, USA	$1.2 \cdot 10^7$	[Mul12]
ÚJF, NPI	Řež, Czech Republic	$1 \cdot 10^7$	[Hav93]
FRM II, TUM	Garching, Munich, Germany	$5 \cdot 10^9$	[Wer18]

Table 2.1.: List of select NDP facilities around the world. Presented are institutions, geographical locations and the flux available at the instrument. List adapted from [Dow95]. The respective references are also listed

If the neutron does not carry significant kinetic energy (in the order of the thermal movement of the nucleus), the energy of the excited compound can be considered fixed. Therefore, the production reaction for the charged particles is, essentially, a decay of one mother nucleus into two daughter nuclei. Due to conservation of four-momentum, the energy of the daughter nuclei is constrained to fixed values. Furthermore, both particles have to be emitted back to back due to conservation of momentum. An illustration of this process for the ${}^6\text{Li}(n,\alpha)$ reaction can be seen in Fig. 2.1.

Cross sections for neutron capture reactions follow a $\frac{1}{\sqrt{E}}$ energy dependence [MK84]. As discussed in more detail in Section 2.2, it is preferable to use slow neutrons in capture reactions. Therefore cold neutrons are often used in NDP experiments [Dow93]. Since cross sections for

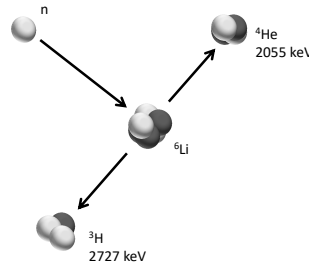


Figure 2.1.: Illustration of a NDP reaction. Displayed is a cold neutron reacting with a lithium nucleus. Due to the low energy of the neutron, the daughter particles are emitted back to back.

neutron capture reactions are typically well known (see for example [Dia03]), measuring the number of produced daughter nuclei can give an information on the number of mother nuclei in an irradiated target.

Correlating the observed count rate for certain daughter nuclei with the number of mother nuclei demands a precise knowledge of the (thermal equivalent) neutron flux density at the target position and of the acceptance and efficiency of the detector used to measure the charged daughter nuclei. Since all these numbers will have uncertainties, the overall measurement precision will suffer when using such an absolute measurement method. Therefore it is preferable to use a sample with a well known isotope distribution as a reference. Assuming a constant neutron flux, a comparison of the count rate observed from the reference sample with that of an unknown sample will provide a more precise measure of isotope concentrations in the unknown sample. Due to the thin nature of samples investigated in NDP (below $50\ \mu\text{m}$), attenuation of the neutron beam in the sample can usually be disregarded.

Besides the amount of mother nuclei, also the depth distribution of these can be measured. For this, emission energies of daughter nuclei have to be known precisely. If the charged particles are emitted from within a sample, they will lose energy when propagating out of this sample [Blo33]. This energy loss is dependent on the sample composition, the type of emitted charged particle, and the emission depth. Knowing the sample composition and density, as well as the emission energies of the particles, a depth profile can be approximated.

Experimentally, this is done by measuring the energy of the particles after they have left the sample. This is then compared to the emission energy of the particles from the mother nucleus, to determine the lost energy. Since the emitted particles are heavy, low-energy ions, measurements are usually done in vacuum, to minimize uncertainties from energy loss in air or gases.

2.2. Cold neutron capture

In neutron capture (which includes the reactions used in NDP), a (cold) neutron is captured by a mother nucleus (A), thereby forming a compound nucleus ($A+1$). For this to happen, the $A+1$ nucleus needs to have a state that can be populated by the free neutron (a state close to the vacuum energy of the neutron). The compound nucleus will be in an excited state, due to the binding energy of the neutron. The excitation energy E^* of this state can be computed straightforward as

$$E^* = m_A + m_n - m_{A+1} \quad (2.1)$$

with m_A the mass of the mother nucleus, M_n the neutron mass (939.5654 MeV), and m_{A+1} the mass of the compound nucleus. The excited $A + 1$ nucleus can either remove this excitation energy by emitting several γ rays, one or more charged particles, or by (re)emitting one or more neutron(s). The emission of γ rays will be highly characteristic for the involved nucleus and can be used to identify it, which is the basis of Prompt Gamma Activation Analysis, or PGAA (see for example [Rev15]).

For NDP active isotopes, the excitation energy is high enough to form two separate daughter nuclei from the compound nucleus. This gives a reaction of the type $A(n,b)B$, with the mother nucleus A and the daughter nuclei b and B . Q -values for these reactions are in the MeV range. Since cold neutron will only carry energies in the meV range, the neutrons energy can safely be neglected. Therefore, the computation of the Q -value of the reaction is straightforward:

$$Q = m_A + m_n - m_b - m_B + E_B^* \quad (2.2)$$

with the masses m_A , m_n , m_b and m_B and E_B^* as the excitation energy of the daughter nucleus (in NDP only α -particles and protons are emitted as b , therefore $E_b^* = 0$). For most NDP reactions E_B^* is zero. (A notable exception is the $^{10}\text{B}(n,\alpha)^7\text{Li}$ reaction.) Due to the mother nucleus being at rest and the neutron not carrying significant momentum, the overall momentum of the system is zero. Therefore, the products have to be emitted back-to-back. Knowing the masses of all involved nuclei, as well as the level schemes of the produced nuclei therefore allows calculation of the full kinematics of the reaction.

Using Fermi's golden rule, the dependency between the energy of the incoming neutron and the reaction cross section can be derived [MK84, pp. 248-252]):

$$\left(\frac{d\sigma}{d\Omega}\right) \propto \frac{1}{\sqrt{E}} \quad (2.3)$$

This can be understood intuitively by considering the wave-function of the free neutron. As shown by the optical theorem [MK84, p. 125], the wave-length of this particle is proportional to the reaction cross section. Since the wave-length is proportional to the inverse square root of the energy, Eq. (2.3) follows. Simply put, the slower the neutron is, the larger its wave function gets, thereby increasing the probability for interaction with the nucleus' wave-function.

2.2.1. (n, α) reactions and cluster models

Due to the constraints on the neutron capture reaction (two charged particles produced without other particles) NDP can only be used for a select few isotopes. The most important of those

isotopes are listed in Table 2.2. The two isotopes most often studied in NDP are ^{10}B and ^6Li . Both isotopes exist naturally in significant proportions. Both lithium and boron have significant applications in material science. Since both isotopes experience (n,α) -reactions, the following section aims to show how these reactions can be modelled, putting a special focus on the di-cluster model which can be used to describe the $^6\text{Li}(n,\alpha)^3\text{H}$ reaction.

To understand NDP type (n,α) reactions, it is useful to consider the moment right after the neutron has been captured by the mother nucleus. A compound nucleus is formed. In this nucleus, the captured neutron will be in a highly excited state. The energy of this state (4.78 MeV for the $^6\text{Li}(n,\alpha)^3\text{H}$ reaction) is given by the binding energy of this neutron when the compound nucleus is in its ground state, as described in Eq. (2.1).

The first calculations performed to describe complex nuclear reactions like fission (and (n,α) -reactions) have been based on the liquid drop model [Mei39, Boh39]. In this model, changes in the potential of the nucleus are described via deformation, shape and size changes of said nucleus. The potential energy is calculated using an analog to a liquid drop, with terms for surface tension, coulomb repulsion, nucleon-nucleon interaction, and many more. This approach was greatly successful in modeling complex nuclear reactions [Mol95, M  l09].

While the liquid drop model is able to describe complex reactions like fission, it fails in predicting some essential properties of nuclei, like the magic numbers. The so called shell-model [Cau05] has been developed to describe these properties. In it, a harmonic oscillator is assumed as the base potential for a nucleus and a shell structure similar to that of the electron configuration in atoms is calculated. Due to the strong spin-orbit interaction in the nucleus, the levels differ from those seen in atoms [Cor09, Cau05]. The nuclear shell model also differs from the atomic shell model, in the regard that a priori there is no distinction between the source of the central potential and the particles effected by it. This is solved in the nuclear shell model through a mean field approach. A central spherical symmetrical potential is assumed, and its effect on single nucleons (valence-nucleons) is calculated (similar to valence electrons in the atomic shell model) [Hax49].

Reaction	% Isot. Abundance	E_{em} [keV]	E_{rec} [keV]	σ_{therm} [barn]
$^3\text{He}(n,p)^3\text{H}$	0.00014	572	191	5333
$^6\text{Li}(n,\alpha)^3\text{H}$	7.5	2055	2727	940
$^{10}\text{B}(n,\alpha)^7\text{Li}$	19.9	1776	1013	241
$^{10}\text{B}(n,\alpha)^7\text{Li}^a$	19.9	1472	840	3600
$^{14}\text{N}(n,p)^{14}\text{C}$	99.6	584	42	1.83
$^{17}\text{O}(n,\alpha)^{14}\text{C}$	0.038	1413	404	0.24
$^{33}\text{S}(n,\alpha)^{30}\text{Si}$	0.75	3081	411	0.19
$^{35}\text{Cl}(n,p)^{35}\text{S}$	75.8	598	17	0.49
$^{40}\text{K}(n,p)^{40}\text{Ar}$	0.012	2231	56	4.4

Table 2.2.: Selected NDP reactions. Data taken from [Dow93]. E_{em} denotes the kinetic energy of the emitted particle, while E_{rec} is the kinetic recoil energy. σ_{therm} is the reaction cross section for thermal neutrons.

a: The ^7Li -nucleus is produced in an excited state (96 %-branching ratio). An additional 478 keV γ is emitted when it de-excites.

Since it is well known that nuclei can have many different, non spherical shapes, and that nuclei can deform, an extension of the shell model using non-spherical symmetric potentials can be a valid approach. An elongation of the nucleus along one axis will significantly change the closed shell configurations calculated from shell model approaches [Oer06]. This deformation and change in closed shell configurations is the basis of the cluster approach, which assumes the formation of clusters (for example α -particles) within certain nuclei [Oer06]. This approach is especially useful for understanding (n,α) -reactions, which can be explained by a deformation of the seed nucleus due to the excess energy brought into the system by the captured neutron. The deformation leads to the formation of clusters, which are only weakly bound to each other and can separate easily.

In the case of the ${}^6\text{Li}(n,\alpha){}^3\text{H}$ reaction, the Q-value of 4.78 MeV allows for a highly excited compound nucleus (at ca. 7.251 MeV). This comparably high excitation energy of the ${}^7\text{Li}$ compound nucleus makes the ${}^6\text{Li}(n,\alpha){}^3\text{H}$ reaction an interesting case study for di-cluster models [For05]. A possible potential to describe the interaction between the two clusters is:

$$V_{\alpha-t}(r) = V_C(r) + V_{WS}(r) + V_{\vec{l}\cdot\vec{s}}(r) \quad (2.4)$$

consisting of a Coulomb term V_C an attractive Wood-Saxon term V_{WS} and a spin-orbit term $V_{\vec{l}\cdot\vec{s}}$ [For05].

The first indication that ${}^7\text{Li}$ can be described in a di-cluster model is given by the large average distance between the α and triton constituents of the nucleus, that would be deduced in such a model [Wal85]. This average distance, calculated by treating the constituents as elementary but not point like particles has been determined to 3.5 fm [Wal85]. Taking α and triton particles as elementary is valid in the ${}^7\text{Li}$ nucleus, due to the high excitation energies of these constituents. No excited state is currently known for the triton particle, and the first excited state of the alpha particle lies 0.5 MeV above its proton separation energy at 20.2 MeV above the ground state [Pri11]. Since the separation energy for tritons and α - particles is considerably lower (≈ 2.5 MeV [Til02]), breakup of the nucleus will generally happen long before excitations of the clusters have to be considered.

This can be seen in particular when comparing calculations from models which assume elementary clusters with those that work with the constituent clusters treated as non-elementary (composed of several nucleons). Observables calculated with both theories agree very well [Wal85]. Agreement with experimentally obtained values is also good, and remains so for different choices of α -triton potentials [Buc88, For05]. Also the observed level scheme in ${}^7\text{Li}$ can be described successfully by using a di-cluster model. It predicts the $(\frac{1}{2})^-$ state at 478 keV [Wal85]. Also the higher energy states, $(\frac{7}{2})^-$ at 4.65 MeV and $(\frac{5}{2})^-$ at 6.6 MeV are predicted by the di-cluster model [For05]. The experimentally determined level scheme is displayed in Fig. 2.2.

Especially interesting in the ${}^6\text{Li}(n,\alpha){}^3\text{H}$ reaction is the question, if the high initial energy of the nucleus (at ≈ 7.2 MeV) allows for the emission of γ -radiation into the so-called continuum, the energy region above the breakup threshold of the nucleus. This emission would result in a missing energy in the reaction products, and could therefore be detected in a NDP setup. Since this emission is predicted by the di-cluster model of the ${}^7\text{Li}$ -nucleus described in [For05], it would allow for the verification of the model. We have proposed an experimental campaign to measure

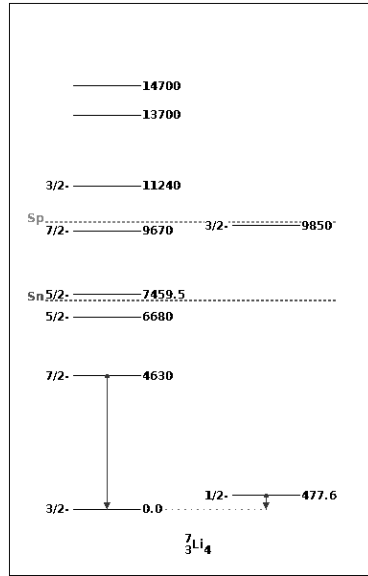


Figure 2.2.: Level scheme of ${}^7\text{Li}$. Proton and neutron separation energies are marked (S_p and S_n). Energies in keV. Taken from [Pri11].

branching ratios for the emission into the continuum¹.

Contrary to ${}^7\text{Li}$, the ${}^{11}\text{B}$ nucleus can not be described as a cluster of two elementary particles (${}^4\text{He}$ and ${}^7\text{Li}$). This is due to the low energy of the first excited state in the ${}^7\text{Li}$ nucleus, at 478 keV (see Fig. 2.2). Due to the Q-value of the ${}^{10}\text{B}(n,\alpha){}^7\text{Li}$ reaction (≈ 2790 keV) higher energy states in the ${}^7\text{Li}$ nucleus can not be populated. Therefore the ${}^{11}\text{B}$ nucleus in this regime is an example for a more complex system. Besides the shell model description for low energy states, a $2\alpha+t$ cluster model can be used to describe states with higher energies in the nucleus [Nis79, Kaw07, Kaw08]. This triple cluster model also helps in understanding the α -breakup of the ${}^{11}\text{B}$ nucleus. When the nucleus is excited, the three constituents will move relative to each other. If the excitation energy is high enough, one of the constituents can leave the nucleus. The $\alpha+t$ (${}^7\text{Li}$) subsystem is bound much stronger than a 2α (${}^8\text{Be}$) system would be (the ${}^8\text{Be}+t$ configuration is 2.5 MeV heavier than the ${}^7\text{Li}+\alpha$ configuration). Therefore a breakup into an α -particle and a ${}^7\text{Li}$ nucleus will occur. Due to the low energy excited state existing in a ${}^7\text{Li}$ nucleus (at 477.6 keV, see Fig. 2.2) it is possible to populate this state in the ${}^{10}\text{B}(n,\alpha){}^7\text{Li}$ reaction. The ${}^7\text{Li}$ nucleus is produced in this state in 96% of all cases, while in the rest of events the ${}^7\text{Li}$ nucleus is produced in its ground state [Kno00]. After production the $(\frac{1}{2})^-$ state decays via the emission of a γ -particle. These two branches in the ${}^{10}\text{B}(n,\alpha){}^7\text{Li}$ reaction therefore lead to different kinetic energies of the products, which can be detected in an NDP measurement [Dow93].

¹ Experimental campaigns have been performed at the PF1B beamline of the ILL. A follow up proposal to be performed at the N4DP instrument has been accepted by the MLZ's scientific board.

2.3. Energy loss

Since NDP uses the energy loss of particles to determine a depth profile, precise knowledge on the energy loss of low energy ions in matter is needed to understand the data. Energy loss of ions in matter due to interaction with electrons (also called electronic energy loss) is generally described by the Bethe-Bloch-formula [Blo33]:

$$-\frac{dE}{dx} = \frac{4\pi e^4 z^2}{m_0 v^2} N Z \cdot B \quad (2.5)$$

with v being the velocity of the ion, ze its charge, m_0 the electron mass and N the number density of electrons in the absorber material. B is given by

$$B = \left[\ln \left(\frac{2m_0 v^2}{I} \right) - \ln \left(1 - \frac{v^2}{c^2} \right) - \frac{v^2}{c^2} \right]$$

with I being the average excitation and ionization potential of the absorber [Kno00, p. 31]. While the formula nicely describes the overall dependencies of energy loss on the characteristics of the incoming particles (note the $\frac{1}{v^2}$ and z^2 dependencies), it still needs an input parameter I , which is almost always determined experimentally. Since I becomes dominant at low ion energies, the determination of energy loss of low energy ions becomes strongly dependent on experimental input parameters. Furthermore, for very low energy ions interactions with the potential of the target material's nuclei can also play a role. This process is often called nuclear stopping or non-ionizing energy loss, and is not included in the calculations using the Bethe-Bloch-formula.

Therefore, it is more feasible to rely on stopping power tables. These tables are determined experimentally by measuring the energy loss of ions as a function of ion energy, ion charge, ion mass, absorber type and absorber thickness. Extrapolation between these data points (often using sophisticated models for energy loss) then allows to compute energy loss for ions in matter very precisely. Examples of programs relying on this technique to determine energy loss are SRIM (Stopping Ranges of Ions in Matter) [Zie04], ATIMA (a webtool) [Mal19] and Geant4 [Ago03].

A typical NDP application would be the analysis of lithium contained within a carbon bulk material (as is common in lithium battery anodes). To illustrate the effect of the different energy losses of particles and the dependency between energy straggling (small differences in energy loss of identical particles passing through the same material, due to the statistical nature of the process) and depth resolutions achievable in NDP, a simulation using Geant4 was performed, which assumed a homogeneous lithium distribution in elementary carbon. A detector dead layer thickness of 80 nm of silicon was assumed. The detector resolution was simulated with a width in energy of $\sigma_E=8$ keV. The resulting distribution of energy loss and production depth is displayed in Fig. 2.3.

The simulation illustrates the different properties of ^3H - and α -particles in NDP. While ^3H -ions penetrate up to 30 μm of standard density, elementary carbon, α -particles are stopped after 5 μm . Due to the greater penetration depth of the ^3H -nuclei, the achievable depth resolution, especially near the surface, is a lot better for α -particles than for ^3H -particles.

To illustrate the influence of the assumed detector resolution compared to the effects due to energy straggling, a second simulation was performed, assuming a perfect energy resolution of the detector (but with the same dead-layer). Comparing these simulations helps to show the influence

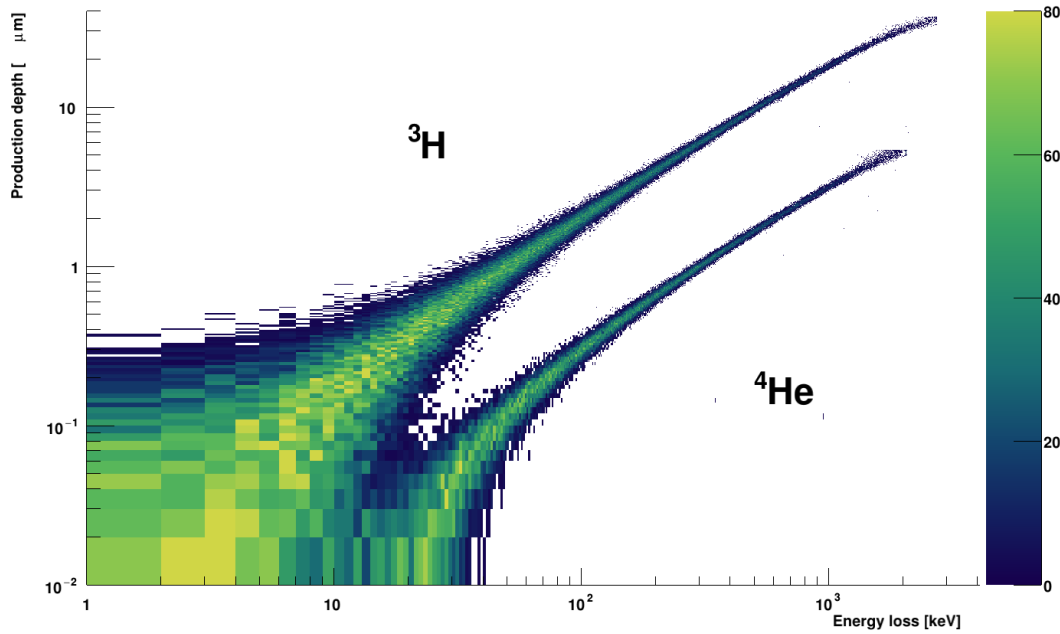


Figure 2.3.: Simulation of the ${}^6\text{Li}(n,\alpha){}^3\text{H}$ reaction in carbon ($\rho = 2.26 \frac{\text{g}}{\text{cm}^3}$). The simulation was performed using Geant4. A homogeneous distribution of lithium within elementary carbon was simulated. A detector dead-layer of 80 nm of silicon was included in the simulation. The two bands from the α - and ${}^3\text{H}$ -particles are clearly visible and have been marked in the graph. The greater penetration depth of the ${}^3\text{H}$ -particles and the better resolution achievable with α -particles is due to the higher specific energy loss of the α -particles.

of the electronics on the measurement quality in NDP. Comparing the results of both simulations by projecting the data on the energy loss axis and determining the width of those distributions provide information on the influence of detector resolutions and particle species on the depth resolution, which can be seen in Fig. 2.4.

While this simulation helps to illustrate the overall behaviour of particles in NDP, it is not perfect. One of the issues which is apparent is the atypical behaviour of the ${}^3\text{H}$ -particles, when assuming a perfect detector (see black dots in Fig. 2.4). This is due to the uncertainties of the energy loss model implemented in Geant4, and helps to illustrate the uncertainties in these types of calculations. Furthermore, the depth straggling plotted here is not identical to the achievable resolution. This resolution is influenced by the uncertainties of the distributions centroid, at least for arbitrarily thin lithium layers. Determining more complex distributions is not straightforward, and often depends heavily on assumptions regarding the samples composition, density and morphology.

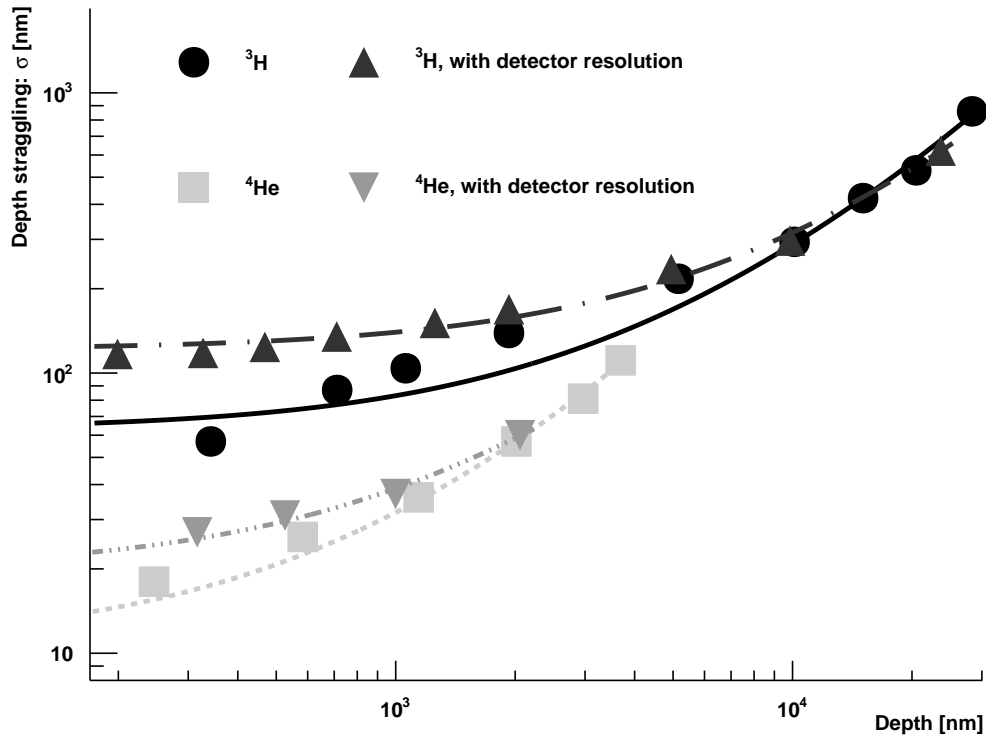


Figure 2.4.: Geant4 simulation of the ${}^6\text{Li}(n,\alpha){}^3\text{H}$ reaction in carbon ($\rho = 2.26 \frac{\text{g}}{\text{cm}^3}$). The simulation was performed once assuming perfect electronics, and once assuming a detector resolution of $\sigma_E = 8$ keV. In both simulations the dead-layer of the detector was set to 80 nm of silicon. The lines plotted represent quadratic fits on the simulated data. They are plotted only as visual guides. Adapted from [Wer18]

2.4. Experimental limitations

While determining integral isotope concentrations with a NDP-type experiment is rather straightforward, challenges arise when correlating measured energy spectra to depth distributions. Some originate from factors due to the experimental conditions (e.g. background radiation, instrument design), while others are due to the nature of the investigated sample (e.g. neutron scattering and absorption in the sample). In the following an overview of the most important experimental limitations will be given.

2.4.1. Effects of high count rates

Several spectra distorting effects can be observed in NDP-measurements. First, if event rates are high, pile-up can occur. Pile-up is when signals are being registered in the electronics, before the system had time to return to zero after the last event. Therefore the second signal will be piled on-top of the tail of the previous signal and be registered with more energy than it actually has. This effect can be seen in Fig. 2.5. In this measurement, a sample of massive boron-nitride was investigated. One can clearly see signals above the expected maximum at 1776 keV. Pile-up can

be reduced by several methods. One effective measure is to reduce the neutron flux illuminating the target. This can be seen in the gray curve in Fig. 2.5 where the neutron flux has been reduced to 6% of the full flux. Pile-up is reduced when compared with the full beam measurement.

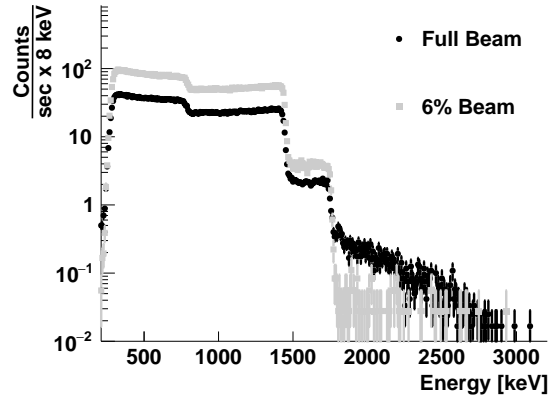


Figure 2.5.: Boron-nitride sample measured at the N4DP-instrument. A measurement at 100% neutron flux (black dots) and one at 6% neutron flux (gray squares) is shown. Data have been normalized for the amount of incident neutrons. No dead-time correction has been applied. A change in pile-up can be seen when comparing the curves at energies above 1776 keV. Furthermore, the detected rate (normalized for neutron flux density) varies strongly between the two measurements. This is due to dead-time effects in the electronics.

While pile-up can distort a measured signal shape, it is usually easy to spot, and can be reduced by introducing additional dead-time into the data acquisition. When the acquisition is triggered, there is a certain time-frame, in which no additional event can be taken. Due to this, observed count rates can severely underestimate the actual isotope concentrations in high rate measurements. A second artefact, which is more problematic in a NDP experiment is due to dead-time in the data acquisition. This manifests as an increase in the measured boron isotope concentration seen in Fig. 2.5. The preferable way to reduce this effect is by using measurements of a known sample with similar isotope concentrations as references (which will have comparable count rates and dead times), thereby applying a simultaneous dead-time and efficiency correction to the data. If those are not available, reducing the neutron flux at the sample position can be an effective way of diminishing this effect. Statistical models based on the known dead-time of the acquisition can also be used to correct for this artefact.

An alternative way to circumvent these issues, other than reducing the neutron flux on the target is to reduce the charged particle flux observed in the detector directly. This can be done by either increasing the distance between target and detector, or by using detectors with smaller active areas. An ideal case would be to use arrays of detectors with small active areas, thereby reducing the pile-up in each detector while retaining the full overall active area. An effective way to do this is by using segmented detectors.

2.4.2. Radiative background

Background can be induced by neutron capture reactions happening with materials other than the investigated sample (for example due to neutrons interacting with an entry window). The background count rate is very much dependent on the instrument at which the experiment is carried out. In general, three sources of background can be identified. One is hard to shield γ -radiation. A second source is β -radiation caused, for example, by aluminum activated by the neutron beam. This background sources can be reduced by decreasing neutron scattering (for example thin entry windows), increasing shielding, and by using detectors which are as thin as possible. The third source are charged particles produced by neutron capture reactions on materials other than the investigated sample. This is often due to low level boron contaminations in the experiment (since boron is a commonly used neutron absorber). A detailed analysis on measures to improve the signal-to-background ratios at the N4DP instrument can be found in Chapter 4.

2.4.3. Sample dependent effects

The energy loss of the charged particles detected in NDP depends on sample density and material composition as well as on the propagation distance of the charged particles in matter. Therefore, interpreting energy spectra obtained with NDP is not unambiguous, and additional information on a sample is needed to get a high precision relation between measured energy loss and depth distributions of the NDP-active isotopes.

Depending on the chemical composition of the sample, and most important, depending on its density, the specific energy loss may change with changes of these quantities [Blo33]. Therefore, a change in density can not be distinguished from a change in gradient within a NDP measurement. This is due to the fact, that increased energy loss will stretch a spectrum along the energy axis, while the integral number of counts will stay constant, thereby compressing the spectrum shape along the intensity axis. This produces the same measurement results as if the concentration of NDP-active isotopes would lower with greater depth.

One further concern when interpreting energy-spectra obtained with NDP is, that the morphology of complex samples may influence the energy spectra obtained. Examples of this can be found in [Tru18]. In Fig. 5.5 for example, one can see a sharp peak at the high energy onset of the spectrum (≈ 2700 keV) for the first few charge cycles (adapted from [Tru18]). Commonly this would be assumed to indicate an increased lithium concentration right at the surface of the sample. This is not necessarily the case, with the peak, in this case, being due to the special morphology of the investigated sample [Tru18].

2.5. Application examples

The isotope specific nature of NDP (see e.g. Table 2.2) constraints the application of the method. A further limitation is the limited range of the charged particles in matter. For example, a triton particle with 2727 keV, as produced in the ${}^6\text{Li}(n,\alpha){}^3\text{H}$ reaction will only have a range of 41 μm in Silicon (value calculated with ATIMA). These physical characteristics of the method constrain it to certain applications, namely the investigation of thin film structures which have NDP-active

isotopes as part of their composition.

Historically, the first application was the investigation of boron-doped semiconductor materials [Zie72]. Due to the high neutron capture cross sections, ^3He , ^6Li , ^{10}B are best suited for NDP measurements. Due to the low isotopic abundance (compare Table 2.2) ^3He is seldom used. Furthermore, being a noble gas, helium is not useful for most material science applications. This leaves lithium and boron as the most promising candidates for NDP-based material analysis applications.

Boron is an interesting element for NDP-based investigations, not only due to its usage in doping semiconductors, but also due to its applications in many other materials. Applications range from boron containing glasses [Wer18], use in super-alloys [Muk12] to boron based ceramics, like boron-nitride or boron-carbide. Lithium, on the other hand, is mostly interesting due to its use in rechargeable batteries [Liu14, He15a, Liu16, Han19, Tru18, Wet18b]. Nevertheless, other select lithium containing systems might be of interest. Lithium-niobate, which can be used in light guides, has been investigated with NDP on several occasions [Tru18, Kol98].

Several NDP measurements performed with the N_4DP instrument can be found in Chapter 5.

3. The N4DP Instrument

When designing a NDP instrument, several parameters have to be considered for an optimal performance. A high neutron flux density is needed to minimize measurement times and improve detection limits. A vacuum chamber has to be designed. Choice of materials used, and the physical design both matter with respect to reducing background count rates (thereby improving detection limits) at the instrument. An instrument control needs to be implemented into the experiment, which allows for an easy use of instrument and sample changer by external users. Detectors and readout electronics play a central part, as these will limit the achievable (depth) resolution at the instrument and significantly influence the background. This chapter describes all the components of the N4DP instrument, which have been developed in the scope of this work, while Chapter 4 will present the achieved performance.

3.1. The experimental Site

The N4DP instrument uses the powerful cold white neutron beam available at the PGAA facility at the Forschungsneutronenquelle München (FRM II). The average energy of the neutron beam is 1.83 meV (6.7 Å). At the end of the curved, elliptical neutron guide NL4b which leads from the cold source to the PGAA facility, two neutron guide configurations are available as guide options. One is a rectangular collimation system providing a maximum neutron flux density of $5 \times 10^9 \frac{n}{\text{cm}^2 \text{s}}$ with a beam spot size of $2 \times 1 \text{ cm}^2$ and a homogeneous beam profile. The other is an elliptical tapered nose with a maximum flux density of $3 \times 10^{10} \frac{n}{\text{cm}^2 \text{s}}$ and a smaller spot size [Rev15]. All flux densities are given as thermal equivalent and have been determined by gold foil activation. For the N4DP instrument the beam spot is collimated down to a circular shape of $\approx 4 \text{ mm}$ in diameter. This is achieved through a combination of boron containing rubber to collimate the neutron beam, and a lead frame to shield against the γ radiation.

The neutron guides of the facility are shielded with a combination of boron containing rubber and lead bricks with reduced antimony content. This allows for effective shielding of neutrons and γ -radiation originating from the neutron guide. The beam stop is designed of boron containing rubber surrounded by lead, to stop any neutrons which have not interacted in the experiment. The experimental site itself has to be surrounded with additional shielding to prevent heightened background in the PGAA's germanium detectors, as well as for health physics reasons. A drawing of the layout is presented in Fig. 3.1.

Since radiation produced inside an experimental chamber will dominantly consist of β - and γ -radiation (see Chapter 4), this shielding consists of lead-bricks. The whole experimental side is encased in concrete walls, as to further reduce the radiation hazard. The shielding at the PGAA facility is the spatially limiting factor for the design of the N4DP chamber. An overview sketch of the N4DP setup is shown in Fig. 3.2. The chamber is described in detail in Section 3.2.

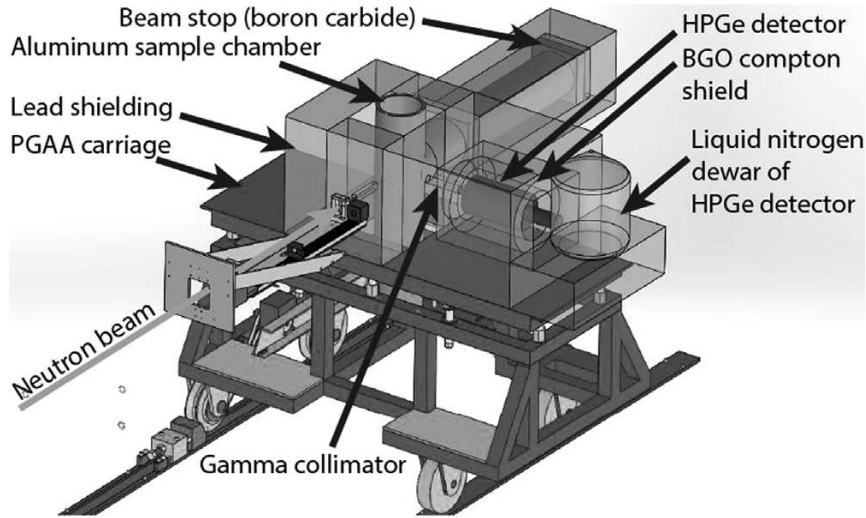


Figure 3.1.: Sketch of the PGAA facility with shielding, beam stop and the PGAA detector. For the N4DP setup the PGAA chamber is replaced with the N4DP chamber as shown in Fig. 3.2. Adapted from [Rev15].

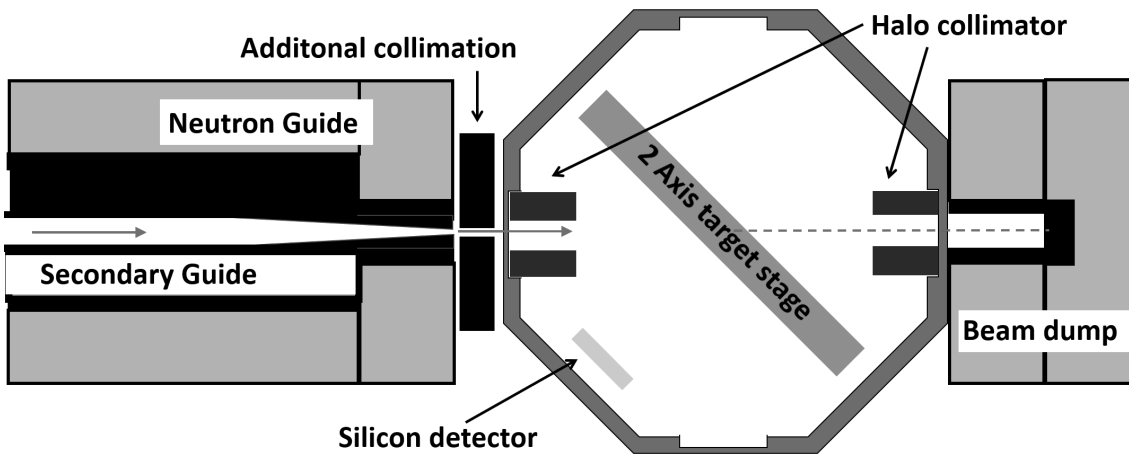


Figure 3.2.: Top view sketch of the N4DP setup, showing neutron guides of the PGAA facility, chamber, sample stage and a detector. Important parts are labeled and described in detail in the text. Taken from [Wer18].

3.2. Chamber Design

The major design aim of the N4DP instrument is a low background count rate. The options for the design are limited by the constraints at the experimental site itself. Shielding, existing detector systems and neutron guide design all limit the available space. Minimizing the background count rate in the chamber demands a design as large as possible. This is accomplished using an octagonal base shape, which also allows for multiple (electrical) connections into the chamber. A modular design approach enables great flexibility in all components of the instrument.

The N4DP instrument is usually operated at a pressure of $2 \cdot 10^{-5}$ mbar. This not only minimizes

energy loss due to the investigated charged particles interacting with rest gases (which is already heavily suppressed at pressures around 10^{-2} mbar), but also drastically reduces background from the $^{14}\text{N}(n,p)^{14}\text{C}$ reaction. Optionally, the N4DP instrument can also be flooded with a helium atmosphere, which is useful when performing *operando* measures on samples which need higher pressures to function. In this case, pressure of the helium atmosphere can be chosen to be any value below 500 mbar (for lithium containing samples). Details on *operando* measurements can be found in Section 5.3.

Since opening and closing of a vacuum chamber takes time, and since any change in the setup, like opening the chamber, can introduce measurement uncertainties, a vacuum chamber suitable for NDP should be able to contain many samples at once, with a possibility to exchange samples. At the N4DP instrument, this is done using two stepping motors to access every point of the target plane. The sample changer is described in detail in Section 3.3.

The width of the N4DP chamber is constrained by the shielding at the PGAA facility. To make optimal use of the space, while still allowing for access to the chamber from as many directions as possible, an octagonal shape was chosen as the chamber's centerpiece. The chamber has an inner diameter of 388 mm, and is milled out of a block of AlMg3-alloy. Fig. 3.3 shows a technical drawing of the chamber's center piece.

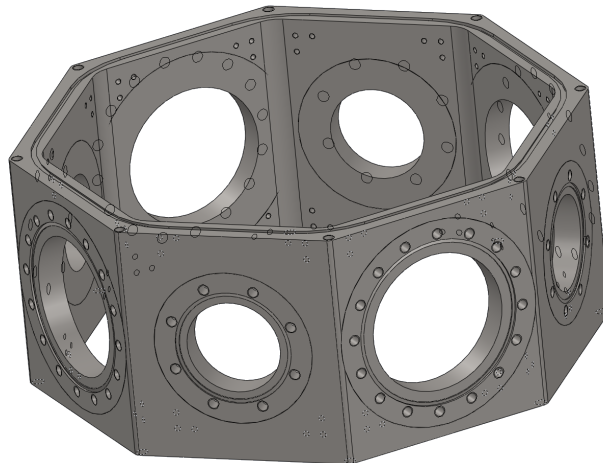


Figure 3.3.: Technical drawing of the octagonal centerpiece of the N4DP chamber.

This center-piece has a total of 8 CF-flanges, alternating between the CF-63 and CF-100 standards. Beam entry and exit windows consist of $100\ \mu\text{m}$ thick aluminium sheets. These are glued onto CF-63 flanges, which have a hole with a diameter of 38.5 mm processed into them. Due to the small diameter of the used neutron beam (ca. 4 mm), this configuration provides an optimum between mechanical stability and reduced scattering. Optional halo collimators, placed behind the entry window, and in front of the exit window are made from boron containing glass tubes and can be used to minimize background from scattering of the neutron beam on entry and exit windows even more.

The CF-63 flanges perpendicular to the neutron beam direction are used as interface flanges towards the existing PGAA-detectors, therefore allowing to perform simultaneous PGAA and NDP measurements. In the current configuration of the N4DP-instrument, these flanges are

identical to the beam exit and entry windows. The four remaining CF-100 flanges are used for electrical connections into the chamber. These include sample changer control, connections for charging and discharging batteries as well as signal and power connections for additional sample environments.

To make the chamber easier to handle, it is separated into several segments. The octagonal centerpiece has a circular stainless steel segment below and above it. The lower stainless steel segment has a height of 86.5 mm. Together with the 30 mm thick bottom plate of the chamber this lifts the center of the beam entry flanges to the height of the neutron beam. The segment on top of the octagonal centerpiece has a total height of 187 mm. This optimizes the area of the accessible sample plane.

The bottom plate of the chamber is constructed from AlMg3. It provides numerous mounting options for the sample stage (it can be mounted at 45° , 67.5° and 90° degree angle relative to the neutron beam direction). Furthermore, detectors can be mounted at several different positions. Mounting options for apertures complete the bottom lid. The top lid of the chamber has two KF-40 flanges, which are used to connect the (vacuum) pumping system. Two rectangular flanges allow for mounting preamplifiers connected to the surface barrier detectors (for more detail see Section 3.5). A large central opening allows to exchange samples without having to disconnect electronics or vacuum pumps. This flange is covered by a lid with a glass viewing window which allows for an optical check of the samples and sample positions. During measurements this window is covered to prevent light reaching the detectors. A cross section of the full chamber is displayed in Fig. 3.4.

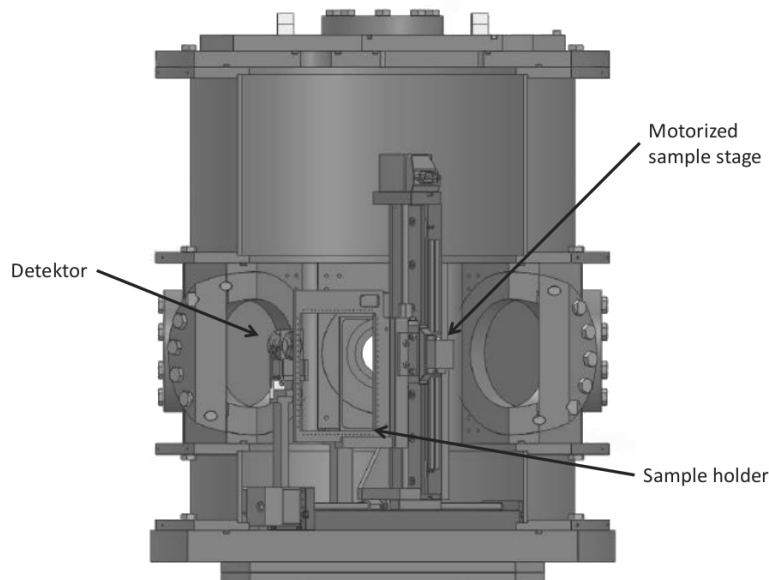


Figure 3.4.: Cross section of the N4DP experimental chamber. Flanges, sample stage and a detector can be seen. Several important parts are labeled. The viewing direction is opposite to the neutrons beam direction (the neutrons would come out of the picture).

3.3. Sample/Target Stage

The sample/target stage is based on two stepping motors. These allow to adjust the sample position in horizontal and vertical direction. This enables to illuminate a total area of $250 \times 250 \text{ mm}^2$ with the neutron beam. High precision stepping motors of the type VT50L¹ are used. These not only allow for excellent reproducibility of the target position (theoretically $\approx 1 \mu\text{m}$, if thermally stabilized and properly protected from vibrations), but are also capable to be used in vacuum, and function without the need for lubricants. This is very important in NDP, since even thinnest oil films on samples, which could be produced by vaporization of motor lubricants in vacuum, can influence measurement results.

The N4DP sample stage is designed to be highly modular. It consists of the motor stage itself, and quick exchange sample holders. The motor stage possesses two high precision fitting rails (one horizontally and one oriented vertically). Sample holders can be pushed into these fittings. A metal spring ensures that the sample holders position is fixed without the need for screws or alignment pins. Therefore the exchange between different sample holders can be performed quickly and easily by a single experimenter.

The modular approach used at the N4DP instrument allows for specialized sample stage designs for specific applications. Some of those are briefly discussed here (a more detailed account can be found in the thesis of M. Trunk). The most basic is an aluminium frame with four threads processed into it. This allows for the use of any custom sample holder designed by a user in the experiment. For thin film samples which need mechanical support, a grid like sample holder has been designed. It is milled out of 2 mm thick aluminium sheets. Samples are fixed on the grid using elastic strings. The neutron beam passes through the openings in the grid, thereby minimizing neutron scattering.

For mechanically stable samples, a aluminium frame with elastic wires is used. These wires form a grid like pattern, and allow to fix samples by alternating positions of the wires in front and behind the sample. The drastic reduction in material close to the neutron beam compared to other sample holders, makes this the preferred option for stable, passive samples.

The most complex sample holder currently in use at the N4DP instrument is used for *operando* measurements of lithium ion batteries. It uses a single grid like row to mount calibration samples. Below that, there are mounting options for four coin cells. Through a combination of Polyether ether ketone (PEEK) isolators, conducting copper frames and spring contacts, each coin cell is supplied with an individual ground and voltage connection. Connection to a charging device outside the chamber is provided via one of the CF-100 flanges.

3.4. Instrument Control

One of the challenges in any new instrument is the implementation of an instrument control. This instrument control is used for controlling detectors, readout electronics and other instrument parameters. Requirements are, that almost all control functions should be accessible remotely,

¹ produced by MICRONIX USA, LLC, Irvine, CA

since access to the instrument is impossible during operation. Furthermore, the control should be reliable, as to limit downtime of the instrument, and should be easy to use, achieving good accessibility for new users.

To simplify user control, the N4DP instrument uses a single, central, control computer. This computer is used as the host of the N4DP instrument network. Via a FL Switch 7000¹ and the Dynamic Host Configuration Protocol (DHCP) it can communicate with all parts of instrument control. While some of the hardware (the TRB backend for example, see Chapter 7) is connected directly to the network, other parts are connected via an intermittent computer (the MARaBOU data acquisition for example, see Section 3.5). Computers connected to the network are accessed via secure shell (ssh), which provides standardized, direct and easy access to them. Other hardware is controlled via software packages directly executed on the central computer. An overview of the network structure is given in Fig. 3.5.

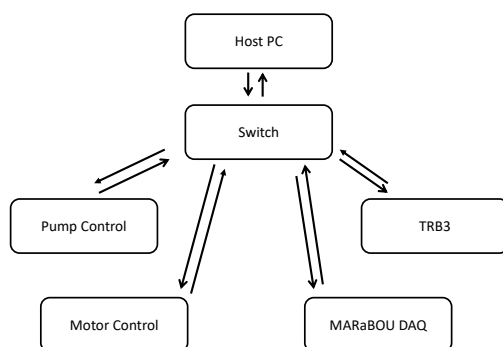


Figure 3.5.: The N4DP instruments network architecture. A switch with 4 100 Mbit/s ports for slow control and 4 1Gbit/s ports for data acquisition purposes is used.

An important aspect of the instrument control is the handling of sample changes. The stepping motors of the sample stage are controlled with the MMC-200 controller and driver, produced by MICRONIX. The motors are used in a closed loop configuration. The driver allows for simple communication with a PC using a RS-232 interface. The motors can be directly controlled via a dial-in terminal (for example using the cu command in Linux based host systems) and a specialized language for motor instructions. Expect scripts (an extension of the Tool command language (Tcl)) have been designed to package this communication and commands in an easy to use way. They can be controlled via Tcl based graphical user interfaces (GUIs), which provide a simple way to control the motors. The GUIs are designed to mimic the physical layout of the corresponding sample holders, with one GUI for each sample holder design. This provides an intuitive interface for any user at the instrument. Fig. 3.6 presents an example of a GUI layout.

¹ Produced by PHOENIX CONTACT

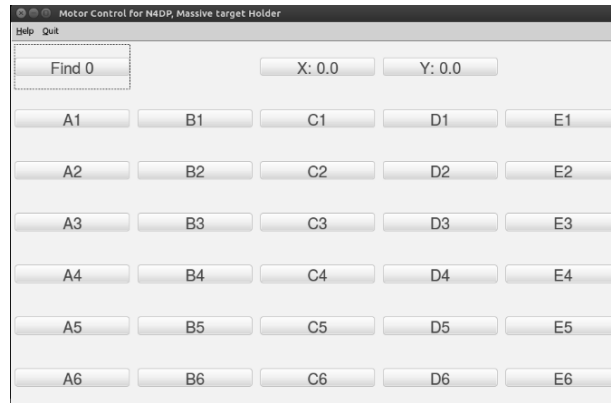


Figure 3.6.: Screenshot of a GUI used for motor control. Depicted is the state right after setting the zero positions at the end switches. The GUI mirrors the physical structure of the sample holder. The interface is kept as simple as possible, to reduce potential usage errors.

3.5. Detectors and Electronics

The main requirements for unsegmented NDP detectors are a good energy resolution, a homogeneous, thin dead-layer, and high radiation tolerance. For these reasons silicon-surface-barrier detectors¹ are used at the N4DP instrument. The detectors are 100 μm thick, with an active area of 150 mm^2 and a dead-layer equivalent to 80 nm of silicon [Wer18].

The detector signals are pre-amplified using charge sensitive preamplifiers², which are mounted on a custom made motherboard. The board handles power supply and filtering. Furthermore, a second amplification stage based on the LM6172IMX/NOPB operational amplifier³ further amplifies the signal and provides a differential output. This allows to minimize the noise introduced by the signal transfer from the preamplifier stage to the shaping amplifier. A MSCF-16-F-V⁴ low noise shaping amplifier is used. Besides shaped and amplified signals, it also provides trigger signals using constant fraction discriminators. This analogue electronics chain is the default setup at the N4DP instrument and is called Setup I. If not stated otherwise, all data have been taken with this configuration.

A lower resolution electronics configuration consisted of a charge sensitive MMPR1⁴ preamplifier combined with a STM 16+⁴ 4 pole shaping amplifier [Wer18], which also provides trigger signals. This setup was used, together with a 300 μm thick surface barrier detector⁵, for the first measurements at the N4DP instrument and is called Setup II in the text. All data taken with Setup II have been normalized in intensity using $R = \frac{150 \text{ mm}^2}{450 \text{ mm}^2}$, the ratio between the active areas of the two detectors. This allows to directly compare count rates for both setups.

For both setups the triggers and signals were fed to a 32 channel CAEN V785 peak-sensing

1 Produced by Ortec, model number: AD-025-150-100

2 Model A1422H, produced by CAEN

3 Produced by TEXAS Instruments

4 mesytec GmbH & Co. KG, 86540 Putzbrunn, Germany

5 From the company ORTEC. The active area is 450 mm^2 , the dead-layer is equivalent to 80 nm of silicon. Model Nr.: BE-19-450-300

Analog-to-Digital Converter (ADC). This ADC digitizes the data with 12 bit resolution. The data acquisition and online monitoring is then performed using the MARaBOU [Lut17] software package, which is based on MBS [NK18] for data acquisition and the ROOT [Bru97] software package for online monitoring of the data.

4. N4DP: Performance with surface barrier detectors

In this chapter the performance of the N4DP instrument is presented. The sources of background and the methods to minimize it (thereby improving detection limits) are discussed in Section 4.1. Section 4.2 deals with the calibration of the instrument. The so-called Pulse-Height-Defect (PHD) is of special interest here, since it influences measurements depending on the ion species detected. Both the applied energy loss model and the calibration function are verified using a sophisticated custom-made sample. The excellent depth resolution achievable with the system (below 10 nm) is presented in Section 4.3. Alongside the resolution, typical pitfalls when interpreting NDP spectra are also discussed. The chapter concludes with an investigation into systematic uncertainties at the N4DP instrument, which are shown to be small, and stable in time.

4.1. Background

Three different paths were pursued at the N4DP instrument to reduce background. These consist of additional shielding outside of the chamber, optimizing neutron scattering on beam windows and sample holders, and optimizing the detector thickness. In the following, the general situation at the experimental site will be briefly sketched. Afterwards, the different ways to reduce the background are discussed one by one, and the effectiveness of the measures undertaken to reduce background is presented.

The last meter of the neutron guide before the N4DP experimental chamber is not evacuated. At the end of this guide, the large sized neutron beam (spot sizes in the centimetre range) is collimated down to a circular beam with a diameter of 4 mm, using a boron aperture. Lead is placed behind the boron to reduce background from neutrons stopped in the collimator. All these provide potential sources for neutron scattering. Since the neutron guide at the PGAA is made of sodium containing glass¹, it activates significantly and produces γ -radiation. Background from these sources has been reduced by introducing additional lead shielding [Wer18].

The first option to reduce background, by applying (external) shielding, aims at reducing the amount of γ -radiation at the detector position. As shown in [Wer18] (compare Fig. 4.1), the main background component below 350 keV is dominated by γ -radiation originating upstream of the experiment and can therefore be shielded. The effect of the increase in shielding can be seen in Fig. 4.1. For the data set taken with increased shielding, an additional 5 cm of lead were introduced between the shielding of the neutron guide and the N4DP chamber.

The amount of shielding that can be introduced is limited by the geometries at the experimental site. The reduction in background count rate is below 30%, even in the energy range where the shielding was most effective. Furthermore, there is no discernible effect on the background for

¹ Zs. Revay, private communication

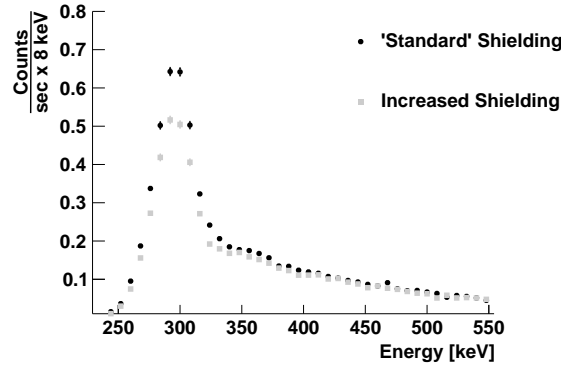


Figure 4.1.: Background at the N4DP instrument. Data have been taken using Setup II, see Section 3.5. Black circles show the background when using the 'Standard' shielding (the shielding of the PGAA beamline), while gray squares show the background after additional lead shielding was introduced between the neutron guide and the N4DP chamber. A $2 \mu\text{m}$ thick mylar foil was used as a sample in both data sets. The data show that the low-energy background is dominated by γ -radiation originating outside of the N4DP chamber, while the higher energy background (dominant above ca. 350 keV) is not influenced by the shielding at all.

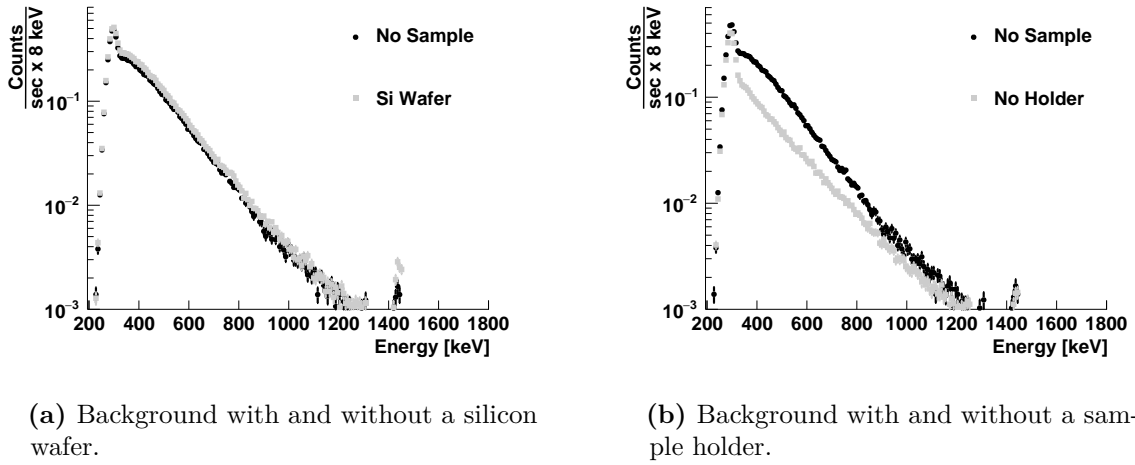
energies above ≈ 350 keV. Therefore adding more shielding is not an effective way of improving the N4DP instrument. Since most of the radiation is introduced by activation of the sodium containing neutron guides, exchanging those guides using materials optimized for low background applications might provide a more effective option for further background reductions. All in all, improving the external shielding of the chamber is not effective in improving the signal-to-background ratio (SBR).

The second approach to reducing background was to reduce neutron scattering and absorption. This was done via reduction of entry window thicknesses, by optimizing the collimator systems, and by reducing scattering on the sample holders as much as possible.

Entry and exit windows provide sources for neutron scattering and absorption. They have been designed from $100 \mu\text{m}$ thick aluminum sheets, to minimize scattering while still allowing for optimal stability. Additionally to scattering on the entry and exit windows, also scattering on sample holders and samples influences the background situation.

Fig. 4.2 shows contributions to the background from different sources. One can see, that even the idealized sample of a thin silicon wafer introduces additional background in the chamber. Furthermore, there is a significant background component introduced by the sample holder. As this particular sample holder was designed for mounting thin films and foils which need mechanical support, a reduction of the material next to the beam, and thereby decreasing the induced background was not possible for this configuration. As is seen in Fig. 4.2, the influence of even an idealized sample is greater than the background induced by scattering on the sample holder, which in turn produces more background than the entry and exit windows. Therefore, no further optimization in this regard is needed.

As can be seen in Fig. 4.2 the main contribution to high energy background, which is the dominating factor in the SBR, is an exponential function. This is due to activation of the aluminium walls of the chamber by scattered neutrons, which produces β -radiation. These electrons



(a) Background with and without a silicon wafer.

(b) Background with and without a sample holder.

Figure 4.2.: Background measurements at the N4DP instrument. Data has been taken with Setup II, see Section 3.5. One can see, that a $500\ \mu\text{m}$ thick silicon wafer (gray squares, (a)) introduces almost no additional background when compared to the measurement with a sample holder (black dots). The sample holder itself contributes significantly to the background situation in the chamber. In (b) a measurement with a sample holder (black dots) is compared with one without a sample holder (gray squares). The changing of the spectral shape indicates, that the sample holder has introduced an additional component into the background. Since the contribution of the sample holder decays faster than the base exponential function, the influence at higher energies is negligible. The peak at ca 1450 keV is due to a boron contamination within the chamber.

are produced with an energy of roughly 2.8 MeV [Pri11], which means that they pass through a considerable amount of matter.

The third approach for reducing background is to use thinner particle detectors. The nuclei investigated in NDP are stopped within a few tens of micrometers, which means, that comparatively thin detectors can be used. The result of this approach can be seen in Fig. 4.3. There the measurement of a reference sample from NIST¹ the SRM 2137 can be seen. It has been performed using two detectors of different thickness, one is $100\ \mu\text{m}$ thick (Setup I) and one with a thickness of $300\ \mu\text{m}$ (Setup II), both from the company Ortec. Reducing the thickness of the detector significantly decreases the background, and thereby improves the SBR by an order of magnitude.

The detector thickness was reduced by a factor of 3, thereby improving the SBR by an order of magnitude. This indicates, that the SBR is connected to the inverse square of the detector thickness. This can be understood if one considers the types of radiation that constitute the background. β - and γ -radiation, which are the main sources of background, will pass through the detectors. These particles mainly interact with matter by producing mostly secondary electrons or photons with comparatively high energy [Kno00]. The likelihood of producing these secondary particles is connected to the detector thickness. When the produced secondary particles pass through matter they lose energy in proportional to the thickness of the detector. Therefore, the overall likelihood for a certain energy signal being produced by one of these primary particles is dependent to the square of the detector thickness. By reducing the detector thickness and

¹ National Institute of Standards and Technology, Gaithersburg, Maryland, USA

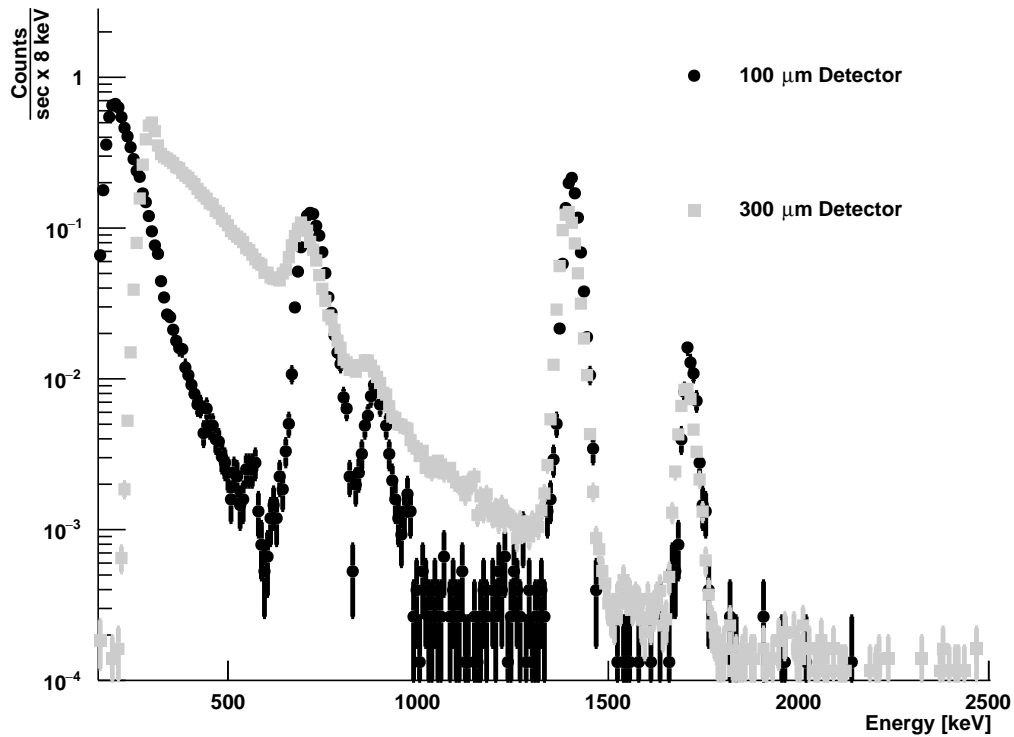


Figure 4.3.: Measurements of the SRM2137 sample at the N4DP instrument. Black dots describe a measurement performed with a 100 μm thick detector (Setup I), while the gray squares stem from data taken with a 300 μm thick detector (Setup II). Both detectors have the same dead-layer thickness. The improved signal-to-background ratio can be seen clearly. The sample is described in detail in Section 4.2.

therefore the background count rate, it was possible to lower the trigger threshold of the system to about 200 keV. Therefore reducing the detector thickness allows for the measurement of lower energy particles, enabling NDP over a wider range of sample depths.

Using thinner detectors is the most effective way to reduce background. The particles with the highest penetration depth investigated in NDP are the 2727 keV ^3H -nuclei from the $^6\text{Li}(n,\alpha)^3\text{H}$ reaction. These can penetrate up to 42 μm in silicon of standard density ($2.33 \frac{\text{mg}}{\text{cm}^3}$, calculated with ATIMA [Mal19]). Therefore any detector thickness greater than $\approx 50 \mu\text{m}$ of silicon will not improve the signals. Since the background is strongly dependent on the detector thickness (see Fig. 4.3), optimizing detector thicknesses is the most promising path for further improvements of the SBR. This is planned for the custom made detectors which will be used in the N4DP instrument upgrade (detailed in Chapter 8).

4.2. Calibration

The energy calibration plays a central role in NDP, since even small disturbances and uncertainties in the calibration influence the calculations of depth distributions significantly. For the calibration to be useful, it has to be valid for an energy range from a few hundred keV (≈ 200 at the N4DP instrument) up to 2727 keV (the highest energy NDP nucleus). Furthermore the calibration should be valid for a range of ion masses and charges.

The calibration procedures used at the N4DP instrument are based on the use of standardized, well known NDP samples. These samples include thin films deposited on top of a bulk material, but also depth distributions of active material within a passive bulk, as well as multi-layered samples designed especially for the purpose of a quick and comprehensive calibration. A major challenge in calibrating a silicon based detector in this way is the influence of the detectors dead-layer on the measured energy. To correct for this effect, energy loss calculations for dead-layers have been performed using ATIMA [Mal19]. These calculations are especially important in the case of samples with complex depth distributions and when using multi-layered samples.

The NIST standard reference sample SRM2137 was produced by implanting boron into a silicon wafer. Implantation profiles and boron concentrations can be found in the NIST certificate of analysis¹. The neutrons illuminating the sample react with the boron in the $^{10}\text{B}(n,\alpha)^7\text{Li}$ reaction. As noted in Table 2.2, with a probability of 96%, the ^7Li will be in an excited state after the reaction. This state is located 478 keV above the ground state of the lithium. The peaks corresponding to these reaction branches are denoted with $^7\text{Li}_e^*$ (840 keV lithium nucleus) and $^4\text{He}_e$ (1472 keV α -particle). When the lithium is produced in its ground state, the energies will be 1013 keV ($^7\text{Li}_g$) and 1776 keV ($^4\text{He}_g$). Fig. 4.4 shows a measurement of this sample, performed at the N4DP instrument.

Besides the SRM2137, calibration samples include a lithium-fluoride (LiF) thin film (about $4 \frac{\mu\text{g}}{\text{cm}^2}$ thick) deposited on a $2 \mu\text{m}$ thick mylar foil and a 10 nm thick boron-carbide (B_4C) layer on a silicon wafer. Using the two thin film samples a calibration routine was designed. In this routine, a Relative Pulse Height (RPH) was determined. It is defined as:

$$\text{RPH} = \frac{E_{\text{calc}}}{\text{ADC} - \text{offset}} \quad (4.1)$$

with E_{calc} the expected particle energy as calculated with ATIMA, ADC the measured ADC channel value, and offset as the offset of the electronics in ADC channels. This offset is then varied and compared with a linear fit on the RPH. χ^2 minimization then yields the optimal offset value. This technique should yield a constant RPH. The result is shown in Fig. 4.5. A linear dependency between the RPH and energy is visible (independently of the chosen offset), which is equivalent to a nonlinearity in the gain. The integral nonlinearity of all used electronics components is far below the nonlinearity measured here, and the result has been reproduced using different electronics and detectors [Wer18]. Therefore detector thickness and aging due to radiation exposure can be excluded as sources of the effect [Wer18]. Since two of the samples are of thin films on the surface of bulk material, and since they show the same behaviour as the SRM2137, this effect can also not be due to the applied energy loss models.

¹ <https://www-s.nist.gov/srmors/certificates/2137.pdf>

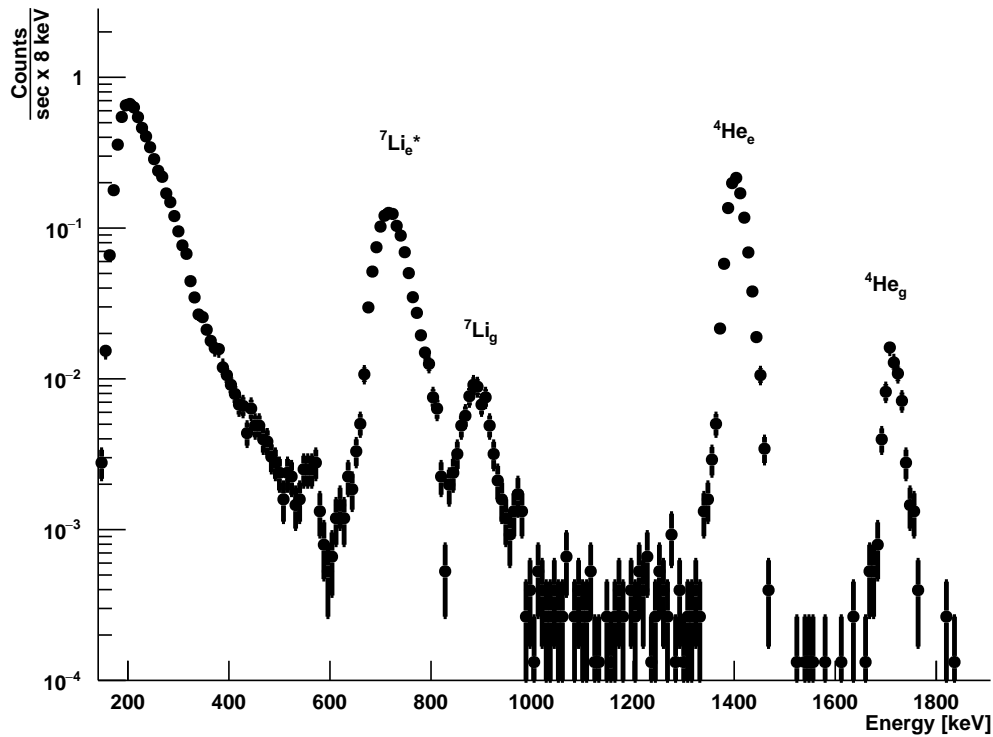


Figure 4.4.: Measurements of the calibration sample SRM2137 at the N4DP instrument. Data have been taken with the setup described in Section 3.5 (Setup I). The four peaks from the $^{10}\text{B}(n,\alpha)^7\text{Li}$ reaction are clearly visible. The broadening of the peaks, and the shift to lower energies is due to the known implantation profile of the boron in the bulk of the silicon wafer.

The so-called Pulse-Height-Defect (PHD) seems to be the most likely reason for the observed nonlinearity [Fin73, Len86, Len87]. This effect describes a dependency between the weight, charge, and energy of ions and the observed pulse height, meaning, that for example two ions with the same energy but different charges will produce different pulse-heights in a silicon detector. This effect is strongest in fission fragments, but is also observed for light ions.

A multi-layered sample (multistack) was designed¹ to verify the PHD, and to further improve the energy calibration. This sputtered sample consists of alternating 3 nm thick $^{10}\text{B}_4\text{C}$ layers and silicon layers. The layer structure begins (surface) with a nominal 100 nm thick Si layer, which is followed by a B_4C layer. This structure is repeated 5 times. Then nominal 200 nm thick Si layers alternate with B_4C layers again for 5 times. Below that, nominal 500 nm thick Si layers alternate with B_4C layers. For the 500 nm thick Si layers, only α -particles could be measured. Since this makes it impossible to verify the Si-layer thicknesses by comparing two independent particles, these layers have not been included in the analysis.

¹ Produced by MOVATEC GmbH, Eching, Germany

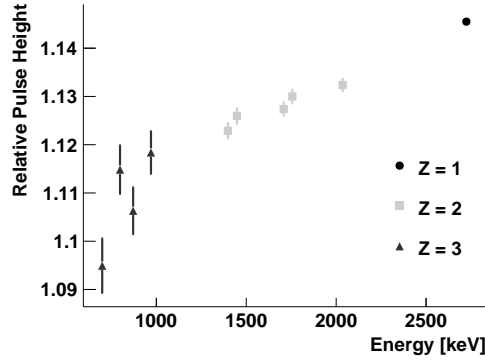


Figure 4.5.: Calibration measurement performed with the N4DP instrument. Data are extracted from measurements with several different calibration samples. The Relative Pulse Height (RPH) as defined in Eq. (4.1) is shown as a function of the calculated particle energy. Uncertainties are dominated by the uncertainty from the ATIMA calculations which was assumed to be 0.5 keV per nucleon. The three ion species are denoted by their charge Z .

Using the calibration determined with the data shown in Fig. 4.5, a systematic offset of the RPH from unity was measured. While the RPH was expected to have a value of 1, values of ≈ 0.81 were observed for α -particles. This is ascribed to a difference in density between the nominal silicon density, which is given for crystalline silicon, and the density of sputtered silicon, which constitutes the silicon in the sample. These differences in density are expected for sputtered samples. Therefore the density was corrected with a correction factor of 0.8089 ± 0.0015 .

The results of the density correction can be seen in Fig. 4.6. The nonlinear calibration used describes the data well. Up to this point, only the α -particles have been considered in the analysis of the sample. The good agreement between the RPHs of lithium- and α -particles verifies the results. The observed small differences from expectation can be ascribed to the PHD, which is not sufficiently corrected for by the used calibration curve. A unified calibration for all particle species is of advantage in NDP measurements, since one will almost always encounter several particle species at once. Since the deviation is below 2% for almost all data points, the applied calibration model is sufficient for almost all practical NDP applications.

Besides showing the influence of the PHD on NDP measurements and calibrations, the data from the multistack agree well with the energy loss calculations from ATIMA. The overall viability of the N4DP calibration routine was shown, and the mean deviation was determined to be 1.3%.

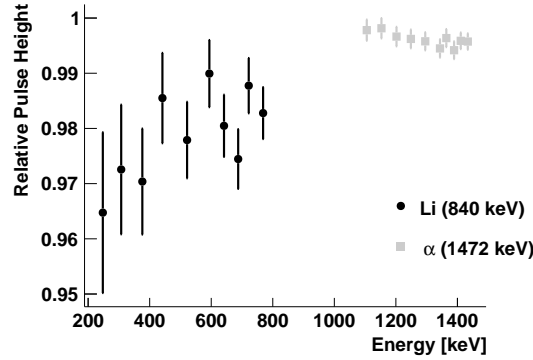


Figure 4.6.: Multistack measured with the N4DP instrument. Displayed is the Relative Pulse Height after calibration. While it is constant for α -particles, there is an energy-dependent deviation for lithium ions. This is due to the PHD, which is not fully corrected by the applied calibration function. The uncertainties are dominated by the uncertainties of the energy loss calculation with ATIMA, which was assumed to be 0.5 keV per nucleon.

4.3. Energy and Depth Resolution

The energy resolution of a NDP system is closely related to the best depth resolution achievable for the system. Since the depth resolution in NDP also depends on the material under investigation and the depth profile itself (see Chapter 2), there is no single depth resolution value that can be given. Therefore this section will deal with the Equivalent Noise Charge (ENC) and the energy resolution achieved for nuclei produced in thin surface films.

The ENC is defined as: *"the amount of charge, that applied suddenly to the input terminals of the system, would give rise to an output voltage equal to the RMS level of the output due only to noise"* [Kno00, p. 630]. It can be measured easily if the electronics chain in question simply receives random triggers, which are uncorrelated to any input signal. Such randomized trigger signals are continuously provided at the N4DP instrument, as to allow a constant monitoring of the detector and electronics performance. One such measurement can be seen in Fig. 4.7. Using a Gaussian fit, the ENC was determined to be 6.47 ± 0.12 keV (1787 ± 33 electrons).

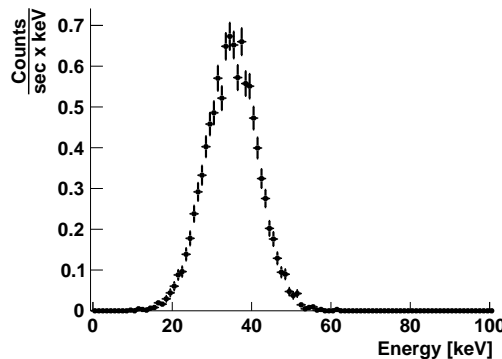
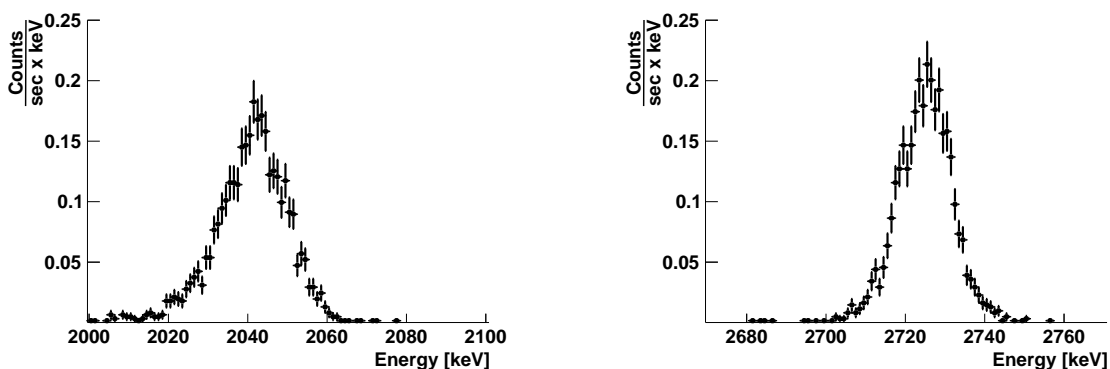


Figure 4.7.: Electronics noise of the N4DP instrument. ENC can be determined from the distributions Root-Mean-Square (RMS). It has been determined to be 6.47 ± 0.12 keV using a Gaussian fit.

While the ENC proves a quality rating for the used electronics, one is rarely interested in it alone. Especially in the measurement of nuclei, the response of the system to charged particles is of highest interest. A thin film of lithium-fluoride (produced with an approximate thickness of $\approx 6 \frac{\mu\text{g}}{\text{cm}^2}$) was deposited on a mylar foil and measured at the N4DP instrument (the same sample as used in the calibration described in Section 4.2). The resulting distributions for the α - and ^3H -peaks are shown in Fig. 4.8. While there is no significant difference between the ENC and the measured resolution for the ^3H -nuclei, the distribution of the α -nuclei is significantly wider. From the energy straggling (2.2. keV, calculated with ATIMA) of the α -particles in the detector dead-layer, one would expect a distribution width of $\sigma=6.83$ keV. Therefore the broadening of the distribution is due to the thickness of the thin film. From the distributions width, the LiF films thickness was estimated to be $\approx 4 \frac{\mu\text{g}}{\text{cm}^2}$. This is well in agreement with the thickness of $\approx 6 \frac{\mu\text{g}}{\text{cm}^2}$ estimated from the production process. These values suggest that thicknesses above $\approx 2 \frac{\mu\text{g}}{\text{cm}^2}$ (≈ 8 nm assuming a density of $2.64 \frac{\text{g}}{\text{cm}^3}$) could be measured for this type of sample.



(a) Peak from α -particles ($E_{\text{emission}}=2055$ keV). The width is $\sigma_{\alpha}=8.42\pm 0.22$ keV.

(b) Peak from triton-particles ($E_{\text{emission}}=2727$ keV). The width is $\sigma_t=6.46\pm 0.20$ keV.

Figure 4.8.: Lithium-fluoride thin film on Mylar, measured with the N4DP instrument. The broadening of the α -peak with respect to the triton-peak can not be sufficiently explained with the increased energy straggling of the α -particles in the detectors dead-layer. The broadening is due to the thickness of the measured thin film, which has been estimated to $\approx 4 \frac{\mu\text{g}}{\text{cm}^2}$.

Besides lithium, boron based systems are also of major interest in NDP. To study the depth resolution achievable for boron, a thin layer of B_4C was sputtered on a silicon wafer substrate¹. This sample had a nominal boron thickness of 10 nm. Since it was also used for calibration purposes (see Section 4.2), enriched ^{10}B was used in the sample, to reduce measurement time. Fig. 4.9 shows the measurement of the boron thin film performed at the N4DP instrument. All peaks show the low energy tail characteristic for depth profiles of thin layers. The distribution stemming from the α -particles produced at 1472 keV has a width 7.71 ± 0.09 keV. This is a significant broadening when compared to the ENC. A simple error propagation model (quadratically adding all contributing factors to get the final width of the distribution) yields a thickness of 7 nm for the boron-carbide layer. This is in excellent agreement with the value predicted from the observed count rate. For this method, the count rate was correlated to an amount of boron.

¹ Sample produced by MOVATEC

From the nominal density of B_4C ($2.42 \frac{g}{cm^3}$) the thickness was calculated to be 7 nm. Both methods yield a thickness differing from the thickness given by the producer. Since sputtering processes usually do not deposit material at standard densities (for a similar sample the density was determined to be 80% of the nominal value, see Section 4.2), this difference in results was expected.

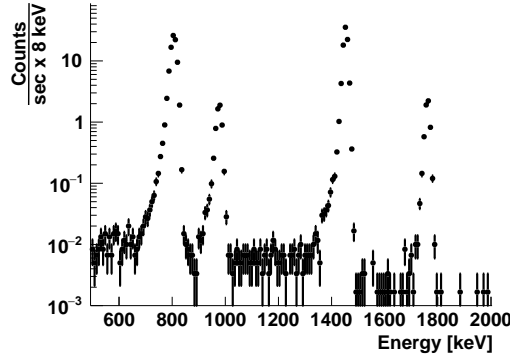


Figure 4.9.: Measurement of a boron carbide thin film performed at the N4DP instrument. All 4 peaks are clearly visible. The low energy tails are due to energy loss in the material layers themselves, and due to the energy loss in the detector’s dead-layer. The thickness of the layer has been determined to be 7 nm. α - as well as 7Li -peaks show a broadening due to the layer thickness.

The 7Li -particles are much more sensitive to the thickness of the B_4C -layer than the α -particles. For the lower energy lithium peak, the distribution has a width of $\sigma_{Li} = 10.65 \pm 0.15$ keV. Using the same propagation technique, the lithium ions would predict a layer-thickness of 10 nm. This helps to illustrate the dangers of such a simplified approach. The actual distribution is not Gaussian, but a trapezoidal function folded with a Gaussian distribution [Tru18]. For very low energy losses, the trapezoid is very thin in energy, and the overall function can be approximated very well by a Gaussian, as seen for the α -particles ($E_{loss} < ENC$). For moderate and higher energy losses, this assumption stops to be valid, and the method can no longer be used.

In the intermediate range, where energy loss is equal to, or slightly larger than the ENC, the determination of thicknesses is not straightforward, even for simple systems. The combination of Gaussians and trapezoids needs to be unfolded in this case, which often necessitates the use of extensive simulations to determine the layer structure and thicknesses of samples. As illustrated in Chapter 2, complex samples already provide extensive challenges in NDP-analysis. Therefore, if feasible, this intermittent energy range (where signals are no longer Gaussian, but can not be approximated by a trapezoidal function either) will not be used for the determination of depth profiles.

For very large energy losses on the other hand, the influence of the ENC and of the energy straggling in the detector’s dead-layer ceases to play an important role. Therefore when energy losses are significantly larger than the ENC and the energy straggling in the detectors dead-layer, getting the width in the spatial frame from the energy distribution is again straightforward (assuming a constant, thick layer of NDP active material) [Tru18].

4.4. Systematic Uncertainties

When dealing with uncertainties in NDP measurements, two general types of uncertainties have to be considered. Uncertainties in the count rates have a direct effect on the deduced isotope concentrations, while errors in energy measurements influence the measurement of depth distributions. While constant errors (for example an offset in the initial intensity calibration) are rather unproblematic, since they do not influence the data (since information will be extracted by comparison to measurements of well known samples), temporal changes in the system can significantly change the conclusions obtained from the data. Therefore great care has been taken at the N4DP instrument to limit and quantify such influences.

Changes in measured energy have been quantified using a long term measurement (more than 15 hours) of a simple boron sample (boron implanted in a silicon wafer). Due to the low background and the high peak, the statistics corresponding to the α -particles emitted at 1472 keV was analyzed. Data were split according to their time stamp in bins with 10 min width. The means of the resulting distributions were extracted and compared to each other. The results are displayed in Fig. 4.10. The fluctuations in energy observed in Fig. 4.10 can be explained by statistical fluctuations. This shows, that temporal changes in energy can be neglected for a single measurement cycle (several measurements undertaken without breaking the vacuum in the chamber).

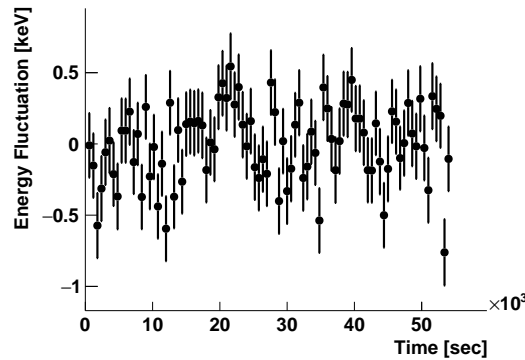


Figure 4.10.: Fluctuations in energy as a function of time. Each data point corresponds to 10 min of measurement (ca. 6800 counts). The standard deviation is $\sigma_E=0.268$ keV. It is dominated by statistical fluctuations, with a $\frac{\chi^2}{\text{NDF}} = \frac{123.26}{89}$. The overall measurement time of 15 hours is similar to the typical time between closing the N4DP chamber and opening it again to exchange samples.

Fig. 4.11 shows two measurements of the same sample performed with several days between them. Data were taken with Setup II and published in [Wer18]. While the fluctuations within one measurement can be ascribed to statistical effects, there is a small shift in the centroid (0.73 keV). Since at the N4DP instrument new calibration measurements are performed after every closing of the vacuum chamber, such changes can be easily detected and, if necessary, corrected for.

Systematic uncertainties in the count rates can be introduced by temporal changes of the neutron flux. The overall power output of the FRM II is constantly monitored, and regulated with a precision of 0.5%. Nevertheless, several effects, like the filling level of the cold source could influence the neutron flux arriving at the N4DP instrument. Therefore the neutron flux at the

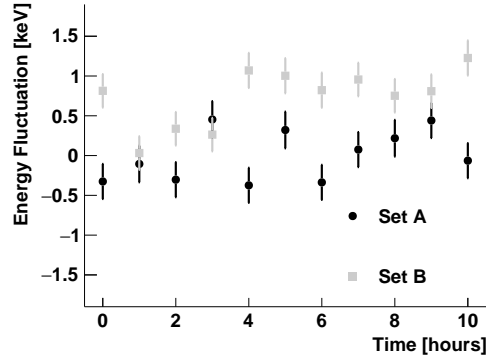


Figure 4.11.: Fluctuations of the measured energy at the N4DP instrument. Data Set B (gray squares) was taken several days after Set A (black dots) using the same sample (SRM2137). Data was taken with Setup II. The energy fluctuations are small, but significantly larger than in Fig. 4.10. This is due to the use of different electronics. Fluctuations are still well below the energy resolution. A shift in the centroid of the two distributions has been observed. It is small at 0.73 keV. Data from [Wer18].

instrument is regularly monitored, using measurements of reference samples. The same data set which is presented in Fig. 4.10 was also monitored for changes in neutron flux by comparing the counts in the equidistant time bins. The result is shown in Fig. 4.12. No statistical significant change in the neutron flux has been observed in the measurement with $\frac{\chi^2}{\text{NDF}} = \frac{104.77}{89}$, although the possibility can not be excluded fully. No trend with time is observable.

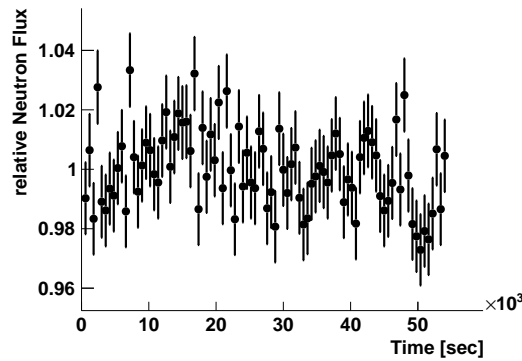


Figure 4.12.: Changes in neutron flux at the N4DP instrument. The standard deviation is 1.32%. The deviation can be explained by statistical fluctuations, with a $\frac{\chi^2}{\text{NDF}} = \frac{104.77}{89}$ and does not indicate a significant change in neutron flux at the investigated timescale.

As shown in Fig. 4.10, Fig. 4.11 and Fig. 4.12, temporal changes in the system have only minimal influence on the measurement results at the N4DP instrument. Regular monitoring helps to decrease this influence further. The main source of uncertainties in energy measurements are the uncertainty of the energy loss model and the uncertainty of the calibration due to this energy loss model and the Pules-Height-Defect. Using a multistack to verify the results, the average systematic uncertainty for energy measurements was determined to be 1.3%.

Systematic uncertainties in the ion concentration measurements are dominated by the un-

certainty of the used calibration samples. The SRM2137, which is the current standard for calibrating NDP measurements, introduces an uncertainty of 3% on the determination of isotope concentrations. This uncertainty is constant for all measurements at the N4DP instrument, since it will only introduce a constant offset, and can therefore be neglected, if no comparison with other measurement methods is desired. For the investigated samples, which have low background count rates, all observed fluctuations in measured isotope concentrations are due to statistical effects. Therefore it can be concluded that only two factors limit the current isotope detection capabilities of the N4DP instrument: Statistical effects can be minimized by increasing measurement times and the active areas of the detectors. The signal to background ratio on the other hand can not be increased as easily. Most background in the N4DP instrument is due to the investigated samples themselves (compare Fig. 4.2) and can therefore not be reduced at will. For thin enough samples (only a few μm thick), a coincidence measurement using detectors at the back and front of the sample can be used. Using, for example, enriched ^{10}B instead of natural boron in the sample preparation also helps to optimize isotope detection limits.

5. Measurements and analysis at the N4DP instrument

When presenting application examples for NDP, battery research is almost always front and centre. Besides this dominant topic, a number of different applications of the technique are also noteworthy. This chapter is organized by presenting boron based applications first. It begins with a basic NDP analysis in Section 5.1. This analysis helps to illustrate the intuitive and straightforward nature of qualitatively interpreting many NDP spectra. It is followed by the investigation of boron containing superalloys (Section 5.2). The corresponding section shows, how careful sample preparation can help to investigate questions normally not answerable with the technique of NDP. The chapter continues with investigations of lithium ion batteries. It not only presents measurements of silicon-graphite based anode systems (Section 5.3.1), but also the first *operando* NDP measurements using liquid electrolyte lithium ion batteries. The chapter concludes with an experimental study into NDP with prussian blue analog based batteries (Section 5.4). Further reading on the research questions investigated at the N4DP instrument can be found in the publications cited in the text.

5.1. Borofloat glasses

Borofloat glass substrates¹ are a commonly used base material in neutron guide production. They are produced by cooling a liquid glass melt on a tin bath, producing a highly homogeneous sheet of glass with very small surface roughness. There is a difference in smoothness between the two sides of the glass. The tin side (the side exposed to tin during cooling) is smoother than the air side (the one exposed to air during cooling).

NDP was used to analyse the boron distribution in glass samples provided by P. Link of the FRM II. For this, raw data of count rates as a function of ADC channels (which correlates to energy almost linearly, as shown in Section 4.2) are compared for the two sides of the sample. Without further analysis a significant dependency between the surface exposure and the boron content was observed, which can be seen in Fig. 5.1. There is a significant depletion of boron on the air side of the float glasses. At 2 μm this depletion vanishes, and the data show a homogeneous boron distribution within the material [Wer18]. This depth was determined through the energy loss of the charged particles in the float glass, which was calculated using ATIMA.

The near surface depletion correlates with an increase in usability for thin film coatings². Thin film coatings are used in neutron guides to create neutron reflectors. These reflectors suffer from strong ageing effects, necessitating regular exchange of neutron guides in research reactors. Therefore, a better understanding of the material properties that make a good substrate for the

¹ Borofloat is produced by the SCHOTT AG, Mainz, Germany

² Private communication P. Link

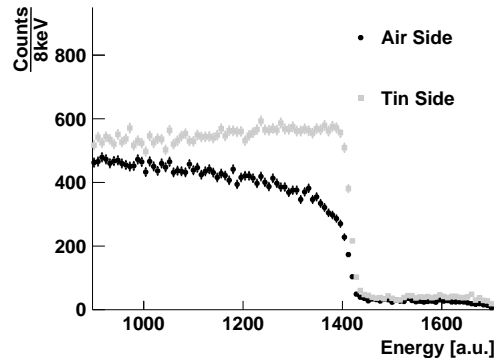


Figure 5.1.: Borofloat glasses measured at the N4DP instrument. A significant depletion of boron in the first few μm can be seen for the side exposed to air (black dots) during production. The side in contact with the tin bath during production (gray squares) shows no such depletion. The slope visible at the tin side is a result of energy straggling and does not indicate a boron gradient within the sample. Data was first published in [Wer18].

typical types of coating used is of great interest in neutron guide production. The glasses have been provided by P. Link.

5.2. Cobalt-rhenium based superalloys

An increase in heat resistance of gas turbines greatly increases their efficiency [Mil96]. Modern high efficiency turbines are mostly based on single-crystal nickel alloys [Per09]. These are currently approaching their limits in terms of heat resistance [Gas08]. Cobalt-rhenium based superalloys provide a possible candidate for turbine materials of even higher heat resistance than single-crystal nickel alloys [Muk10, Muk14]. These alloys consist of a base of cobalt, rhenium and chromium, to which small amounts of tantalum and carbon are added. Traces of boron added to the alloy (50-1000 p.p.m) improve the strength and ductility of the material further [Muk12, Muk14]. An assumption is that the added boron accumulates at grain boundaries in the material. It could then act similar to a glue, by sticking the different grains together, thereby increasing the strength of the material. To test this hypothesis, a series of measurements was performed at the N4DP instrument. Samples were provided by D. Mukherji.

The grain size of the alloy is on the order of $10 \mu\text{m}$. For this type of material, the depth range of NDP for boron is $3 \mu\text{m}$, therefore making a direct validation of the theory with NDP impossible. Fortunately, the alloy can be etched. A controlled etching process is possible, which primarily will dissolve the material at the grain boundaries, thereby allowing for a measurement of the effect. This is experimentally done by comparing a measurement performed with a detector which is positioned parallel to the surface of the sample with a measurement from a detector positioned with a 45° angle relative to the sample surface. If the boron is located primarily at the grain boundaries the detector parallel to the surface should see signals originating from the boron at the bottom of the etchings. The detector positioned under an angle on the other hand should not see this boron, since the ions produced by the $^{10}\text{B}(n,\alpha)^7\text{Li}$ -reaction will be stopped by the additional material they have to pass through (as illustrated in Fig. 5.2). By comparing etched

and not etched samples with each other, it should be possible to see if the boron is indeed located at the grain boundaries.

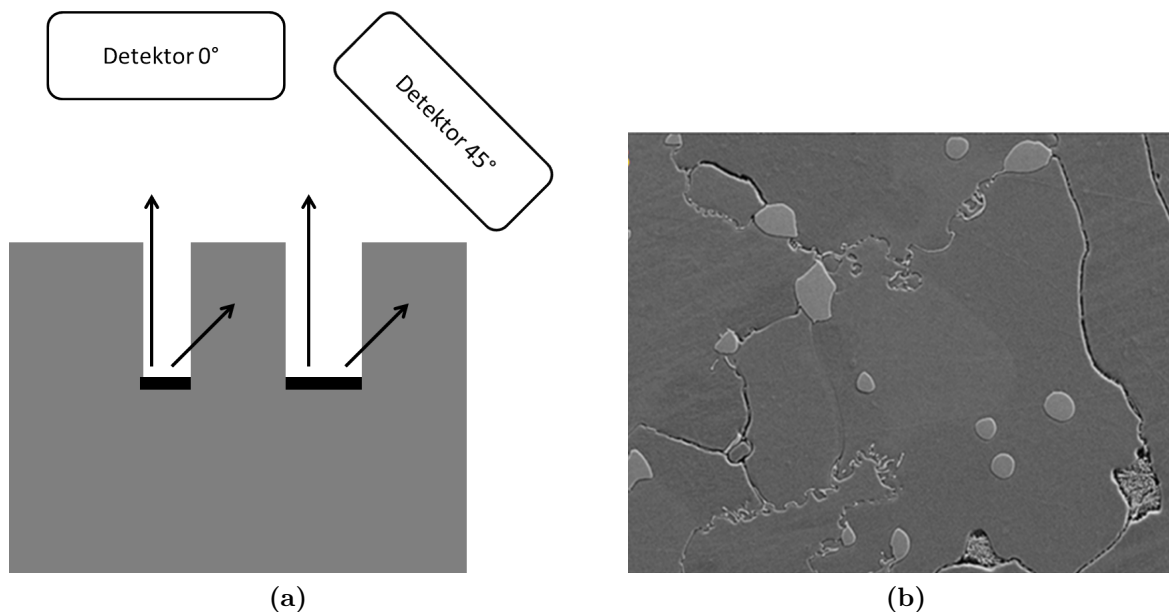


Figure 5.2.: Panel (a) shows the measurement principle employed for the CoRe-alloys. Two detectors are used. One to measure the overall boron content (Detector 0°), and one to determine the boron enrichment at the grain boundaries (Detector 45°). If boron (displayed in black) is located at the grain boundaries, the detector at 45° will detect a reduced signal intensity. Panel (b) shows a photograph of a CoRe-sample. The grain boundaries are clearly visible.

Samples with different nominal boron content have been prepared. For each boron content 3 batches were prepared, one not etched at all, one etched only for a short time, and one batch etched for a long time. These samples have then been measured with two identical detectors which were positioned under the angles mentioned above. By measuring both angles simultaneously, contributions from changes in neutron flux or signal to background rates to the measurement uncertainty can be limited.

For the analysis of the data, several steps have to be undertaken after calibration of the data. First, the (relative) boron content of the etched samples needs to be determined. For this, the measurements from the Detector 0° are used. Due to the exponential background in the measurement, data below a certain threshold (800 keV) was not considered in the analysis, while the data above this threshold can be considered free of background. The integral boron amount was determined for this region and is listed in Table 5.1. The large differences in observed boron content for the differently prepared samples can be explained through the grain structure of the samples. These macroscopic structures have sizes of about $10 \mu\text{m}$. Due to the low penetration depth of the α -particles observed in NDP, only the first μm of the sample can be probed. Therefore, the observed fluctuations are due to local differences in boron content, not due to overall changes.

To account for these fluctuations data need to be normalized. The measured boron content (in Detector 0°) was used to normalize the spectra obtained by Detector 45° . After normalization, the different sample batches are compared. For this, the normalized histograms obtained for the

Nominal [ppm]	not etched [$\frac{atoms}{cm^2}$]	short etched [$\frac{atoms}{cm^2}$]	long etched [$\frac{atoms}{cm^2}$]
0.1	$\approx 2.0 \cdot 10^{15}$	$\approx 3.2 \cdot 10^{15}$	$\approx 3.0 \cdot 10^{15}$
0.4	$\approx 5.8 \cdot 10^{15}$	$\approx 15.4 \cdot 10^{15}$	$\approx 9.8 \cdot 10^{15}$

Table 5.1.: Boron content of CoRe-alloy samples measured at the N4DP instrument. Nominal boron content (determined in the sample preparation) is shown together with the boron contents measured with NDP. Differences in value are due to localized fluctuations in boron content in the samples (only the first μm of the sample can be probed in NDP).

etched samples are divided, bin by bin, by the corresponding spectra of the non-etched samples. The results of this technique for the samples with 100 p.p.m. and 400 p.p.m. boron content can be seen in Fig. 5.3.

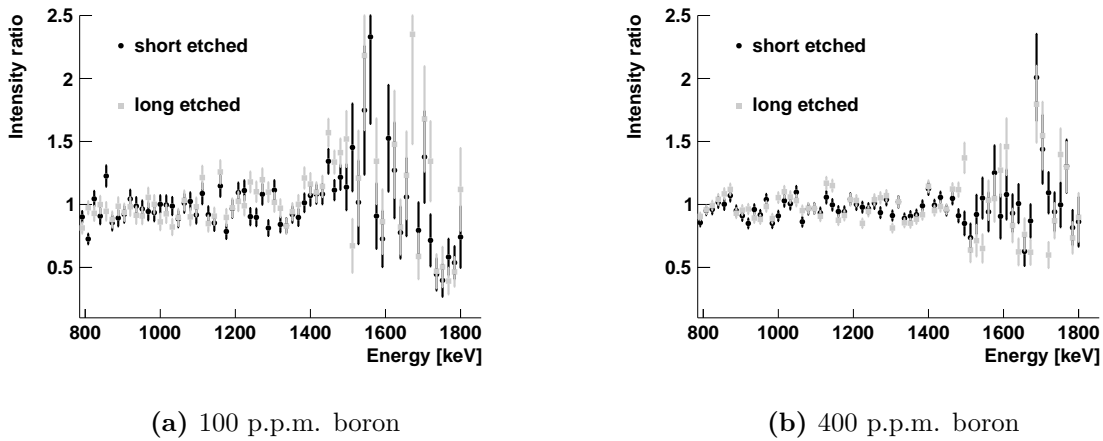


Figure 5.3.: Cobalt-rhenium alloy with 100 p.p.m. (Panel (a)) and 400 p.p.m. (Panel (b)) boron content. Displayed is the ratio between the short etched and non etched sample (black dots) and the ratio between the long etched and non etched sample (gray squares). Within the uncertainties there is no deviation from unity for any of the curves. The larger fluctuations for energies above ca. 1470 keV are due to the lower reaction rates for the 1776 keV α -particles compared to the 1472 keV α -particles.

No dependency between the intensity ratio and the etching process has been found for both 100 p.p.m. and 400 p.p.m. boron content. Assuming that the etching process works as intended (preferably etching away the grain boundaries), these measurements disfavour the theory of strong boron accumulation at the grain boundaries, since no systematic dependency on either boron content or etching processes have been found.

5.3. Lithium ion batteries

The dominant state lithium ion batteries have reached in mobile power provision, leads to intensive research into further improving these devices. Possible improvements mainly concern the capacity density (energy that can be stored in a battery of a certain weight) and charge rate. For this purpose, especially the electrodes and the interface between the electrodes and the electrolyte are of great interest. These thin layers containing lithium, are excellent candidates to

be studied using NDP. Several lithium based battery systems have been investigated at the N4DP instrument [Tru18, Wet18b, Wet19, Lin20, Fra20]. The interested reader will find additional information on the subject in the thesis of M. Trunk (forthcoming).

5.3.1. Silicon-graphite based anodes

Current lithium ion batteries often use graphite as an anode material. To increase the energy density in batteries, different anode materials are under investigation. One candidate is a mixture of silicon and graphite for the anode material. Silicon has a very high specific capacity at $3579 \frac{\text{mA}}{\text{g}}$. When added to graphite, it provides a material mixture suitable for application in lithium battery systems.

When using silicon graphite, two challenges arise. First, the anodes experience a sizeable swelling during charging and discharging, which can lead to an increase in anode thickness in excess of 100 %. Second, current designs of batteries using silicon graphite anodes experience a significant drop in available capacity after a few charge and discharge cycles. Both challenges can be investigated using NDP, since it provides a method to directly track the change in lithium concentration in the anodes as well as being able to track changes in the anodes thickness. Therefore, two campaigns of *ex-situ* studies on silicon graphite anodes were performed. One focused on the lithium intercalation (the inclusion of lithium atoms into the electrode, without a significant change of the electrodes molecular structure) during the first charge cycle, while the second focused on the building of the Solid-Electrolyte-Interface (SEI, a lithium based layer which covers the interface between the electrode and electrolyte and forms during charging) after several charge cycles.

For these *ex-situ* studies batteries were disassembled under a protective gas atmosphere after reaching the desired charge state. The separator (the electrical isolation between anode and cathode, which is permeable to the ions of the electrolyte) was removed from the anode, and the residue of separator and electrolyte (based on LiPF_6 dissolved in fluoroethylene carbonate [Wet18b]) was washed away carefully. For the study of the first charge cycle, anodes were prepared in different States Of Charge (SOC, the amount of charge in a battery relative to its maximum charge capacity) and Depths of Discharge (DOD, how much charge was taken out of a battery, relative to the maximum charge that can be extracted). The anodes were put into the N4DP vacuum chamber immediately, thereby reducing the exposure time to air to a minimum. Exemplary NDP spectra obtained from the anodes are shown alongside with the change of lithium amount between charge and discharge state as determined with NDP in Fig. 5.4.

The NDP measurements show a quite homogeneous lithium enrichment in the anode while charging. The spectral shapes in the discharged states are similar to that of the corresponding charge states. Small differences are observable between depth distributions of corresponding charge and discharge states. This could be an indication for a non optimal design of charge collector and anode. Due to the fluctuations expected from the anode production and extraction process, this is not conclusive.

Two features observable in the NDP measurement might indicate the dominant reason for loss of capacity in the first cycle. One is an overall increase of the lithium content. The second is visible in the peak like feature at the high energy range ($E \approx 2700 \text{ keV}$) of the triton signals. While an overall increase of the lithium content of the sample is expected due to formation of the

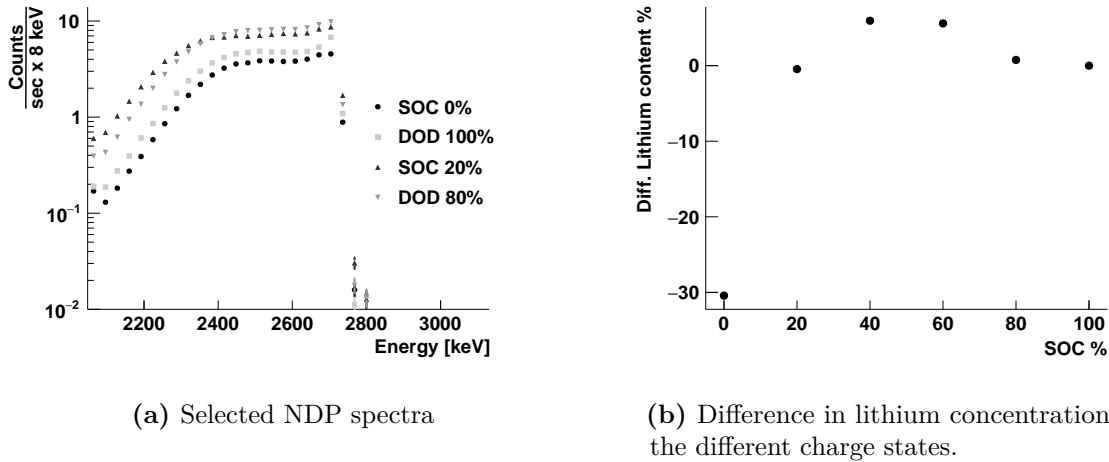


Figure 5.4.: N4DP measurements of Silicon graphite based anodes. While (a) shows the spectra of anodes during charge (SOC 0% = not charged, SOC 100% = fully charged) and discharge (DOD 0% = fully charged, DOD 100% = fully discharged), (b) shows the integral difference in lithium content between equivalent SOC and DOD. A change in the depth distribution during discharge is visible. The formation of the SEI can also be seen clearly. The slight increase in lithium content during discharge for the states corresponding to SOC 40 % and SOC 60 % is most likely due to small fluctuations in the sample preparation. Samples were prepared by M. Wetjen. Data is adapted from [Wet19].

SEI, the peak like structure is more difficult to explain. The samples consist of silicon particles embedded into graphite. Due to the high specific capacity of silicon, lithium will be found mostly at these silicon particles. As shown in [Tru18] this can explain the peak like structure. This is a strong indication, that the capacity loss observed in silicon-graphite anodes is mainly due to lithium bound in silicon which can not be removed during discharge [Wet19].

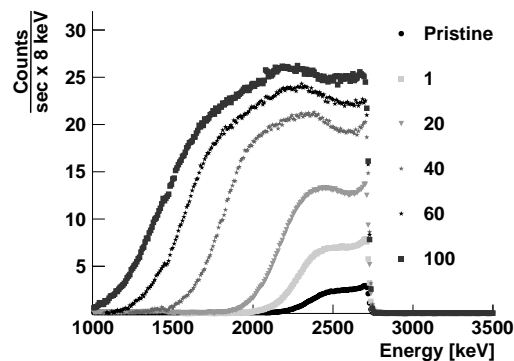


Figure 5.5.: NDP spectra from silicon-graphite anodes measured at the N4DP instrument. Anodes have been charged and discharged for the number of cycles indicated in the plot before the measurement. The signal from α -particles has been subtracted mathematically. The evolution of the SEI can be seen very well. The vanishing of the peak at the onset of the spectrum at high energies indicates a change of sample morphology with an increase in charge cycles. Adapted from [Tru18].

The second study in this regard focused on the effects over repeated charge cycles [Tru18, Wet18b]. For this, anodes were extracted from batteries in their fully discharged state after several

charge and discharge cycles and then characterized with NDP. A mathematical subtraction method introduced in [Tru18] was used to separate the α -signal from the ^3H signal. The resulting spectra, which have been adapted from [Tru18] are displayed in Fig. 5.5. A point of special interest is the behavior of the peak like structure, again observed here for the first few charge cycles. As can be seen it starts to flatten out and finally vanish with an increase in charge cycles. This is due to a change in morphology of the sample. With an increase in charge cycles the silicon particles start to dissolve [Wet18a]. This leads to a vanishing of the peak like structure [Tru18, Wet18b]. This morphology change is strongly correlated to the binding of lithium ions in the silicon particles. Therefore, it can be concluded that the dominant effect in capacity loss is the irreversible intercalation of lithium in the silicon particles. Studying this process for different anode compositions and different structures of the silicon particles might lead to a silicon-graphite anode with higher charge/discharge stability.

5.3.2. *Operando* study of lithium ion batteries

If data at a NDP instrument is time-stamped, temporal changes in isotope distributions within a sample, when charging a battery for example, can be measured. This type of *operando* measurement is of great importance in understanding the dynamic processes taking place within energy storage systems [Wer18, Lin20]. Time resolved NDP can in general be performed with any detector (as long as the detector is viable for NDP). Extracting time information of the kind interesting in NDP experiments (usually in the range from seconds to minutes, for example fast charging of batteries) is usually a feature of current, commercially available digital readout electronics. Time resolution is therefore not limited by electronics, but by the neutron flux available at the experiment. Due to the high neutron flux available at the N4DP instrument it is excellently suited to perform *operando* measurements.

Most NDP instruments use solid electrolyte batteries when performing such *operando* studies [Che18, Ver18, Lv18]. Since liquid electrolyte lithium ion batteries currently present the commercial standard for lithium ion batteries, a special casing to perform *operando* measurements with liquid electrolytes has been designed for use at the N4DP instrument. It consists of a standard battery coin cell, with a grid of small holes processed into the casing. The electrode consists of a thin polyamid foil with copper coating. This foil is thin enough to let the charged ions produced in the anode during NDP escape to the detectors. The design is described in detail in [Lin20].

Due to the vapour pressure of the electrolyte, measurements can not be performed in vacuum. A helium atmosphere is used in these measurements, with typical pressures between 200 and 500 mbar. Pressure is kept constant during the measurements. This setup has been used successfully for NDP measurements of *operando* lithium ion batteries with liquid electrolytes. A typical spectrum of such a measurement is displayed in Fig. 5.6, alongside the integral lithium amount as a function of time, as detected by NDP.

The N4DP instrument is fully capable of *operando* measurements of liquid electrolyte lithium ion batteries. Due to the high flux available at the N4DP instrument, effects below the minute scale can be observed. A more detailed account of the *operando* measurements performed at the N4DP instrument can be found in the thesis of M. Trunk and in [Lin20].

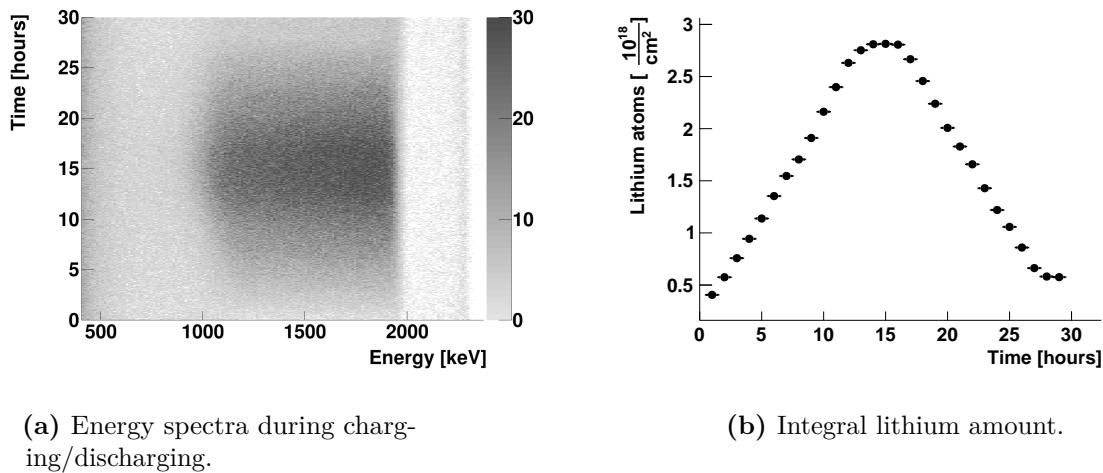


Figure 5.6.: *Operando* N4DP measurements of a liquid electrolyte lithium ion battery. Panel (a) shows the evolution of the lithium distribution over time. The signal from the electrode begins at ca. 2000 keV (due to energy loss in the helium atmosphere and entry window of the battery). The signals at ca. 2300 keV originate from lithium on the entry window of the battery. While the lithium amount increases significantly, no swelling of the battery has been observed. Panel (b) shows the integral lithium amount as a function of time. The battery has been charged, then kept in a charged state for 2 hours and then discharged again. The charge curve is well reflected in the integral lithium amount.

5.4. Prussian blue analog based batteries

Intensive research in the field of large scale energy storage is currently under way [Yan11, Dun11, Sol11]. Electro-chemical systems possess some advantages over other systems, like mechanical energy storage (e.g. pumped hydroelectric). Electro-chemical systems do not require special geographical features (unlike mechanical energy storage), and they promise high round-trip efficiency as well as greater flexibility than current systems [Yan11, Dun11, Sol11].

Lithium ion batteries are in common use in mobile energy storage (smart phones etc.). They have high energy densities [Win98, Tar01, Kan06, Arm08] but they are not suitable for large scale, stationary energy storage due to their high price and the flammable electrolytes of the batteries. To deal with these challenges, two developments are necessary. One is the replacement of the commonly used electrolytes with a different, safer material. The other is the replacement of the expensive materials in the battery with cheaper substance, while simultaneously simplifying the battery design, thereby reducing the price (while worsening the energy density) compared to lithium ion batteries [Ibr08, Luo07].

The use of aqueous electrolytes is promising in this regard. They are inherently safe and environmentally benign and they provide good ion conductivity. Furthermore, since these electrolytes do not have to be processed under protective atmospheres, battery production is simplified when compared to lithium ion batteries [Luo07, Tan13, Li94, Ibr08]. There are many candidates for electrode materials [Wes11, Eft01, Lee04, Deu95, Man06, Sau08, Man11]. Prussian blue analogs are promising candidates for electrode materials for batteries with aqueous electrolytes. They can not only be used for lithium based systems, but also for sodium based systems. Electrodes based on Prussian blue analogs were provided by P. Marzak for the measurement at the N4DP instrument.

Electrodes were prepared with the method and cell described in [Mar]. The electrodes used are NiHCF thin film electrodes. They were charged using a lithium containing aqueous electrolyte (instead of the usual sodium based electrolyte). Electrodes were extracted in different states of charge. After extraction ex-situ measurements were performed at the N4DP instrument.

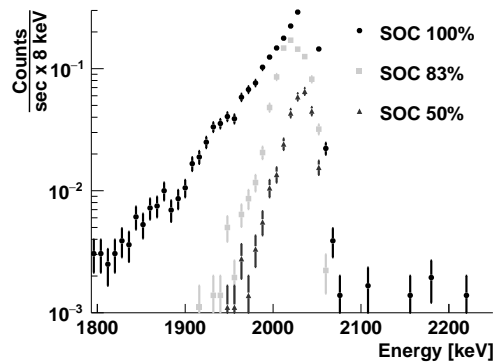


Figure 5.7.: Prussian blue analog based electrodes measured at the N4DP instrument. The electrodes have been provided by P. Marzak. They have been extracted in different states of charge (SOC). The amount of lithium intercalated into the electrodes increases with charge. Changes in spectral shape are also visible during charging. This shows that NDP is a suitable technique to study these novel electrodes ex-situ.

Fig. 5.7 shows the NDP spectra obtained from several electrodes in different states of charge (SOC). The integral amount of lithium in the sample increases with increased charge, as is expected. Changes in the depth distribution are visible, which indicate that the lithium is not intercalated homogeneously over the full depth of the electrode. Future investigation of such thin film electrodes at the N4DP instrument might help to better understand charging and discharging processes in this type of electrode material.

6. Position resolved (4D) NDP

This chapter deals with laterally resolved NDP. While time resolved NDP is routinely used at the N4DP instrument, the implementation of position resolved 4D NDP requires extensive development effort. The different approaches towards position resolved NDP are presented. The chapter continues by discussing the implementation of laterally resolved NDP which is planned for the N4DP instrument. Detailed accounts of the developments undertaken to reach the full 4D capacity are given in Chapter 7 and Chapter 8.

6.1. Position resolved NDP

NDP normally only probes depth distributions, while integrating laterally over the whole beam spot. This is done using unsegmented detectors with high energy resolution [Wer18, Dow95]. Since lateral variations in the isotope distributions might also be of interest, modifications to NDP setups, allowing for laterally resolved measurements, have been implemented in several NDP experiments [Bie73, Bie81, Tom17, Por17]. These setups typically sacrifice energy resolution to gain position information.

Lateral resolved NDP-measurements can be achieved in several ways. The most straight-forward is to use a pinhole-aperture directly in front of the sample [He15b] to collimate the charged particles originating from the sample (collimating the incident neutrons to a fine enough spot is usually not done, since building such a neutron collimator is much more challenging). After a measurement, the target is then moved, with the pinhole remaining at the same position. Thereby, the target plane can be scanned, without the need for position resolved detectors. In this type of measurement, the resolution is limited by the size of the pinhole. This size can not be reduced to arbitrary low levels, since background from β - and γ -radiation will stay constant, while the signal intensity will decrease with the size of the pinhole, which reduces the signal-to-background ratio.

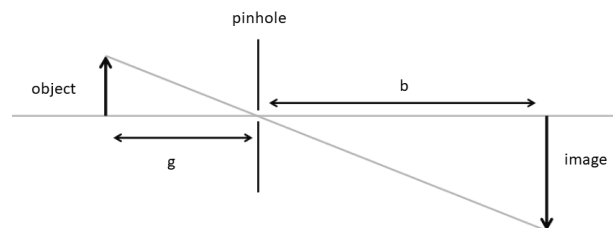


Figure 6.1.: Principle of a camera obscura. The magnification of the inverted image is given by the ratio $\frac{b}{g}$, while the pinhole diameter determines the achievable resolution.

Alternatively, projection techniques can be used. One such technique applies the principle of a camera obscura, as demonstrated in [Por17]. The principle is illustrated in Fig. 6.1 While this type of measurement requires a position sensitive detection method, the rest of the experimental set-up is kept relatively simple. Only one measurement is needed to get a full three-dimensional

picture of the sample. Additionally, moving the pinhole between detector and target allows for different levels of magnification, thereby allowing measurements suitable for a variety of different experimental conditions. Again, this method is limited by the signal-to-background ratio.

This limitation can be overcome by the *coded-mask* approach [Ube03, Gun76]. While the projection is mathematically similar to the camera obscura method, the ratio of hole-size to covered area is much better, and can approach up to 50% of the overall area. This allows for much improved measurement statistics, thereby overcoming one of the significant disadvantages of the camera obscura approach. The *coded-mask* approach not only requires a more sophisticated aperture design, but also requires the use of advanced algorithms to unfold picture and projection functions [Gun76].

An alternative approach is the application of tracking techniques. In this type of measurements, the point of origin of the charged particles is reconstructed by tracking them. The most direct way would be to measure the particle tracks (and then extrapolating them back to the source). Due to the low penetration range of the charged particles observed in NDP, this can not be done with most detectors, since the particles will not penetrate even a single detector layer. This is not the case for gas based detectors where even α -particles will travel distances in the centimetre range. Therefore, the most promising detectors for these measurements would be time-projection-chambers (TPC's). While their spatial resolution is sufficient for those type of measurements, they suffer from quite high dead-time [Ket13]. Due to the high level of background radiation at neutron beam facilities (see Chapter 4), this severely limits the applicability of this technique.

Another approach is to use a kind of vertex reconstruction technique. Therein one uses the back-to-back emission of the two particles. If both particles are detected in position sensitive detectors, kinematic constraints dictate, that the point of origin must lie on a straight line between the two points of impact. Since the production depth in the sample can be determined from the energy loss within the sample, this allows for a precise reconstruction of the reaction vertex. Furthermore, the coincident (in time and energy terms) information collected in both detectors allows to suppress background very efficiently. The most severe limitation of this technique is that both particles have to escape the sample. Due to low penetration depths of the charged particles, this is only possible for extremely thin samples. Considering the options a vertex reconstruction approach is most promising when applicable. When considering projection techniques, the *coded-mask* approach is superior, although more complicated than the *camera-obscura* method.

6.2. 4D implementation at the N4DP instrument

The central premise of the N4DP instruments upgrade is to keep the excellent depth resolution currently achievable. This strict requirement eliminates most position resolved detector systems, leaving silicon based systems as possible candidates (germanium based detectors being not produced with sufficient position resolution). Double-sided silicon microstrip detectors (DSSSDs, sometimes just DSSDs) provide excellent energy resolution, while enabling position resolved measurements with good spatial resolution. They can be produced to cover large areas, thereby improving the angular coverage at the N4DP instrument when compared to the current setup. Furthermore, DSSSDs can be produced from thin silicon wafers ($\approx 100 \mu\text{m}$ thick), thereby reducing background from β - and γ -radiation when compared to other detector technologies.

One of the challenges in fielding DSSSDs in a NDP experiment is the typically thick and inhomogeneous dead-layer of these detectors. This challenge can be addressed through clever detector design. Details on these developments are given in Chapter 8. Besides the dead-layer, also the width of the single microstrip is of importance. Larger strips reduce position resolution and increase count rates per single channel. These introduce pile-up and dead-time, and increase per strip capacity, thereby increasing the noise of the readout channels [Kno00, pp. 631-632].

Therefore, small area strips are preferable. A reduction in strip width, and thereby strip pitch (the distance between two neighboring strips), introduces new challenges in an experiment. Small strip pitches mean a high density of readout channels, thereby limiting the size of the used electronics. The electronics used in the current version of the N4DP instrument (see Chapter 4) are rather large, with a single channel occupying several dozen cubic centimeters for the preamplifier stage alone. While these large electronics allow for very good energy resolution at a wide range of input signals and detector capacities, they are obviously not suited for reading out hundreds or even thousands of channels.

For the N4DP upgrade, configurations using between 158 and 1896 readout channels are planned (see Chapter 8). To cover this wide range, electronics not only need to be small, but also scalable. Application Specific Integrated Circuits (ASICs) can provide a high enough density in readout channels [Lia19, Res19, Ton97]. Many ASICs designed for particle physics applications are designed for high energy physics experiments like the CMS or ATLAS detectors. Therefore, they are optimized for detecting so called MIPs¹, and have a low dynamic range [Fre01] (DNR: defined in [Sly04]). Due to the comparatively large dynamic range necessary for NDP experiments (100 keV to 3 MeV), these ASICs can not be used. Also a good energy resolution is required. Therefore ASICs designed for reading out highly segmented calorimeters are promising candidates for the N4DP upgrade. The Silicon Kalorimeter Integrated Read-Out Chip (SKIROC) [Cal11] ASIC family has been chosen for this upgrade.

¹ minimum ionizing particle, energy loss of a MIP: ≈ 147 keV in $320 \mu\text{m}$ thick silicon detectors

7. Electronics for position resolved measurements at the N4DP instrument

This chapter presents the readout electronics designed for the upgrade of the N4DP instrument to its full, 4D capacity. Due to their excellent resolution and large dynamic range, the upgrade is based on the SKIROC Application Specific Integrated Circuits (ASICs). The implementation of the SKIROC ASICs was guided both by the requirements of the planned upgrade [Ber20] of the TREX experiment at MINIBALL [Bil12], and by the requirements of the N4DP upgrade. This was due to similar requirements on the detectors in both experiments, thereby allowing to combine the design processes of both experiments. The chapter starts with a description of the SKIROC ASICs. It then briefly sketches the development of the hardware. The circuit boards designed for the readout of the detectors are described in Chapter 8. The description of the GEAR-board is kept short on purpose (the thesis of C. Berner provides a more detailed account). Having been developed in the scope of this thesis, the firmware is described in detail. The chapter concludes with a discussion of the systems capability, with a focus on the firmware performance and achieved resolution.

7.1. The SKIROC ICs

The readout channel density of the SKIROC ASICs [Cal11] is sufficient, at 64 channels per ASIC ($7.1 \times 8.5 \text{ mm}^2$ as bare die). SKIROC ASICs are designed with both an analog and a digital part. Digitization of data is performed using a 12-bit Wilkinson ADC. 32 kbit of Random Access Memory (RAM) are used to store data pre-readout. The ASICs are designed for low power usage. They can be triggered externally, or use an internal trigger. SKIROCs provide both an energy and a time signal, via internal ADCs, Time to Digital Converters (TDCs) and Time to Amplitude Converters (TACs). The dynamic range is 0.4 fC to 10 pC. SKIROC ASICs are designed for operation with a pulsed beam structure.

The analogue stage consists of a tunable preamplifier, which supplies the signals to a fast CRRC shaper, used for timing and trigger information, and two slow shapers. The slow shaping amplifiers have a gain of 1 and 10, thereby providing a low gain and high gain branch. The fast shaper has an adjustable gain and adjustable shaping time. A 10 bit Digital to Analogue Converter (DAC) provides the trigger threshold. This threshold is fed into a discriminator which produces a trigger signal using the signal from the fast shaping branch. Additionally, each of the 64 channels has an adjustable 4 bit DAC, which is used for compensating offsets between the channels. The block diagram for the analogue part of the SKIROC 2A ASIC is shown in Fig. 7.1.

The SKIROC 2A ASIC is designed for positive polarity only, and has a good resolution and readout speed. The CMS is designed for both polarities, and normally works in a *trace-mode*, meaning that it will record a long trace (detected signal heights for multiple times, similar to an oscilloscope) of one event upon receiving a trigger. This constrains the maximum readout speed possible and would limit its applicability at the N4DP instrument. Details on circumventing this

mode and increasing the readout speed (and thereby the maximum rate measurable) can be found in Section 7.3.

7.1.1. The SKIROC 2A

The SKIROC 2A is designed with charge sensitive inputs which accept signals of positive polarity. Every input is connected to charge preamplifiers which consists of a p-type metal-oxide semiconductor (PMOS)-transistor followed by a cascode configuration (cascode configuration: see for example [Hun39]). It is optimized for a detector capacity of 20 pF. For this capacity, the ASIC has an Equivalent Noise Charge (ENC) of ≈ 1500 electrons, making it suitable for high resolution silicon strip detectors. The feedback capacity can be set using the ASIC's slow control to values between 400 fF and 6 pF.

The fast channel uses an amplifier with gain of 10, followed by a variable shaper. The shaper's peaking time can be set by slow control between 30 and 120 ns. Next is a low offset discriminator. Its threshold is set by a combination of a 10 bit DAC common to all channels and a 4 bit DAC for each channel. This configuration allows for adjustments of trigger thresholds between the channels, to correct for individual offsets. The output of the discriminators is fed into an 8-bit delay box, enabling delays between 100 ns and 400 ns for the triggers. The triggers of each channel are then combined using or-gates.

Two slow shapers, with peaking times of 180 ns and gains of 1 (low gain) and 10 (high gain) are used for the energy measurement. When the trigger signal is given, the signal of the slow shapers is fed into a switch-capacitor-array (SCA). The minimum time needed to distinguish between two events in the SCA is 70 ns. The SCA has 3 track and hold cells, each with 15 capacitors. They are used to store low gain, high gain, and time measurements. The SCA can save 15 events. Fig. 7.1 shows the block diagram for the analogue readout chain of a single channel.

When a readout order is sent to the SCA, the analog data is sent to a multiplexer. Depending on the slow control configuration of the ASIC, either low gain and high gain, low gain and time, or high gain and time will be passed from the multiplexer to the internal 12/10 bit Wilkinson ADC (Wilkinson ADC: see for example [Kno00]). In the 12 bit mode, the conversion time for 64 data values is 100 μs , leading to a maximal conversion time of 3 ms for all SCAs of all channels of the ASIC. In 10 bit mode, conversion time is reduced by a factor of four, with a maximum conversion time of 750 μs .

The data from the conversion is stored in a 32 kbit memory, which is of sufficient size to store the gray encoded ADC data, which is expanded with status bits to 16 bit per conversion, together with coarse timing information and an ender word. After the conversion is finished, analog data taking can start again. The data in the digital memory can also be read out, once the conversion is finished. By default data is transmitted using a bit rate of 5 MHz. There is one single data line giving an overall data transport time (at 5 MHz) of 6.2 ms. The data structure of the SKIROC output is displayed in Fig. 7.2.

As can be seen from these specifications, the SKIROC 2A was designed for pulsed beam operation. Up to 15 events can be saved with almost no dead time, while the conversion and readout take significant time. As is shown in Section 7.3, the readout speed can be increased significantly.

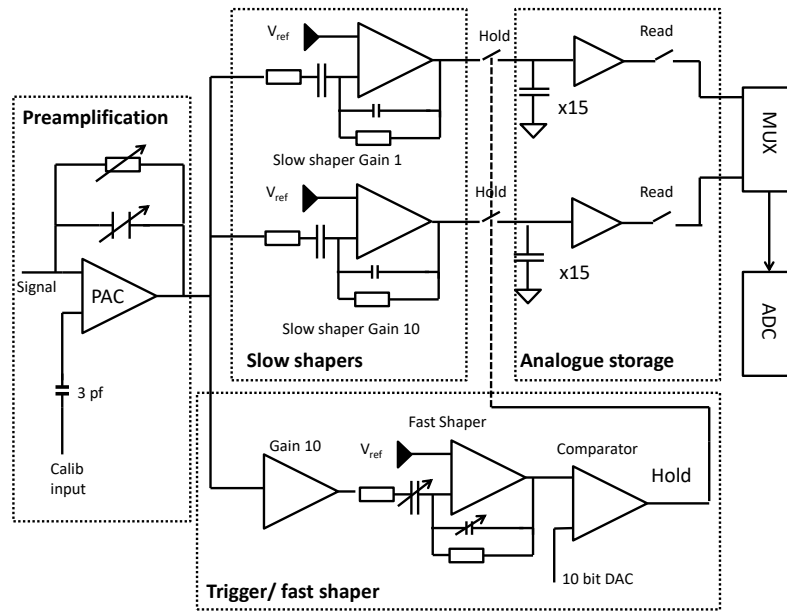


Figure 7.1.: Schematic for the analogue readout chain of a single SKIROC 2A ASIC channel. PAC indicates the preamplifier of the channel. Both high gain and low gain slow shaping stage are shown. The trigger branch with the fast shaper is marked.

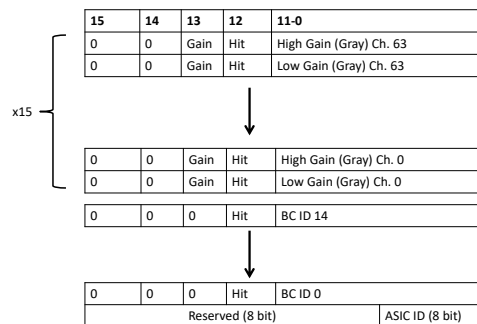


Figure 7.2.: Data structure of the SKIROC 2A ASICs output. The ASIC has been configured to output both high gain and low gain data.

Since one of the planned upgrades of the N4DP instrument includes bunching the neutron beam to reduce background count rates even more (NDP reactions are almost instantaneous, while the emission of γ - and β -radiation due to neutron capture reactions has longer time scales), the design of the SKIROC 2A is advantageous.

7.1.2. The SKIROC CMS

The SKIROC CMS ASIC is similar in design to the SKIROC 2A ASIC. Contrary to the SKIROC 2A ASIC it can handle both positive and negative input polarity. Due to the similar design

and characteristics of the two ASICs it was decided to use the SKIROC CMS ASIC to read out negative polarity signals from the detectors. The SKIROC CMS ASIC is a prototype ASIC with several characteristics that make it necessary to use it to complement the SKIROC 2A ASICs instead of completely replacing the 2A ASICs. Among those are both slightly worse resolution as well as lower default rate capability, as detailed in this section.

The CMS uses preamplifiers similar to that of the 2A. Its preamplifiers are combined with an inverter, to allow operation with both signal polarities. As in the 2A, the CMS possesses two slow shapers with gain 1 and gain 10. The trigger signal of the CMS starts the data taking procedure. After the trigger, data is written to a new SCA with every clock tick of the so-called roll-clock, until all SCAs are filled. This means, that the CMS will write a *trace* into its analogue memories. 13 SCAs per channel are used to store the data. Therefore, the CMS will save the shaper output from the first 325 ns after the trigger with a granularity of 25 ns.

While the fast shapers are similar to the ones of the 2A, the CMS has additional TACs. These are used to provide time-of-arrival (ToA) and time-over-threshold (ToT) signals. Due to the CMS being designed to only save one event, a ToA and ToT signal can be saved for each channel. As in the 2A, the data are multiplexed and then digitized with a Wilkinson ADC. The gray encoded data is saved in a 4 kB digital memory.

Due to the difference in architecture, the data structure of the CMS differs from the data structure of the 2A. CMS data are grouped according to ADC conversions. A single conversion contains a data word from each of the 64 channels. The conversion arriving first contains the data from the low gain shaper branch at the first tick of the roll-clock. It is followed by the high gain data from the same time. After that, the conversions of the second clock tick follow. This is continued, until all 13 energy SCAs are read out. After that, the ToA information for every channel follows. The first 64 data words are the ToA taken at the falling edge of the clock, while the next 64 are taken at the rising edge of the clock. This data is followed by the ToT informations for each channel, taken with slow and fast clock. The data are completed with 4 header words, containing time stamps, the ASIC identification, and the information on which SCA entry contains the trigger.

7.2. Hardware implementation

The spatial constraints at the MINIBALL experimental site (for which this system is also developed, see [Ber20]) require very compact front-end electronics. This was realized by using a six-layer printed circuit board (PCB)¹ which houses both detectors and SKIROCs. Advanced manufacturing techniques were used on the board. These include z-axis milling with in-layer bond pads, ultra fine pitch connectors, high density traces, and filled and capped micro-vias.

The detector board is connected to a vacuum feed-through using a flex-PCB with high density connectors. This feed-through is a PCB which is glued into a vacuum flange using a 2-component epoxy resin. A ten layer backplane PCB is connected to the feed-through. This backplane supplies the connection points for the bias voltage of the detectors, as well as the option of connecting an external pulser to perform a channel-by-channel calibration. Directly connected to the backplane is

¹ produced by IV-Schaltungen GmbH, Allerhausen, Germany

the so-called GEAR (GEnericAsicReadout)-board. A photograph of the board is shown in Fig. 7.3.

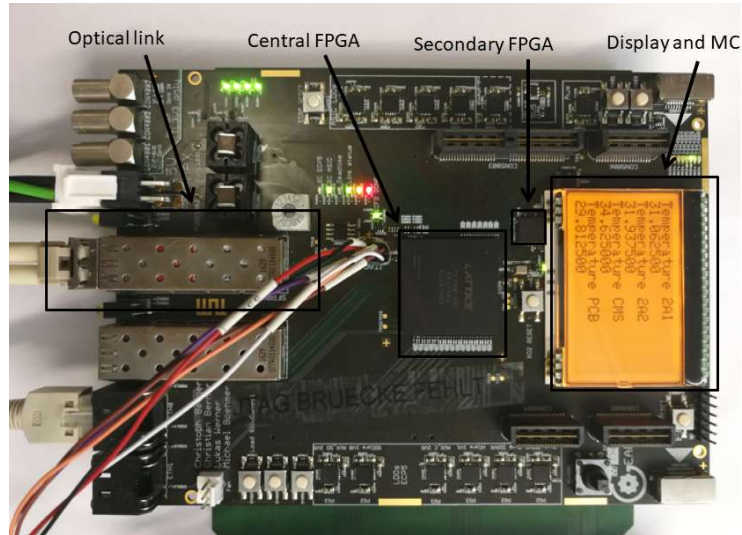


Figure 7.3.: Photograph of the GEAR-board. Important parts are labelled. The microcontroller is located behind the display.

The GEAR-board houses a central Field-Programmable-Gate-Array (FPGA) of the type ECP5-UM¹. This FPGA is used for controlling the ASICs, (pre-)processing the data and for communication with the back-end data acquisition. Communication with the Back-End is done via a Serializer/Deserializer (SerDes) interface. The UDP-protocol is used for communication of the interface with the Back-End (via optical fiber). Besides the central FPGA, a second FPGA (MachXo2¹) is used in a watch dog function, resetting the central FPGA if some major error should occur. Besides the two FPGAs also a microcontroller (MC), the STM32 F7671T6² is placed on the GEAR-board. It serves as a controller for the on-board display, as a debug interface, and it can be used as a on-board pulser for calibration of the SKIROC ASICs via its internal DAC.

As a Back-End, the TRB [Krz08] system was chosen. The TRB (*"what does TRB mean? You can choose between: TDC-Readout-Board, Triggered-Readout-Board and Triggerless-Readout-Board"*³) was originally designed for the High Acceptance DiElectron Spectrometer (HADES) which is located at the Gesellschaft für Schwerionenforschung (GSI). The highly modular TRB framework provides an interface between the DAQ-PC and the various end-points by using standardized Back-Ends and firmware modules for readout triggers, data transport and slow-control. The modular architecture allows for easy scaling of (sub)systems. The TRB supports DHCP, making integration of the system into a network straightforward. A number of add-ons exist for various tasks, including for synchronizing the TRB system with an external clock.

¹ produced by Lattice Semiconductors

² produced by STMicroelectronics, Geneva, Switzerland

³ trb.gsi.de

The GEAR-board is fully implemented in the TRB-network. The GEAR therefore provides a standardized platform for readout of ASICs with a digital interface, as well as supplying power at standardized voltage levels for ASICs that might be combined with the system. Furthermore, the MC provides an easy-to-use interface to the TRB network, which does not require any knowledge in FPGA-programming to use. In the case of the SKIROC ASICs a powerful firmware framework provides multiple control and usage options for a wide range of different applications.

7.3. Firmware: Controlling and readout of the SKIROCs

Since the system is fully integrated into the TRB-framework, the firmware also employs several of the modules common to TRB-implementations. First and foremost is the use of the TRB media interface [Mic] for communication between the TRB-network and the custom firmware on the GEAR-boards. Furthermore, the TRB-bus-handler provides a common bus for all slow control (slctr) registers used in the GEAR-firmware. Communication with the nand-flash memory on the GEAR is performed with the trbsec-tools library. All these are described in detail in [Mic] and [Kor].

The GEAR-firmware uses 3 data-interfaces to the TRB, one for each SKIROC-IC. They are configured to be able to hold at least one maximum sized event each. Data is configured in 32-bit words and is fully clock-synchronous with a 100 MHz clock. The default endpoint ID of the GEAR-boards is 0xfdec. A broadcast option is supported, allowing all boards to be simultaneously addressed using the 0xfffc broadcast address. The full list of slow control registers available can be found in Appendix B.

The default application of the GEAR-board is to control two SKIROC 2A and a SKIROC CMS (CMS) ASICs. Therefore three top level entities are used for ASIC control. An entity is a functional unit in VHDL based firmware design. It contains a list of ports (connections to other entities and/or the physical in-and outputs of the circuit) and an internal architecture. An entity might contain any number of sub-entities within it. These entities are used to perform the ASIC-slctr, retrieve, timestamp, preprocess and save data, and to provide the necessary control and data outputs to the TRB-interfaces.

Besides these large firmware entities, the top level of the FPGA design also contains several phase-locked-loops (PLLs), a 200 MHz timestamper unit, provides control and status outputs, communicates with the on-board micro-controller (MC) via a Serial Peripheral Interface (SPI), and contains numerous logic gates for decision making, and allows to directly switch off and reboot any IC on the GEAR.

As described in Section 7.1, both the 2A and CMS ICs have limitations concerning the maximum readout rate possible with these ASICs. While the energy resolution, dynamic range and instantaneous rate is high for the 2As, the integral readout rate is severely limited. The conversion time can be reduced by switching to the internal 10-bit ADC (which of course reduces resolution). But the limiting factor is the readout speed, at 5 MHz. The CMS on the other hand, possesses a higher readout speed, but is designed to save traces of events rather than several single events. While this is useful in detectors with long rise and fall times, DSSSDs have fast timing constants, with signals reaching their maximum in less than 25 ns.

7.3.1. Data state machines 2A

Two state machines are used to control the 2As. The first one is used for controlling the acquisition of new events and for controlling the conversion of the analog data in the SCAs to digital data in the RAM. The second is used for transmitting these data to the FPGA. Both state machines perform handshake protocols with each other and with the rest of the system.

Once the Acquisition part of the firmware is enabled (via slow control or by an external signal) the ASIC will start to take data. Once the analogue memory of the ASIC is full, or an external signal is given to the state machine, conversion of the data will start. When the conversion is finished, the data transmission is started. Once all data has been converted and saved in the RAM, the ASIC will request to be read out. The transmission state machine starts the readout. Once all data have been transmitted, the Acquisition can start again.

To optimize the data rate of the 2A, the best approach is to work with the digital part of the ASIC (since analog timings are mostly given by charge times of capacitors). Variable clock speeds were implemented. For this, two clocks, one at 5 MHz speed (as given in the data sheet), and one at 40 MHz, are connected to the same output pin of the FPGA. Once the transmission state machine detects a readout request from the ASIC, it will enable the 40 MHz clock on the output pin, thereby switching off the 5 MHz clock (which is assured through AND and NAND gates). This overall process can be enabled or disabled via slow control.

7.3.2. Data state machines CMS

The state machines used to control the data acquisition and transmission in the CMS are similar to those used for the 2As. The main difference concerns the data taking decision. While the 2As are always used in their self triggering mode, a different approach was taken for the CMS. In normal *trace-mode*, the CMS fills a SCA for every tick of the so called roll-clock, which is registered after a trigger was detected.

This mode strongly limits the maximum data rate possible for the CMS. To deal with the readout speed issue, a new data taking mode, the so-called *singles-mode* was created. For this, the CMS is triggered externally, using the trigger from the 2As. The trigger is passed to the CMS on the trigger line, and the first tick of the roll-clock is enabled simultaneously. The roll-clock will then be kept inactive, until the next trigger from the 2As is registered. This trigger does not produce a trigger signal, but only a tick on the roll-clock output, thereby filling the next SCA. This procedure is continued until every SCA contains an event, thereby increasing the analog buffer size from 1 to 13 events. Due to the ASICs design only 11 of the 13 SCAs contain useful information when read-out in *singles-mode*. The index of these SCAs is constant for each data set, and they can be easily identified using the roll clock information provided in the data stream (the SCAs in question are also well visible when checking the data, since they will contain only noise). In *singles-mode*, the firmware handles these two SCAs by producing artificial (non-physical) triggers to fill both SCAs. Therefore, the impact on the overall rate is minimal (both SCAs are filled within a few 100 ns), and no physical events get lost.

After these events are transmitted (with 40 MHz), the acquisition state machine will be active again. The next event will now again produce a trigger signal and a tick of the roll-clock, thereby

starting the data taking process anew. Slow control registers enable the switching between internal and external triggering, as well as between using *trace*-mode and *singles*-mode. Logic gates ensure that the trigger decision is set correctly when *singles*-mode is used. Another register enables the forced readout of the SKIROC 2A ICs once the SKIROC CMS has saved 13 events. This allows to limit overall system dead times, by forcing all three ASICs to a simultaneous conversion and transmission cycle.

7.3.3. Data Processing

For both types of ASICs, received data is fed into a 16-bit ring-buffer. To ensure clock synchronization in the FPGA, incoming data is oversampled and synchronized using edge detection. Once 16-bits have been received, data is copied to a shadow-register. While data taking in the ring-buffer continues, the shadow register is written to a First-In-First-Out memory (FIFO), the PreFIFO.

Once transmission is finished, data from the PreFIFO is taken to the next stage of processing. To ensure data integrity, no further transmission is possible, until the PreFIFO filled by the shadow register is empty. Since the data word depth is 16-bit, and since the PreFIFO is read out with 100 MHz, emptying the PreFIFO takes only $\left(\frac{1}{64}\right)^{\text{th}}$ of the time it takes to fill it.

Data from the PreFIFO is processed by a secondary firmware module, the so-called reducer. While this module can in theory be used to remove data not containing physical hits (the option is implemented and can be switched on via slow control), the high clock speed (compared to the ASICs) and extensive buffering in the FPGA make this option unnecessary. Since the TRB is working with a 32-bit standard, and since the SKIROCs use 16-bit words, the reducer adds additional information to the data words. This additional information contains an identifier for the ASIC which transmitted the data. The reducer also adds the word number to the data. This means, that every 32-bit word contains the full information of its origins, without needing any additional data structure. There are several slow control options to configure the reducer. It allows for debug modes, to pre-process the data from gray-decoded to binary-decoded data, and to throw away data-words were the hit bit has not been set by the ASIC (therefore its name). Data pre-processed by the reducer is fed into another FIFO. Once the process is finished, both the transmission module and the following processing module are started.

Following the reducer is the HEADER-adder. Upon receiving the information that the reducer is finished, it will start. First, a TRB-standard compliant header word is produced, containing the number of words that will be written to the TRB data interface, as well as a unique ID, detailing which ASIC has sent the data. After that, the times of each trigger received from the ASIC (timestamped with a 200 MHz clock) are added to the data (in 64-bit packages). To synchronize an arbitrary number of boards, an external signal can be provided to any GEAR-board. The timestamp of this signal is added (again in 64-bits) next. The time of the TRB-reset (in a TRB-compliant standard) is sent in the next word and in the lower 8 bit of the word after that. The 16 higher bits of this word contain the temperature of the temperature sensor positioned directly under the ASIC. After that, a status word is provided, containing information on the current slctr configuration of the ASIC (such as gain, trigger threshold, shaper time constant ...). This is followed by the ASIC data (retrieved from the FIFO filled by the reducer), and completed with a predefined ender word. This word is used as an additional marker, to ensure

data integrity in all possible situations (but is in principle redundant, since the length of the event is also transmitted). The data structure produced in this way is illustrated in Fig. 7.4.

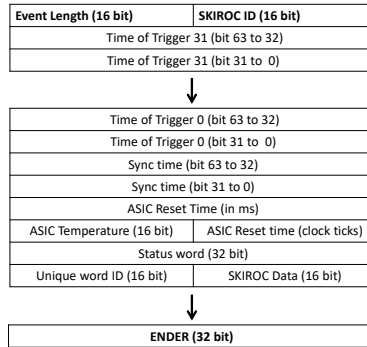


Figure 7.4.: Data structure after HeaderAdder. The ENDER is a fixed word (0xffffffff) used to ensure that all data is sound and has been transmitted fully. It is a redundant safety feature.

When the HEADER-adder is finished, a readout request is sent to the TRB. Should no readout trigger arrive from the TRB within 0.66 ms, then the request is sent anew. After a trigger has been received, data is sent to the TRB endpoint. Should a readout trigger from the TRB arrive, which has not been produced by the electronics associated with the respective ASIC (e.g. from a different GEAR-board), two situations are possible. If no data is present, or the HEADER-adder is active, the trigger will be accepted immediately, and the datafinished signal will be set on the TRB trigger bus, immediately releasing the trigger bus. If data is available immediately, it will be sent on the spot. While the HEADER-adder is active, the reducer is not allowed to take data. Same, if a TRB-readout request is currently processed, the HEADER-adder will not start processing data. All in all, this configuration allows to buffer up to three full ASIC data blocks in the FPGA.

7.3.4. ASIC Slowcontrol

Besides ASIC control, data storage, trigger handling, time-stamping, configuration logic and communication with secondary devices, the GEAR-firmware has multiple debug options and interfaces, and of course also allows for the slow control configuration of the ASICs. The 2A and CMS ASICs are configured using a Serial Peripheral Interface (SPI). It uses a pre-set SPI-mode (mode 0) and the ASIC is the SPI-slave. On the Master-Out-Slave-In (MOSI) data line, the configuration which the ASIC should load into its configuration registers is transmitted. On the Master-In-Slave-Out (MISO) line, the current content of these registers is transmitted.

The 2A slow control has a total of 616 bit, while the CMS can be configured with 384 bit. The bits are only identified by their position in the MOSI and MISO data streams. When the slow control is sent to the ASIC for the first time after a reset or power up, the data stream received on the MISO line will contain the arbitrary content of the registers. To check if the slctr has been loaded correctly, the slow control has to be loaded twice. The GEAR-firmware will compare the data sent to the ASIC with the data received on the MISO line. If those are identical, the SlowControlLoaded bit will be set, and the corresponding light emitting diode (LED) on the

GEAR-board will be switched on.

For usability, the slctr of the ASICs can be configured through TRB-slctr registers which are automatically sorted by the FPGA into the correct order. This allows a high degree of order and ensures compatibility with the 32-bit architecture of the TRB-network. In practice this configuration is normally automated using a script to load the numerous registers with the values desired by the operator of the data acquisition.

7.3.5. Data readout

Once data is collected by the TRB-backend, it is packaged and sent via the User Datagram Protocol (UDP) on an optical fiber link to the DAQ-PC. There the dabc (data acquisition backbone core)-software package [Ada08] is used in the TRB-compatible hadaq (HADES data acquisition) configuration. It collects data and saves the data to the DAQ-PC. While unpacking of normal TRB events is straight forward, the data structure inherent to the SKIROC ASICs demands additional treatment.

First, the TRB data is unpacked. With each event every GEAR-board will send data from 0 to 3 ASICs. The events do not have to be ordered by time between the different ASICs, much less between different boards. The first step of the unpacking is to sort the ASIC event packages by ASIC board and TRB trigger info in specific ROOT-trees, disentangling header informations and ADC data from each other, while also saving TRB header data.

The ROOT-tree produced in this way is then separated into three trees, one for each ASIC. Each physical event gets its own entry in this tree, thereby splitting up the bunched data structure of the SKIROCs. If several GEAR-boards are involved in the data taking, these trees will contain events from each board, but only from one predefined ASIC of that board (e.g. data from the CMS ASICs of every board). These events are sorted by their time-stamp, producing a time sorted tree.

These three resulting trees are then combined, and during combination they are sorted again, as to produce a single, time sorted tree of all events. This tree is then taken and events are correlated with each other, thereby providing a final output of correlated events. A short summary of the overall unpacking and sorting work flow is shown in Fig. 7.5

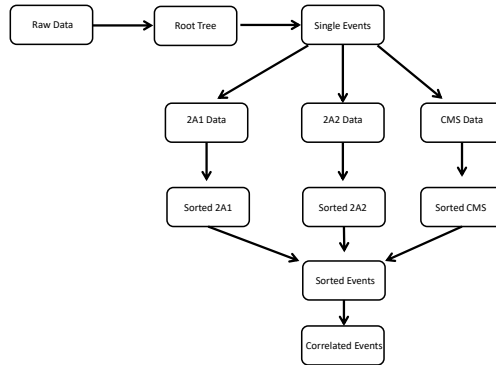


Figure 7.5.: Full work flow of the unpacking software. Arrows indicate programs while boxes indicate data structures.

7.4. Performance

7.4.1. Event rate and deadtime

While the SKIROC ICs have an extremely high instantaneous rate capability (with a minimum of 70 ns between two subsequent events), due to conversion and transmission times, the continuous event rate is much lower. In standard operation (12-bit ADC, 5 MHz transmission rate), the full conversion and transmission of a 15 event package of the SKIROC 2A will take about 6 ms. When switching to higher transmission rates (40 MHz), this time can be cut down. To verify the reduction in dead time, a pulser was connected to one of the 2A ASICs. The pulser rate was varied between 20 Hz and 100 kHz, and the transmission data rate was set to 5 or 40 MHz. The event rate detected by the ASIC was then reconstructed using the run times of the sub-data sets and the amount of events in those sub sets. The resulting distribution of trigger efficiency as a function of the pulser rate is displayed in Fig. 7.6.

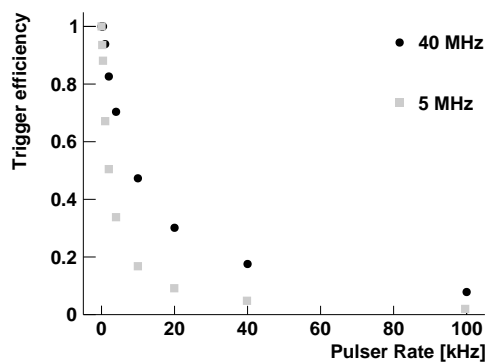


Figure 7.6.: Trigger efficiency (accepted/received pulses) as a function of pulser rate for 5 MHz and 40 MHz transmission rates. Pulses were set to be equidistant in time. The influence of the transmission rate on the trigger efficiency is especially stark in the region between 5 and 40 kHz. In 40 MHz transmission rate, the 2A trigger efficiency is 50% at a pulser rate of 10 kHz.

As expected, the efficiency is much higher for 40 MHz transmission rate. Still, the overall

rate remains limited by the conversion time of the ADC, which can not be optimized without reducing the resolution. An increase of the transmission rate would be thinkable, but due to the electronic characteristics of the ASICs, the signal quality of the transmission starts to significantly deteriorate at higher rates, leading to miss-identified bits. For the N4DP upgrade, as well as for the MINIBALL upgrade a pulsed beam structure will be used, increasing the overall possible rate significantly (since 11 Events can be taken within 910 ns by one GEAR). Therefore no further optimization of the readout rate is necessary.

7.4.2. Resolution

The resolution achievable with the ASICs was measured for several pulser signals of different heights. By providing realistic signals, these allow for a precise determination of the SKIROCs contribution to the overall energy resolution. No dependence of the measured resolution on the pulser height has been found. An exemplary measurement is presented in Fig. 7.7 which shows a pulser input signal equivalent to an energy deposition of 3194 keV in a silicon detector. The signal has a width of $\sigma=4.46$ keV. Since even detectors with thinnest dead-layers have a worse intrinsic resolution when used for NDP-measurements (as shown in Chapter 4), the SKIROC 2 ASIC easily has a good enough energy resolution to be used for NDP measurements.

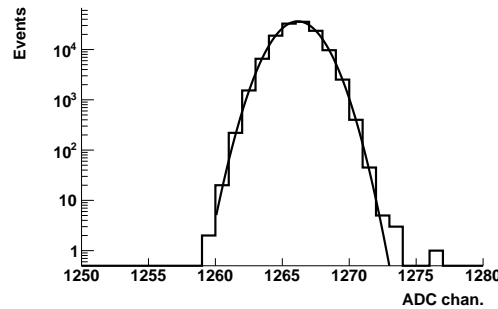


Figure 7.7.: Measurement of a pulser with a SKRICO 2A. The pulser height is equivalent to 3194 keV, with a resolution of $\sigma=1.445\pm 0.003$ ADC chan., or $\sigma=4.461\pm 0.009$ keV determined by a Gaussian fit. Data was taken at an ASIC temperature slightly below 20°C. The data for every SCA is presented in the Appendix in Fig. C.1

The SKIROC-CMS will be used for the readout of the back-side of the DSSDs. As such, the resolution does not play an important role, since the energy will be reconstructed with the 2A-ASICs (which have a lower ENC than the CMS). A measurement of a pulser input signal performed with the CMS is shown in Fig. 7.8. In this measurement the CMS ASIC was used in *singles*-mode. It was triggered by the 2A, which received a pulser simultaneously with the CMS. The resolution is comparable, but a little bit worse than that achieved with the 2A. Nevertheless it is more than sufficient for the planned usage of the CMS-ASICs.

Besides the resolution for a single channel with a pulser input, the pedestal of each channel can also be monitored. This is especially interesting with respect to insufficient power supply to the preamplifiers, since these would lead to a change in the pedestal position as a function of the ASIC channel. If power supply is constant over all channels, only small fluctuations between the channels due to small differences in the feedback resistors is expected. Exemplary pedestals of

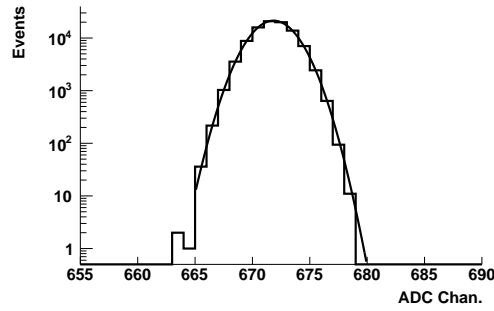


Figure 7.8.: Measurement of a pulser with a SKRICO CMS. The ASIC was set to *singles*-mode and triggered by the 2A ASIC. Shown is SCA 4. Data was taken at an ASIC temperature slightly below 20°C. The resolution at $\sigma=1.8\pm0.2$ ADC chan. is worse than that of the 2A, which is expected due to the characteristics of the ASICs. The resolution was determined by a Gaussian fit.

one SKIROC 2A can be seen in Fig. 7.9.

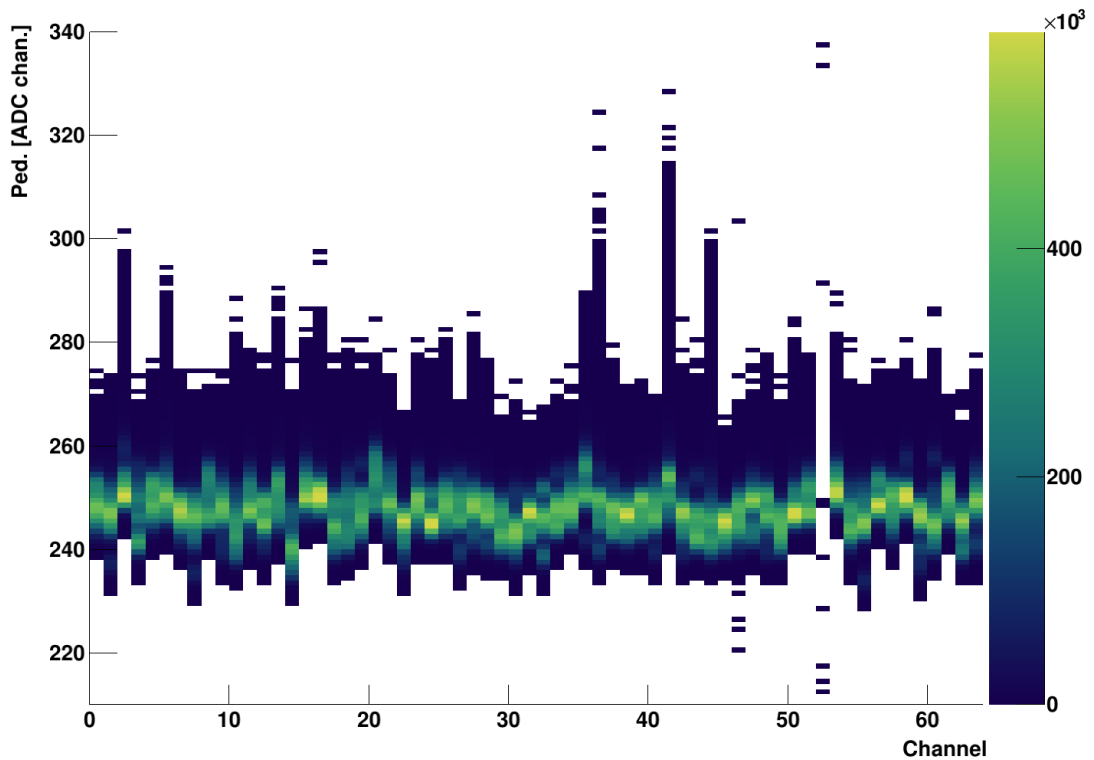


Figure 7.9.: Pedestals of a SKIROC 2A. The pedestals only differ by small fluctuations, no general trend is visible. Channel 52 was connected to an external pulser and triggered the setup, therefore no pedestal is visible for this channel.

There are only small fluctuations in the means of the pedestals, and the width is almost constant

for all of them. Since channel 52 was connected to the external pulser, no pedestal is visible for this channel. Therefore the power supply must be sufficient over the whole ASIC, since no drop in voltage can be observed. The small fluctuations still observed are due to uncertainties in the ASIC production (small differences in the feedback resistors). Any calibration procedure that aims for high resolution results has to do a channel by channel calibration, therefore the remaining difference in the pedestals is of no importance since it will be eliminated by the calibration.

7.4.3. Cross-talk

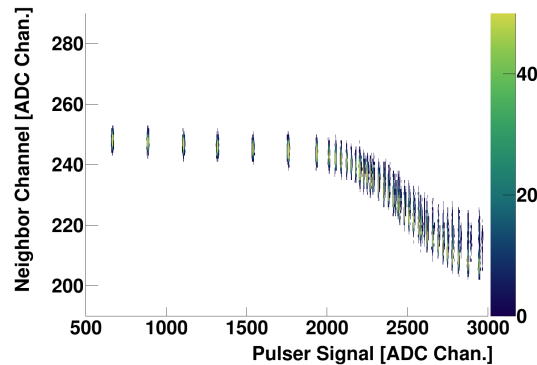


Figure 7.10.: Measurement of cross-talk in a SKIROC ASIC for the high gain readout chain. The pedestal of the neighboring channel is plotted against the measured pulser signal. For most of the range, the signals show no correlation. When very high signals (with respect to the dynamic range of the current setting) are induced, the pedestal drops slightly.

Cross-talk, meaning that a very large charge deposited in one readout channel will change the signal in other channels can also be checked. For this, pulser signals of varying height were induced in one channel and the signal in the neighboring readout channel was checked. The results are displayed in Fig. 7.10. For most of the energy range there is no dependence between pulser and pedestal level. For signals that are at the upper edge of the range of the high gain branch of the readout, there is a drop in the pedestal of the neighbor channel. This is due to the heightened power consumption of the high gain shaper when dealing with such signals. Due to this increased power consumption the neighboring channel experiences a small drop in the supply voltage, leading to a drop in the pedestals. The overall effect is small and can be easily prevented by setting the amplification according to the expected signal heights. It only sets on in the high energy regime, where the SKIROC, by design, changes to a non-linear amplification, to increase its dynamic range [Cal11]. Therefore this will not be a significant influence in NDP measurements with the SKIROC ASICs.

7.4.4. Temperature dependent effects

Fluctuations in temperature of the electronics and (although unlikely) the detectors can lead to changes in gain and resolution of the system. The GEAR-boards therefore continuously

monitor temperature of all ASICs, using the TMP102AIDRLT IC¹ temperature sensors, which are positioned directly on the PCB under each SKIROC. To quantify the effect of changes in temperature on the data acquisition, the ASICs were heated up to 70 °C. An α -source was measured with a PIN-diode connected to the SKIROC. The whole setup was positioned within a vacuum chamber, and then cooled down, thereby providing a change in temperature of the system.

Changes in three parameters have been evaluated: the gain of the channel connected to the diode, the width of the peak from the α -source and the ENC of a channel not connected to any readout. The first parameter was extracted using the mean position of the signal from the α -source. The peak position was normalized with its value at the lowest temperature, and the result plotted against the temperature of the SKIROC as seen in Fig. 7.11.

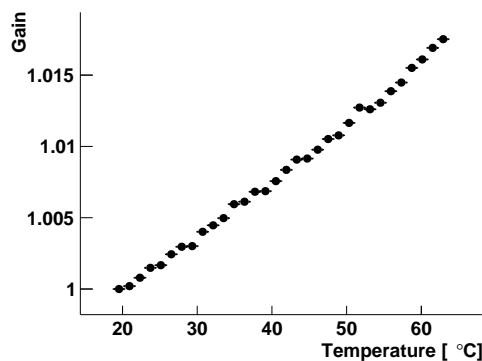


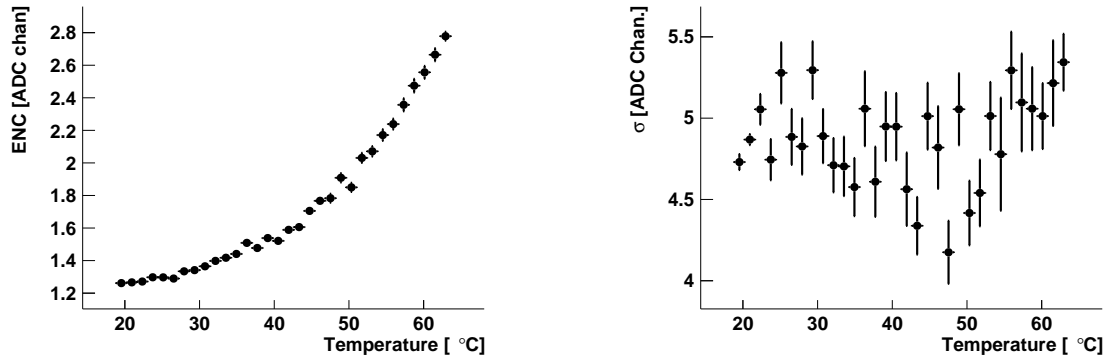
Figure 7.11.: Gain as a function of SKIROC2A temperature for one SCA. Data was taken with an α -source measured with a PIN-diode detector. The detector was thermally decoupled from the ASIC during the measurement. Data was normalized to the gain at 20 °C. The dependence between gain and temperature is largely linear.

Deviations from the linear dependence between gain and temperature, which can be seen in Fig. 7.11 are most likely due to statistical fluctuations. This has been cross checked with different SCAs. All showed the same overall behavior, but the position of the fluctuations change for each SCA, thereby excluding uncertainties of the temperature measurement as a cause. Data from all SCAs are shown in Fig. C.2. Changes in the supply voltage can be excluded as well as other environmental effects, since those would have to show up in each SCA of the ASIC at the same time (which means in the same temperature bin). The temperature is permanently monitored for every SKIROC used, and the temperature data is written to the data stream with each event. Therefore the energy information in the system will always be reconstructible, and no temperature stabilization is needed to control the gain.

Besides gain also the energy resolution of the system could change with temperature. This effect should be visible in two measurements: in the ENC of the system, and in the energy resolution achievable for mono-energetic particles. The ENC of a channel not connected to the detector was determined for different temperatures, Fig. 7.12 (a). A clear correlation between ENC and temperature is visible. When monitoring the energy resolution for 5 MeV α -particles instead (Fig. 7.12 (b)), the situation changes. Since the actual achievable resolution is significantly worse

¹ produced by TEXAS Instruments

than the ENC due to detector dead layers and thermal noise of the detector, the change in ENC does not influence the energy resolution.



(a) ENC as a function of temperature.

(b) Peak width of an α -source as a function of temperature.

Figure 7.12.: Temperature dependent resolutions. Even for large temperature changes the change in resolution is low when compared to other factors. The overall energy resolution for 5 MeV α -particles is dominated by thermal noise of the detector and by energy straggling in the detector dead-layer.

The overall effect of the temperature on the gain can be described with a simple linear dependency. The change in resolution is small when compared with other effects, even for ASIC temperatures above 60 °C. Therefore simple monitoring of the temperature of the SKIROC ASICs is sufficient for any experiment, and no temperature stabilization is needed. Due to the low energy consumption of the ASICs, radiative cooling is sufficient to stabilize temperature of the ASICs.

7.4.5. Timestamp

For a multi detector setup as is planned for the MINIBALL and the N4DP upgrades data has to be timestamped. For this purpose the GEAR firmware uses 64 bit, 5 ns timestamps. The length of the timestamps ensures the use of one continuous time, with no need to handle rollovers or buffer overflows in the timestamps. The common TRB reset is used for resetting timestamps. Furthermore, board-to-board and even inter-system synchronization is implemented via an external signal. This external signal is registered by the GEAR firmware, timestamped and the data added to the overall data stream of each event (see Fig. 7.4).

To ensure timestamping is handled properly, two tests have been performed. One was to reconstruct the time difference between two well known events from the data. This has been done by feeding a pulser with known frequency into the system (model BNC DB-2 from Berkeley Nucleonics¹). The time difference between two subsequent events was plotted in Fig. 7.13. The width of the measured distribution is RMS=1.64 μ s which is well within the timing precision achievable with the used pulser.

¹ https://www.berkeley-nucleonics.com/sites/default/files/products/datasheets/db-2_datasheet.pdf

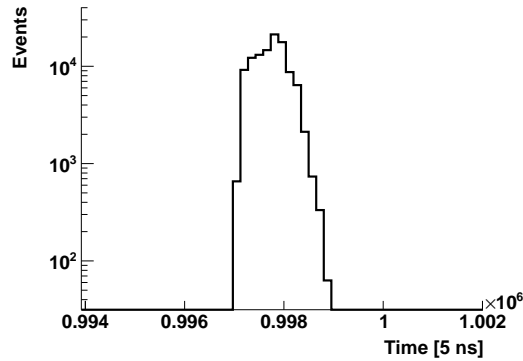


Figure 7.13.: Time difference between two pulser signals as measured with the GEAR internal timestamp. The determined frequency, at 200.46 Hz, agrees with the pulser frequency as measured with an oscilloscope (also 200 Hz). The width of the time distribution is $\text{RMS}=1.64 \mu\text{s}$ and is limited by the used pulser (model BNC DB-2 by Berkeley Nucleonics).

In a more realistic test scenario, a α -source has been measured with a silicon detector. The measured time difference between two events will follow an exponential distribution. The measurement result is displayed in Fig. 7.14. The step at ca. 7 ms ($1.4 \cdot 10^6 \times [5 \text{ ns}]$) is due to the dead time of the ASIC. Events that are chronologically separated by more than 7 ms are guaranteed to be registered. For smaller time differences there is a chance that the ASIC is currently being read out, thereby leading to an unregistered event, which corresponds to a small drop in efficiency.

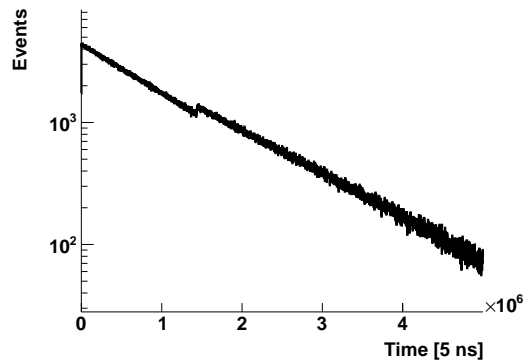


Figure 7.14.: Time difference between two subsequent events originating from an α -source. The expected exponential distribution is well visible. The step at 7 ms is due to the read out time of the ASIC (details in the text).

8. Detector for 4D NDP

Laterally and time resolved NDP (4D NDP), requires detectors with good position resolution and excellent energy resolution. Furthermore, the detectors are required to be insensitive to β - and γ -radiation while having a high efficiency for ion detection. This chapter starts by detailing the requirements for a detector suitable for the upgrade of the N4DP instrument. It will then discuss the limitations of current, commercially available detectors. Measurements with commercially available strip detectors are shown, to illustrate limitations as well as the performance of standard detectors. All results have been acquired using the electronics detailed in Chapter 7. The chapter concludes by presenting prototype detectors, which are able to fulfill all requirements for the upgrade of the N4DP instrument.

8.1. Detector performance needed for N4DP

Energy resolutions achievable with surface barrier detectors using dedicated single channel electronics at the N4DP instrument, are FWHM=21 keV for a triple α -source. The SKIROC 2A ASIC has a maximum resolution of $\sigma=6$ keV. Therefore energy straggling (σ) in the detector should be around 7 keV for α -particles to reach a comparable result with double-sided silicon microstrip detectors (DSSDs). Using Geant4 simulations the typical dead-layer structure of a DSSD has been simulated. For this, a silicon bulk material was simulated, with a dead-layer due to the implantation process on top of it. It was followed by a 40 nm thick isolation layer, and a 350 nm thick aluminum layer was included as the topmost layer. While isolation layer thickness and aluminum thickness are given by required electrical characteristics, the implant layer thickness can be varied. A typical NDP reaction, the neutron capture of ^{10}B was simulated. The produced α - and ^7Li -particles impinged on the simulated detector, and the energy measured within the detector was determined. The thickness of the implant related dead-layer was then varied, to determine the influence of the crucial implantation process on the quality of the resulting detector. The results are presented in Fig. 8.1. As these simulations show, this can be achieved with an implant dead-layer with a thickness between 100 and 300 nm.

The detector thickness is given by several physical constraints. On the one hand, thinning detectors helps to drastically reduce background (see Fig. 4.3). The NDP reactions impose a limit on the thickness at around $42\ \mu\text{m}$, which is the thickness needed to fully stop the highest energy particles produced in NDP. But also mechanical stability has to be considered. Very thin silicon sheets are prone to splintering and breaking, even when handled with great care. DSSDs production includes cutting the detectors out of a larger silicon sheet, and these detectors also need to be bonded onto the PCB to be read out. Both procedures induce mechanical stress onto the detector and therefore limit the minimum thickness achievable for the detectors. After tests performed by CiS¹, the research institute producing the detectors, it was decided to use $70\ \mu\text{m}$

¹ CiS Forschungsinstitut für Mikrosensorik GmbH, Erfurt, Germany

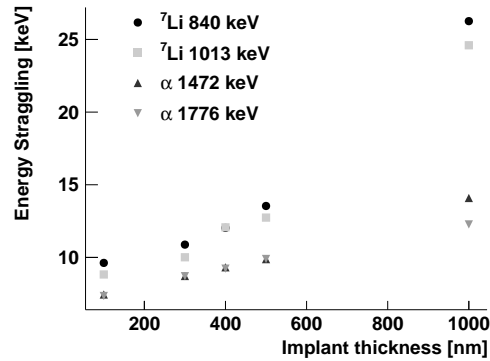


Figure 8.1.: Geant4 simulation of detector responses to the ${}^{10}\text{B}(n,\alpha)$ reaction. Energy straggling in the detector dead-layer is shown against the thickness of the implant related dead-layer. A 40 nm thick isolation layer, and a 350 nm thick aluminum layer were simulated on top of the implant layer. Energy straggling, especially for the ${}^7\text{Li}$ -particles is drastically reduced by thinner implantation layers.

thick detectors for the N4DP upgrade.

In the simplest case, the N4DP upgrade will employ a *camera obscura* type measurement. With etching techniques, hole sizes between 10 and 100 μm are possible for the aperture. Since magnifications between 1 and 10 are possible with the chamber geometry, the detectors position resolution should be $\approx 100 \mu\text{m}$ as to not limit the measurement resolution. Assuming a circular beam-spot with a diameter of 4 mm and a magnification of 10, the detectors need to cover an area of at most 4 cm diameter. Due to double use concept underlying the detector development, a trapezoidal detector shape was chosen. Fig. 8.2 shows the circuit board on which the detector will be mounted, with the area reserved for the detector marked in gray. The chosen detector layout has the advantage of allowing the construction of several shapes in two and three dimensions, including a pyramid with a hexagonal base. This three dimensional construct allows for an almost complete 4π coverage of the sample (thereby fulfilling the requirements for the TREX upgrade at MINIBALL [Ber20]).

At the N4DP instrument, this detector shape will enable several different configurations. In the simplest case, one detector will be used together with an aperture. In this setting a maximum of 158 readout channels will be read out (not taking into account channels not connected to the detectors). The most complex possible configuration will be a coincidence measurement using two detector pyramids with a hexagonal base, one in front of the sample and one behind it. This will provide 4π coverage, thereby enabling measurements with highest statistics (which will enable an excellent time resolution). In this configuration, the data acquisition would have to handle 12 times more channels (1896) than in the simplest configuration.

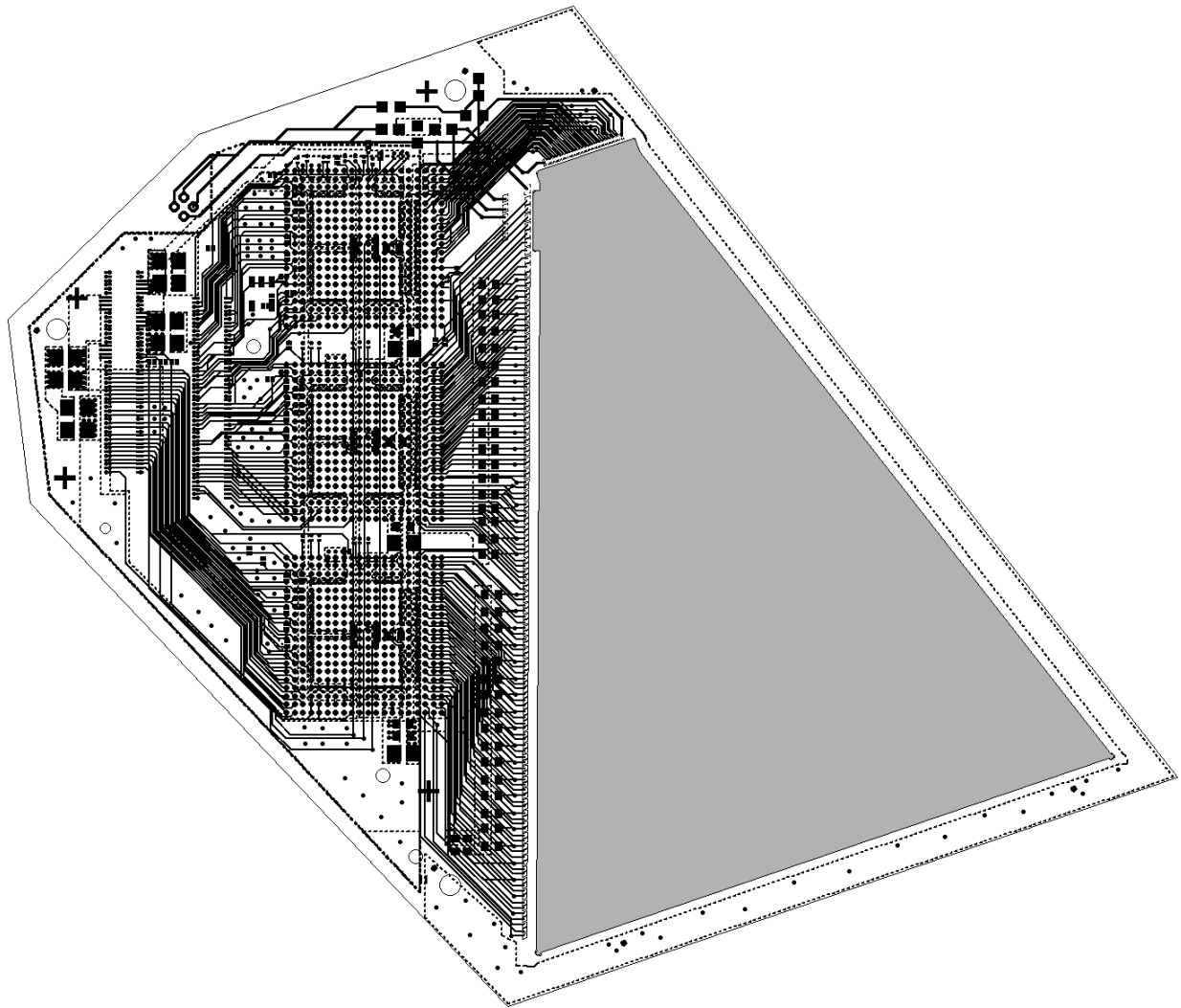


Figure 8.2.: Layout of the printed circuit board (pcb) on which the detector will be mounted. The area filled in gray shows the location of the detector. This area is milled out in the PCB design. The detector has a height of 72.6 mm, a maximum width of 61.5 mm and a minimum width of 11 mm.

8.2. Commercially available silicon strip detectors

Due to the excellent characteristics of silicon based detectors in α -spectroscopy and similar fields, like NDP, the upgrade was based on the concept of silicon strip detectors. Currently available DSSDs are often designed for Vertex reconstruction in high energy physics or with similar applications in mind [Ton97, Lia19, Res19]. Due to the high energies of the particles involved, dead-layer thicknesses and inhomogeneities of the dead-layers are not relevant for these detectors.

But in NDP, these play an important role. Even small fluctuations in dead-layer thicknesses can lead to the appearance of so called satellite peaks. The effect can be described with a simple model. For mono-energetic α -particles with energies of a few MeV, a detector dead-layer of ≈ 100 nm will shift the detected energy by a few keV. If a second dead-layer exists, which covers a different part of the detector and has a different thickness, it will shift particles impinging in these areas by a different energy. Therefore a second peak, at a different energy will appear in the spectrum.

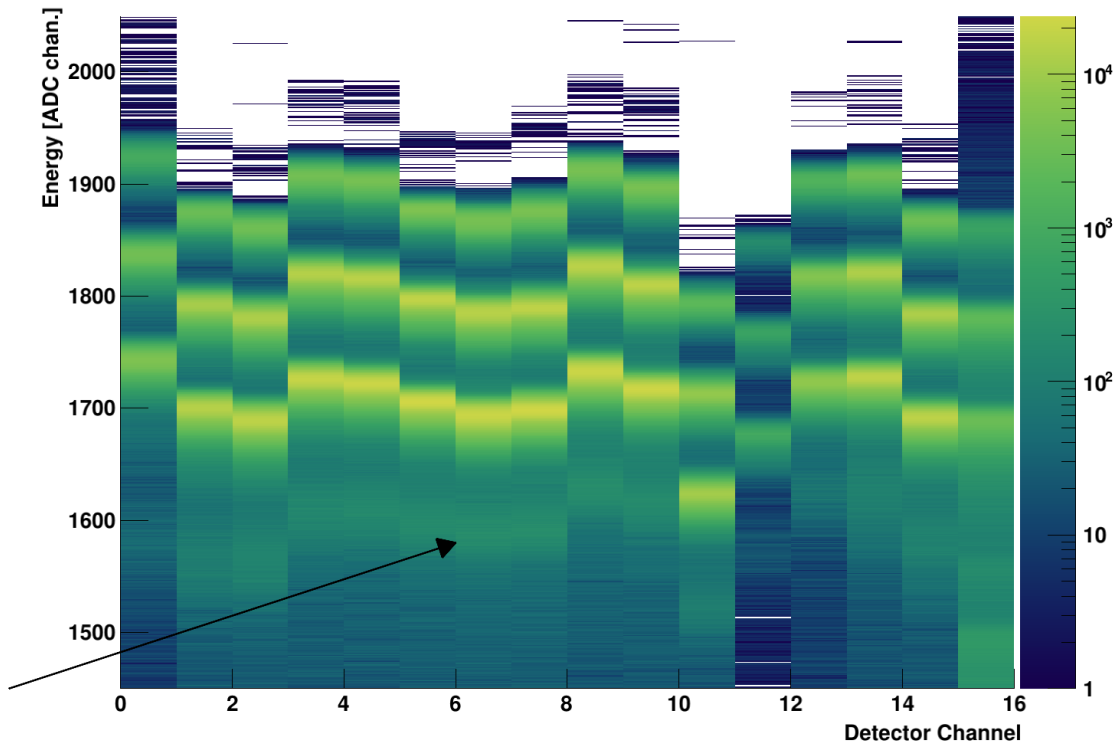


Figure 8.3.: Measurement of a triple α -source using a commercially available strip detector. The measurement has been performed using the SKIROC 2A ASIC and the GEAR front-end board. The three energies of the source are well visible. Satellite peaks, due to dead-layer inhomogeneities in the detector, are observed. One is highlighted with an arrow. If used in an NDP measurement such artifacts could lead to misinterpretations of the sample's depth profile.

This effect is illustrated in Fig. 8.3, which shows a measurement of a triple- α -source (curium, ameritium and plutonium α -sources) performed with a commercially available detector.

Further testing using a commercially available DSSD was performed at the Munich tandem accelerator facility MLL. A beam of ^{58}Ni was accelerated to 110 MeV. ^{58}Ni deposited on a carbon foil was used as a target. A DSSD¹, with 16 strips on the frontside and 16 strips on the back was used as a detector and read out using the custom made electronics, firmware and software described in Chapter 7. The data acquired with the front side of the detector are shown in Fig. 8.4. The expected energy, calculated assuming elastic scattering, as a function of the angle relative to the beam is also plotted for several particles [Ber20]. Data and expectations are well in agreement, showing that the developed readout system is ready for use in realistic conditions. Currently the deployment of the full setup at the N4DP instrument is only hindered by the need for very homogeneous, ultra-thin dead-layers. Detectors fulfilling these specific requirements are under development. Tests with prototypes of these detectors are presented in Section 8.3.

¹ W1(DS)-100, Type 9G/2M Silicon detector from MicronSemiconductor

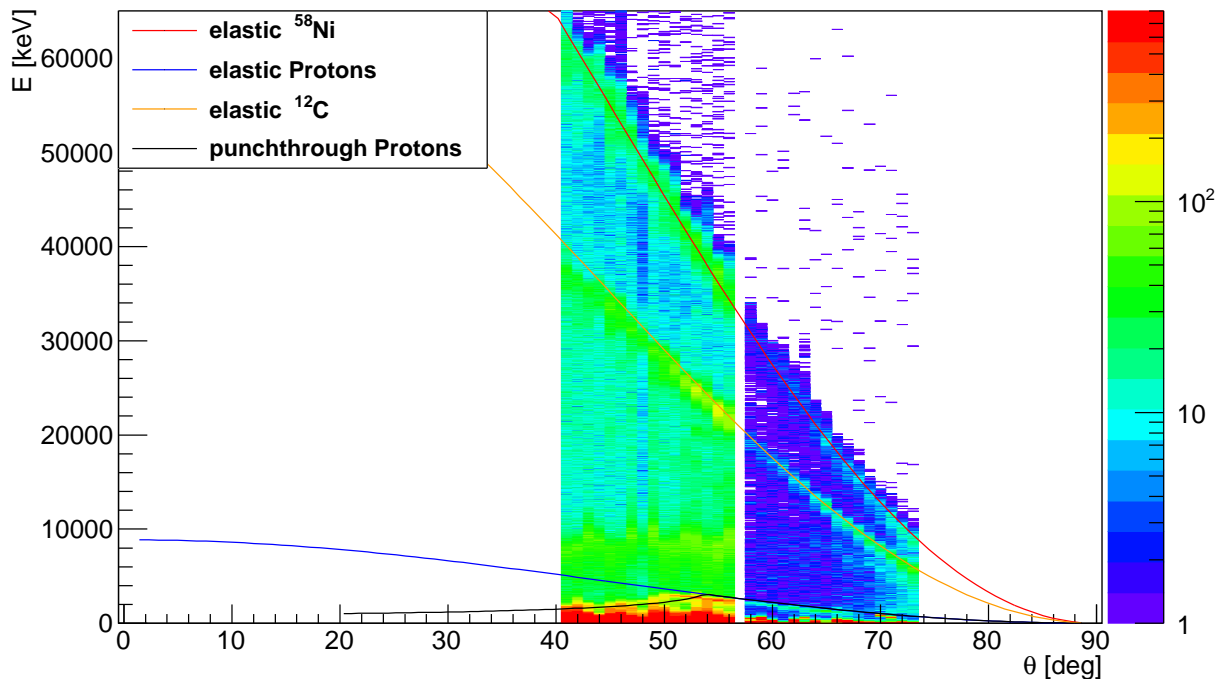


Figure 8.4.: Measurement of elastic scattering. The ^{58}Ni beam impinges on a ^{58}Ni and carbon target with an energy of 110 MeV. Shown is the energy measured as a function of the angle relative to the beam. Data was taken with the readout electronics described in Chapter 7. A 16x16 strip DSSD was used as detector. The expected energy distributions for elastic scattering with different particles are plotted. Data and calculations are in good agreement. Data were taken at the MLL and adapted from [Ber20].

8.3. Prototypes

A critical part of the detector design is the required, very thin implant layer. Therefore CiS¹ has produced several prototypes, which consist of unsegmented PIN-diode type detectors. These prototypes were used in NDP measurements to verify functionality and determine the dead-layer thickness.

For this purpose, a full calibration as detailed in Section 4.2, was performed. Data was taken using the electronics of the N4DP instrument (Setup I, see Section 3.5). In this calibration process, the dead-layer thickness is an input parameter for the energy loss calculations. Since the actual thickness of the dead-layer was unknown, calculations were performed for several thicknesses, with a step size of 5 nm. The shape of the calibration curve was then compared to the one determined for the silicon surface barrier detectors. In this way, the implantation dead-layer for the most promising production batch was determined to be 150 ± 10 nm. The uncertainty was determined by varying the assumed dead-layer thickness, and comparison of the resulting distributions. The calibration curve for this value is shown in Fig. 8.5.

The implant depth determined for the prototype detector fulfils the requirements of the N4DP

¹ CiS Forschungsinstitut für Mikrosensorik GmbH, Erfurt, Germany

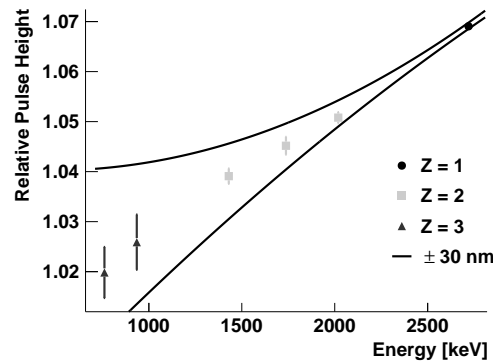


Figure 8.5.: Relative pulse height as a function of particle energy for a prototype detector. The detectors dead-layer was determined to be 150 nm. The two black lines indicate the position of the data points if the thickness would have been over-/underestimated by 30 nm.

upgrade. Together with thin isolation layers and optimized aluminium strip structures, the planned strip detectors will allow for highest resolution measurements.

Using the electronics developed for the readout of strip detectors at the N4DP instrument, a triple α -source was also measured using a CiS prototype PIN-diode. Due to the size and thickness of the prototype, it is comparable to a single strip of the final DSSD detector. The measurement using the GEAR board and the SKIROC 2A ASIC is shown in Fig. 8.6. The achieved resolution of 24 keV FWHM is similar to the 21 keV reached for the same source with silicon surface-barrier detectors (using Setup I).

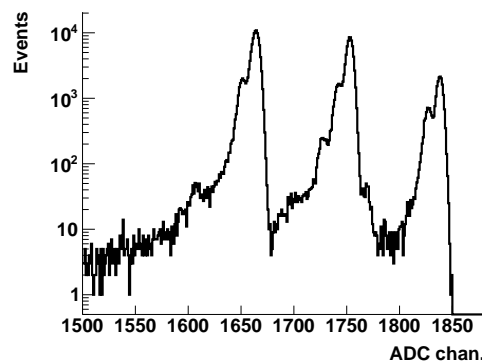


Figure 8.6.: Measurement of a triple α -source using a CiS prototype detector and the SKIROC 2A ASIC. Decays into different states are well separated. The resolution has been determined to be FWHM=24 keV for a single peak.

The built electronics, combined with the detector prototypes have performed very similar to the existing electronics and detectors used in the classical NDP configuration. Due to the planned detectors being thinner than the currently used surface barrier detectors, a better signal-to-noise ratio can be expected. The planned setup will deliver high lateral position resolution, while simultaneously providing a depth resolution very similar to the current configuration.

9. Summary and Outlook

In the scope of this thesis a new Neutron Depth Profiling (NDP) instrument, the N4DP instrument was designed, built, and set up at the Forschungsneutronenquelle München (FRM II). Several successful experimental campaigns have been performed with the instrument. These include research in the fields of electro-chemistry (batteries), metallurgy (heat resistant alloys) and neutron guides (borofloat glasses). To enable position resolved measurements, hardware, firmware and software based on the SKIROC readout-chips have been developed, which, together with novel detectors will allow performing time and position resolved NDP at the N4DP instrument.

At a neutron flux density of $5 \times 10^9 \frac{n}{\text{cm}^2 \text{s}}$ (thermal equivalent) the N4DP instrument has the highest neutron flux density of any current NDP setup (two times higher than the neutron flux currently available at one of the leading NDP facilities at the NIST research reactor [Dow93]). This flux is provided by the beamline of the PGAA facility at the FRM II. The good shielding and corresponding low background available at the PGAA experimental site is a further advantage. The design of the N4DP vacuum chamber allows for an optimal use of the available space while simultaneously optimizing background count rates even further. A modular sample stage, controlled by two stepping motors is fully integrated into the instrument.

The N4DP instrument achieves depth resolution below 10 nm, while simultaneously having an excellent signal-to-background ratio. These parameters are realized through the use of silicon-surface-barrier detectors, which are read out by state of the art charge sensitive preamplifiers combined with low noise shaping amplifiers. The chamber and detectors are optimized to a point where even idealized samples with low neutron scattering and absorption cross sections (e.g. thin silicon wafers) introduce more background than all other sources combined. For commercially available silicon-surface-barrier detectors the current setup presents the optimal configuration.

The excellent depth resolution of the N4DP instrument rests not only on highest resolution detectors and electronics, but also on a high precision calibration method. The influence of the Pulse-Height-Defect (PHD) on the calibration was determined. The introduction of a non-linear term into the N4DP instruments calibration function allows for the compensation of the PHD over a wide range of energies and ion species, thereby allowing the use of a single calibration function for almost all NDP applications. The viability of this calibration was verified using a specially designed multi-layered sample. The results show a good agreement between data and theoretical prediction with a mean deviation of only 1.3%.

Already during the design and commissioning phase numerous experiments have been performed using the N4DP instrument. The investigation of boron containing float glasses, which are used for neutron guide production, revealed differences in boron content for the two glass surfaces [Wer18]. Several battery systems were analysed. Especially noteworthy are the investigations of silicon graphite anodes [Tru18, Wet18b, Wet19] in which the growth of the solid-electrolyte interface (SEI) could be linked to a morphology change in the silicon particles. A specialized battery casing allowed to perform, for the first time, *operando* measurements of lithium ion batteries with

liquid electrolytes. These batteries have been shown to be fully functioning and comparable to commercially available lithium ion batteries. This enables, for example, direct investigation of effects currently limiting the charge speed of lithium ion batteries, like lithium plating [Lin20].

Using modern detectors and electronics, the N4DP instrument will be extended beyond its current limitations, by introducing position and time resolved 4D NDP. To achieve this goal, readout electronics have been developed in the scope of this thesis. Together with the high performance firmware and software modules, position resolved measurements using the SKIROC readout chips are enabled by these developments. Important properties of the N4DP setup with monolithic silicon surface barrier detectors, and the properties expected for the segmented double sided silicon microstrip detectors are listed in Table 9.1.

Detector type:	Surface barrier	DSSSD
Channels	1-16	1-1896
Position resolution	N/A	$\approx 100 \mu\text{m}$
Dead-layer	80 nm Si	150 nm Si
FWHM (α at 5 MeV)	21 keV	24 keV
Readout mode	continuous	bunched
Δt_{min} (between two events)	$>10 \mu\text{s}$	$\approx 70 \text{ ns}$

Table 9.1.: Summary of important properties of the current N4DP setup (with surface barrier detectors) and of the upgrade (with DSSSDs).

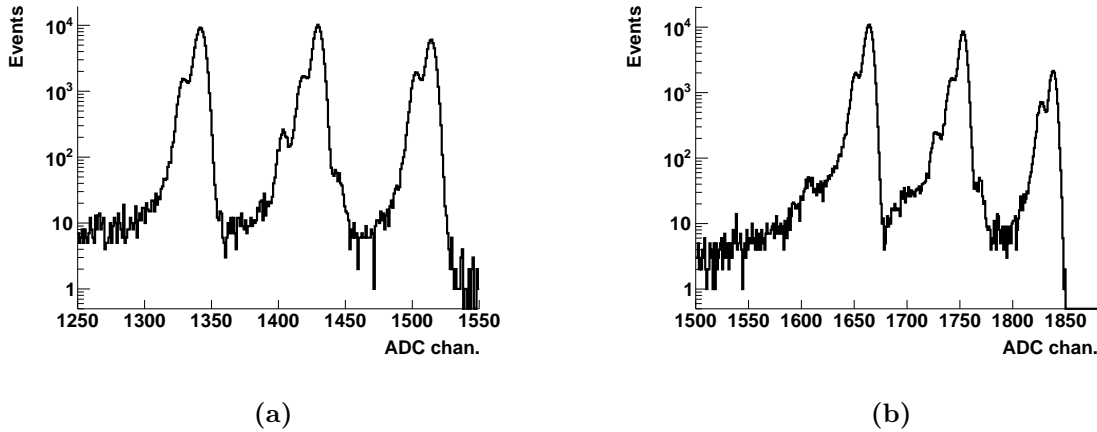


Figure 9.1.: Measurement of a triple- α source (plutonium, ameritium and curium). Panel (a) shows the measurement performed with a silicon surface barrier detector and large, single channel electronics. The achieved resolution is 21 keV FWHM. Panel (b) shows the α -spectrum measured with a prototype detector using the SKIROC 2A chip and the readout electronics developed in the scope of this thesis. The resolution is 24 keV FWHM. The resolution of both systems is very similar. The resolution achieved with the prototype system fulfils the requirements for the N4DP instruments upgrade. Measurements were taken with two slightly different α -sources.

The 4D implementation chosen for the N4DP instrument is designed not to compromise the achievable energy resolution. The complex and high performing system developed achieves this goal. Fig. 9.1 shows two measurements of a triple- α source. The one in panel (a) has been

measured with the classical NDP setup at the N4DP instrument. The measurement shown in panel **(b)** was obtained using the newly developed electronics and prototype detectors. For this configuration, a full width at half maximum of 24 keV was achieved. This is similar to the 21 keV which have been achieved with the current N4DP setup.

Further developments at the instrument are planned as well. The good performance of the new detectors and electronics will be further enhanced by a new, high flux, low background neutron beam guide. This guide will push up the available neutron flux density at the sample position by more than one order of magnitude. This high flux density will enable *operando* measurements with finest time granularity. Inclusion of the current software front-end into the overall control software used at the MLZ will provide a standardized user interface, thereby fully integrating the instrument into the MLZ.

A. List of Publications

1. Werner, L.; Trunk, M.; Gernhäuser, R.; Gilles, R.; Märkisch, B. and Revay, Z. *The new neutron depth profiling instrument N₄DP at the Heinz Maier-Leibnitz Zentrum*. Nuclear Instruments and Methods in Physics Research Section A: Accelerators, Spectrometers, Detectors and Associated Equipment, 2018. 911, 30 – 36. ISSN 0168-9002. doi: 10.1016/j.nima.2018.09.113
2. Trunk, M.; Wetjen, M.; Werner, L.; Gernhäuser, R.; Märkisch, B.; Revay, Z.; Gasteiger, H. and Gilles, R. *Materials science applications of Neutron Depth Profiling at the PGAA facility of Heinz Maier-Leibnitz Zentrum*. Materials Characterization, 2018. 146, 127 – 134. ISSN 1044-5803. doi: 10.1016/j.matchar.2018.09.030
3. Wetjen, M.; Trunk, M.; Werner, L.; Gernhäuser, R.; Märkisch, B.; Revay, Z.; Gilles, R. and Gasteiger, H.A. *Quantifying the Distribution of Electrolyte Decomposition Products in Silicon-Graphite Electrodes by Neutron Depth Profiling*. Journal of The Electrochemical Society, 2018. 165, A2340 – A2348. ISSN 10. doi: 10.1149/2.1341810jes
4. Wetjen, Morten and Trunk, Markus and Werner, Lukas and Gasteiger, Hubert A. and Gernhäuser, Roman and Gilles, Ralph and Märkisch, Bastian and Révay, Zsolt. *Monitoring the Lithium Concentration across the Thickness of Silicon-Graphite Electrodes during the First (De-)Lithiation*. Journal of The Electrochemical Society, 2019. 166(8), A1408–A1411. doi: 10.1149/2.0581908jes
5. Linsenmann, F.; Trunk, M.; Rapp, P.; Werner, L.; Gernhäuser, R.; Gilles, R.; Märkisch, B.; Revay, Z. and Gasteiger, H. *A Liquid Electrolyte-Based Lithium-Ion Battery Cell Design for Operando Neutron Depth Profiling*. Journal of the Electrochemical Society, 2020
6. Frankenberger, M.; Trunk, M.; Seidlmayer, S.; Dinter, A.; Dittloff, J.; Werner, L.; Gernhäuser, R.; Revay, Z.; Märkisch, B.; Gilles, R. et al. *SEI Growth Impacts of Lamination, Formation and Cycling in Lithium Ion Batteries*. Batteries, 2020. 6(2), 21
7. Berner, C.; Werner, L. and Gernhäuser, R. *HI-TREX - A highly integrated transfer setup at REX-(HIE)ISOLDE*. Nuclear Instruments and Methods in Physics Research Section A: Accelerators, Spectrometers, Detectors and Associated Equipment, 2020. submitted

B. Slowcontrol Registers

The following tables present a complete list of all slow control registers available. The first column denotes the data word (in hexadecimal), the second the bit(s) (in decimal), and the third column describes the effect/purpose.

Adress	Bit	Meaning
		BOARD
0xe010	0	Switch on ASIC LDOs
0xe001	N/A	Reset all SKIROCS, read or write access.
0xe002	N/A	Load Slow Control all ASICS
0xe003	N/A	Take Data, all ASICS Not Available
0xe004	2-0	Use PowerPulsing DAQ (001 = powerpulsing, 100= no powerpulsing) Not Available
0xe0ff	N/A	Activate Test Out! (Depending on bits 15 to 0 of reg 0xe0ff) Not Available
		TOP ADDON
		Klemme1
0xe012	0	Pin1
	1	Pin2
	2	Pin3
	3	Pin4
	4	Pin5
	5	Pin6
	6	Pin7
	7	Pin8
	8	Pin9
	9	Pin10
	10	Pin11
	11	Pin12
		Klemme2
0xe013	0	Pin1
	1	Pin2
	2	Pin3
	3	Pin4
	4	Pin5
	5	Pin6
	6	Pin7
	7	Pin8
	8	Pin9
	9	Pin10
	10	Pin11
	11	Pin12

		GPIO 40Pin (LAYOUT wie RasPI!, d.h 1=topLinks 2=topRechts)
0xe014	0	Pin3
	1	Pin5
	2	Pin7
	3	Pin11
	4	Pin13
	5	Pin15
	6	Pin19
	7	Pin21
	8	Pin23
	9	Pin27
	10	Pin29
	11	Pin31
	12	Pin33
	13	Pin35
	14	Pin37
	15	Pin8
	16	Pin10
	17	Pin12
	18	Pin16
	19	Pin18
	20	Pin22
	21	Pin24
	22	Pin26
	23	Pin28
	24	Pin32
	25	Pin36
	26	Pin38
	27	Pin40
0xe015	0	Force readout if one asic is full
	1	Activate raz chn (do not use)
	2	Deactivate sequential readout if force readout is active
	3	Reserved
	4	If 1: 2a1 can not trigger readout of other asics
	5	If 1: 2a2 can not trigger readout of other asics
	6	If 1: cms can not trigger readout of other asics

Adress	Bit	Meaning
0xc0xx		SKIROC 2A1
0xc000	--	Load 2A1 SLCTR
0xc001		MISC. commands
	0	Backup SCA selection. 15 depth SCA =0, 1 = backup SCA
	1	Track and Hold /SCA Bias (weak bias = 0)
	2	Choose gain value if auto gain is disabled (HG =0)
	3	Allows to bypass latch used during auto gain select (0= no bypass)
	4	Select ADC_TEST input as analogue data to convert (0 =off)
	5	TDC ramp slope (1= 200ns 0 = 5 us)
	6	Select external adc ramp commands (0 = use ASIC commands)
	7	ADC ramp slope (0= 12 bits 1= 10 bits)
	8	use external TDC commands (0 = use ASIC commands)
	9	select analogue signal to digitize when Flag_TDC_external selected
	10	select external TDC ramp commands (0 = use ASIC commands)
	11	select only external trigger for sampling (0= TrigInt or Trigext)
	12	End_readout_1 enabled (0 = End_readout_2 enabled)
	13	select start_ReadOut1 (1) or Start_Readout2(0)
0xc002		Set THRESHOLDS
	1-0	fast shaper time constant commands
	9-2	Delay for the "trigger" signals (from LSB to MSB)
	19-10	10-Bit DAC (From LSB (highest) to MSB) for Trigger discriminator threshold
	29-20	10-Bit DAC (From LSB to MSB) for gain select discriminator threshold
0xc003	7-0	CHIP ID
0xc004		Enable word (On normally 1), used for switching on parts
	0	preamps on
	1	Enable slow shaper G1
	2	Enable slow shaper G10
	3	Enable fast shaper
	4	enable SCA
	5	enable backup SCA
	6	enable Hi-Z output OTA
	7	enable probe OTA
	8	enable 4-bit DAC Adjustment
	9	enable Trigger Discriminator
	10	Trigger delay enabled
	11	Auto gain selected

	12	Gain Select Discriminator enabled
	13	enable ADC discriminator
	14	Bandgap OTA disabled
	15	10-Bit dual DAC enabled
	16	enable TDC ramp
	17	TDC ramp switch inject charge compensation enabled (default off)
	18	ADC ramp enabled
	19	ADC ramp switch inject charge compensation enabled (default off)
	20	TDC on, 0 TDC off, TDC should be switched OFF due to noise problems
	21	enable weak Open collector Trigger Out signal (1= Trig out enabled)
	22	ChipSat enabled
	23	Transmit_ON2 enabled
	24	Transmit_ON1 enabled
	25	Dout2 enabled
	26	Dout1 enabled
0xc005		Trigger Mask from CH 32 to CH 63
	31-0	BIT 31 = Ch 32, BIT 0 = CH 63
0xc006		Trigger Mask from CH 0 to CH 31
	31-0	BIT 31 = Ch 0, BIT 0 = CH 31
0xc007		4-BIT DAC adjust
	31-0	Bit 31-28 = CH 63; Bit 3-0 = CH 56
0xc008		4-BIT DAC adjust
	31-0	Bit 31-28 = CH 55; Bit 3-0 = CH 48
0xc009		4-BIT DAC adjust
	31-0	Bit 31-28 = CH 47; Bit 3-0 = CH 40
0xc00a		4-BIT DAC adjust
	31-0	Bit 31-28 = CH 39; Bit 3-0 = CH 32
0xc00b		4-BIT DAC adjust
	31-0	Bit 31-28 = CH 31; Bit 3-0 = CH 24
0xc00c		4-BIT DAC adjust
	31-0	Bit 31-28 = CH 23; Bit 3-0 = CH 16
0xc00d		4-BIT DAC adjust
	31-0	Bit 31-28 = CH 15; Bit 3-0 = CH 8
0xc00e		4-BIT DAC adjust
	31-0	Bit 31-28 = CH 7; Bit 3-0 = CH 0
0xc00f		Settings for Preamps
	2-0	preamp compensation capacitance commands

	6-3	preamp feedback capacitance commands
0xc010		select high leakage current (=1)
	31-0	Bit 31 = Ch31 Bit 0 = Ch0
0xc011		select high leakage current(=1)
	31-0	Bit 31 = Ch63 Bit 0 = Ch32
0xc012		Disable Ctest
	31-0	Bit 31 = Ch31 Bit 0 = Ch0
0xc013		Disable Ctest
	31-0	Bit 31 = Ch63 Bit 0 = Ch32
0xc014		disable charge preamp
	31-0	Bit 31 = Ch31 Bit 0 = Ch0
0xc015		disable charge preamp
	31-0	Bit 31 = Ch63 Bit 0 = Ch32
0xc016		Power Pulsing control; if bit is 0 and broadcast =0: PP ON, else OFF
	0	preamp power pulsing
	1	slow shaper G1 power pulsing
	2	slow shaper G10 power pulsing
	3	fast shaper power pulsing
	4	SCA power pulsing
	5	backup SCA power pulsing mode
	6	Hi-Z output OTA power pulsing
	7	probe OTA power pulsing
	8	4-bit DAC Adjustment power pulsing
	9	Trigger Discriminator power pulsing
	10	Trigger delay power pulsing
	11	Gain select discriminator power pulsing
	12	ADC discriminator power pulsing
	13	Bandgap OTA power pulsing
	14	10-Bit dual DAC power pulsing
	15	TDC ramp power pulsing
	16	ADC ramp power pulsing
	17	LVDS recivers power pulsing
	18	Broadcast Option: if 1 PP is OFF for all, if 0: PP CAN be switched on
0xc017		Take Data , on r/w strobe
0xc018		Reset
0xc019	2-0	Processing mode (001=REDUCE untested, 010= NO REDUCE, 110=JUST_COUNTER, 100=NO_GRAY)

0xc020	0	If 1, take Data, if 0 don't
Adress	Bit	Meaning
0xc1xx		SKIROC 2A2
0xc100	--	Load 2A1 SLCTR
0xc101		MISC. commands
	0	Backup SCA selection. 15 depth SCA =0, 1 = backup SCA
	1	Track and Hold /SCA Bias (weak bias = 0)
	2	Choose gain value if auto gain is disabled (HG =0)
	3	Allows to bypass latch used during auto gain select (0= no bypass)
	4	Select ADC_TEST input as analogue data to convert (0 =off)
	5	TDC ramp slope (1= 200ns 0 = 5 us)
	6	Select external adc ramp commands (0 = use ASIC commands)
	7	ADC ramp slope (0= 12 bits 1= 10 bits)
	8	use external TDC commands (0 = use ASIC commands)
	9	select analogue signal to digitize when Flag_TDC_external selected
	10	select external TDC ramp commands (0 = use ASIC commands)
	11	select only external trigger for sampling (0= TrigInt or Trigext)
	12	End_readout_1 enabled (0 = End_readout_2 enabled)
	13	select start_ReadOut1 (1) or Start_Readout2(0)
0xc102		Set THRESHOLDS
	1-0	fast shaper time constant commands
	9-2	Delay for the "trigger" signals (from LSB to MSB)
	19-10	10-Bit DAC (From LSB (highest) to MSB) for Trigger discriminator threshold
	29-20	10-Bit DAC (From LSB to MSB) for gain select discriminator threshold
0xc103	7-0	CHIP ID
0xc104		Enable word (On normally 1), used for switching on parts
	0	preamps on
	1	Enable slow shaper G1
	2	Enable slow shaper G10
	3	Enable fast shaper
	4	enable SCA
	5	enable backup SCA
	6	enable Hi-Z output OTA
	7	enable probe OTA
	8	enable 4-bit DAC Adjustment
	9	enable Trigger Discriminator

	10	Trigger delay enabled
	11	Auto gain selected
	12	Gain Select Discriminator enabled
	13	enable ADC discriminator
	14	Bandgap OTA disabled
	15	10-Bit dual DAC enabled
	16	enable TDC ramp
	17	TDC ramp switch inject charge compensation enabled (default off)
	18	ADC ramp enabled
	19	ADC ramp switch inject charge compensation enabled (default off)
	20	TDC on, 0 TDC off, TDC should be switched OFF due to noise problems
	21	enable weak Open collector Trigger Out signal (1= Trig out enabled)
	22	ChipSat enabled
	23	Transmit_ON2 enabled
	24	Transmit_ON1 enabled
	25	Dout2 enabled
	26	Dout1 enabled
0xc105		Trigger Mask from CH 32 to CH 63
	31-0	BIT 31 = Ch 32, BIT 0 = CH 63
0xc106		Trigger Mask from CH 0 to CH 31
	31-0	BIT 31 = Ch 0, BIT 0 = CH 31
0xc107		4-BIT DAC adjust
	31-0	Bit 31-28 = CH 63; Bit 3-0 = CH 56
0xc108		4-BIT DAC adjust
	31-0	Bit 31-28 = CH 55; Bit 3-0 = CH 48
0xc109		4-BIT DAC adjust
	31-0	Bit 31-28 = CH 47; Bit 3-0 = CH 40
0xc10a		4-BIT DAC adjust
	31-0	Bit 31-28 = CH 39; Bit 3-0 = CH 32
0xc10b		4-BIT DAC adjust
	31-0	Bit 31-28 = CH 31; Bit 3-0 = CH 24
0xc10c		4-BIT DAC adjust
	31-0	Bit 31-28 = CH 23; Bit 3-0 = CH 16
0xc10d		4-BIT DAC adjust
	31-0	Bit 31-28 = CH 15; Bit 3-0 = CH 8
0xc10e		4-BIT DAC adjust
	31-0	Bit 31-28 = CH 7; Bit 3-0 = CH 0

0xc10f		Settings for Preamps
	2-0	preamp compensation capacitance commands
	6-3	preamp feedback capacitance commands
0xc110		select high leakage current (=1)
	31-0	Bit 31 = Ch31 Bit 0 = Ch0
0xc111		select high leakage current(=1)
	31-0	Bit 31 = Ch63 Bit 0 = Ch32
0xc112		Disable Ctest
	31-0	Bit 31 = Ch31 Bit 0 = Ch0
0xc113		Disable Ctest
	31-0	Bit 31 = Ch63 Bit 0 = Ch32
0xc114		disable charge preamp
	31-0	Bit 31 = Ch31 Bit 0 = Ch0
0xc115		disable charge preamp
	31-0	Bit 31 = Ch63 Bit 0 = Ch32
0xc116		Power Pulsing control; if bit is 0 and broadcast =0: PP ON, else OFF
	0	preamp power pulsing
	1	slow shaper G1 power pulsing
	2	slow shaper G10 power pulsing
	3	fast shaper power pulsing
	4	SCA power pulsing
	5	backup SCA power pulsing mode
	6	Hi-Z output OTA power pulsing
	7	probe OTA power pulsing
	8	4-bit DAC Adjustment power pulsing
	9	Trigger Discriminator power pulsing
	10	Trigger delay power pulsing
	11	Gain select discriminator power pulsing
	12	ADC discriminator power pulsing
	13	Bandgap OTA power pulsing
	14	10-Bit dual DAC power pulsing
	15	TDC ramp power pulsing
	16	ADC ramp power pulsing
	17	LVDS recivers power pulsing
	18	Broadcast Option: if 1 PP is OFF for all, if 0: PP CAN be switched on
0xc117		Take Data , on r/w strobe
0xc118		Reset

0xc119	2-0	Processing mode (001=REDUCE untested, 010= NO REDUCE, 110=JUST_COUNTER, 100=NO_GRAY)
0xc11f	0	Readout speed. If 0=5MHz if 1= 40MHz
	31-16	Configurable delay. Debug only! Keep at 0!
0xc120	0	If 1, take Data, if 0 don't
Adress	Bit	Meaning
0xc2xx		SKIROC CMS
0xc200	--	Load CMS SLCTR
0xc201		MISC. Options
	0	use ADC test input as analouge data (0= off)
	1	AutoOff OTAq (auto OFF = 1)
	2	select external ADC ramp commands (0 use ASIC commands)
	3	ADC ramp slopw (0 = 12 bits, 1 = 10 bits)
	4	Gain selection (internal selection (dig readout) = 0)
	5	40 MHz clock to TOA (1 = On)
	6	RAZ TOA & TOT Internal (1= ON)
	7	RAZ TOA & TOT EXternal (1= ON)
	8	Clock to hold Q in SCA (1= clk_roll, 0= 40 MHz)
	9	Select start readout (1 =1, 0= 2)
	10	bias LVDS TX 1mA (1= ON)
	11	bias LVDS TX 2mA (1= ON)
0xc202	7-0	CHIP ID
0xc203		Enable Components (1= ON)
	0	preamps on
	1	enable G1 slow shaper
	2	enable G10 slow shaper
	3	enable fast shaper
	4	enable TOT discriminator
	5	enable TOT ramp
	6	enable TOT fast ramp
	7	enable TOT slow ramp
	8	enable TOA discriminator
	9	enable TOA ramp
	10	enable Bandgap OTA
	11	enable 10 bit DAC
	12	enable 10 bit DAC2
	13	enable SCA

	14	enable ADC Discriminator (1 on)
	15	enable High-Z output OTA (1 on)
	16	enable probe OTA
	17	enable ADC ramp
	18	enable ADC ramp switch injected charge compensation
	19	Trig TOA Out enabled
	20	Trig TOT Out enabled
	21	End Readout1 enabled
	22	Chip sat enabled
	23	enable Transmit_ON2
	24	enable Transmit_ON1
	25	enable LVDS RollClock reciver
	26	enable LVDS 40MHz_CLK reciver
	27	enable LVDS ValEvt reciver
	28	enable LVDS TRIGExt reciver
	29	enable LVDS RazChan reciver
	30	Enable LVDS DATA Tx
0xc204		Set THRESHOLD
	9-0	10 bit DAC for trigger TOT threshold (LSB (highest) to MSB (lowest))
	19-10	10 bit DAC for trigger TOA threshold (LSB (highest) to MSB (lowest))
0xc205		SHAPER settings
	3-0	LG slow shaper time constant, value (LSB to MSB)*5 ns
	7-4	G10 slow shaper time constant, value (LSB to MSB)*5 ns
	10-8	fast shaper time constant, value (LSB to MSB)*0.625 ns
	11	TOA discriminator polarity (negative =0)
	16-12	leakage current
	17	leakage current polarity (negative =0)
0xc206		Preamp Settings
	0	preamp signal polarity (0= negative, 1= positive)
	6-1	preamp feedback caps, value*62.5 fF LSB (highest) to MSB (lowest)
	14-7	preamp feedback resistors, value*10kΩ LSB (highest) to MSB (lowest)
0xc207		Enable TOA TRIGGER (1= ON)
	31-0	BIT 31 = Channel 63; BIT 0 = Channel 32
0xc208		Enable TOA TRIGGER (1= ON)
	31-0	BIT 31 = Channel 31; BIT 0 = Channel 0
0xc209		Enable TOT TRIGGER (1= ON)
	31-0	BIT 31 = Channel 63; BIT 0 = Channel 32

0xc20a		Enable TOT TRIGGER (1= ON)
	31-0	BIT 31 = Channel 31; BIT 0 = Channel 0
0xc20b		Enable Ctest (0= enabled)
	31-0	BIT 31 = Channel 63; BIT 0 = Channel 32
0xc20c		Enable Ctest (0= enabled)
	31-0	BIT 31 = Channel 31; BIT 0 = Channel 0
0xc20d		Enable PREAMPS (1= ON)
	31-0	BIT 31 = Channel 63; BIT 0 = Channel 32
0xc20e		Enable PREAMPS (1= ON)
	31-0	BIT 31 = Channel 31; BIT 0 = Channel 0
0xc20f		Power Pulsing control; if bit is 0 and broadcast =0: PP ON, else OFF
	0	preamps powerpulsing
	1	disable slow shaper G1 powerpulsing
	2	disable G10 slow shaper powerpulsing
	3	disable fast shaper powerpulsing
	4	disable TOT discriminator powerpulsing
	5	disable TOT ramp powerpulsing
	6	disable TOA discriminator powerpulsing
	7	disable TOA ramp powerpulsing
	8	disable bandgap OTA powerpulsing
	9	disable 10 Bit DAC powerpulsing
	10	disable 10 Bit DAC2 powerpulsing
	11	disable SCA powerpulsing
	12	disable ADC Discriminator powerpulsing
	13	disable High-Z output OTA powerpulsing
	14	disable probe OTA powerpulsing
	15	disable ADC ramp powerpulsing
	16	disable LVDS RollClock reciver powerpulsing
	17	disable LVDS 40MHz_CLK reciver powerpulsing
	18	disable LVDS ValEvt reciver powerpulsing
	19	disable LVDS TRIGExt reciver powerpulsing
	20	disable LVDS RazChan reciver powerpulsing
	21	diabile LVDS DATA Tx powerpulsing
	22	Broadcast Option: if 1 PP is OFF for all, if 0: PP CAN be switched on
0xc210		START Trigger , on r/w strobe
0xc211		Reset
0xc212	2-0	Processing mode (001=REDUCE, 010= NO REDUCE,

		110=JUST_COUNTER, 100=NO_GRAY)
0xc213	15-0	Delay of RollTrigger input in 200MHz ticks
	31-16	Length of Roll Trigger input in 200MHz ticks
0xc214	0	Choose Trigger: 0=SelfTrigger, 1=Trigger from 2A!
	1	Use Roll TriggerMode if 1. (several events per data package)
	5-2	(Events-1) per package in roll mode. Only valid number is 12
0xc215	31-0	AnalogProbe Config: Bitmask Ch.31-0
0xc216	31-0	AnalogProbe Config: Bitmask Ch.63-32
0xc217		GENERELL Config AnalogProbe
	0	Out PA pos
	1	Out PA neg
	2	Out PA hg
	3	Out ssh lg
	4	Out ssh hg
	5	Out fs
	6	Sel probe analog pa
	7	Sel Probe analog pa hg
	8	Sel probe analog ssh
	9	Sel probe analog fs
	10	Sel probe analog ramp
	11	Out TOT
	12	Ramp TOT fast
	13	Ramp TOT slow
	14	Ramp TOA
	15	Out TOA
	16	Out ADC
	17	Startb ramp ADC Int
	18	Out ramp ADC
	19	NC
	20	Enable Analog Probe SLCTR
0xc220	0	If 1, take Data, if 0 don't

C. Additional Figures for Chapter 7

The following figures present the data shown in Fig. 7.7 and Fig. 7.11 for all switch capacitor arrays (SCAs) of the SKIROC ASICs.

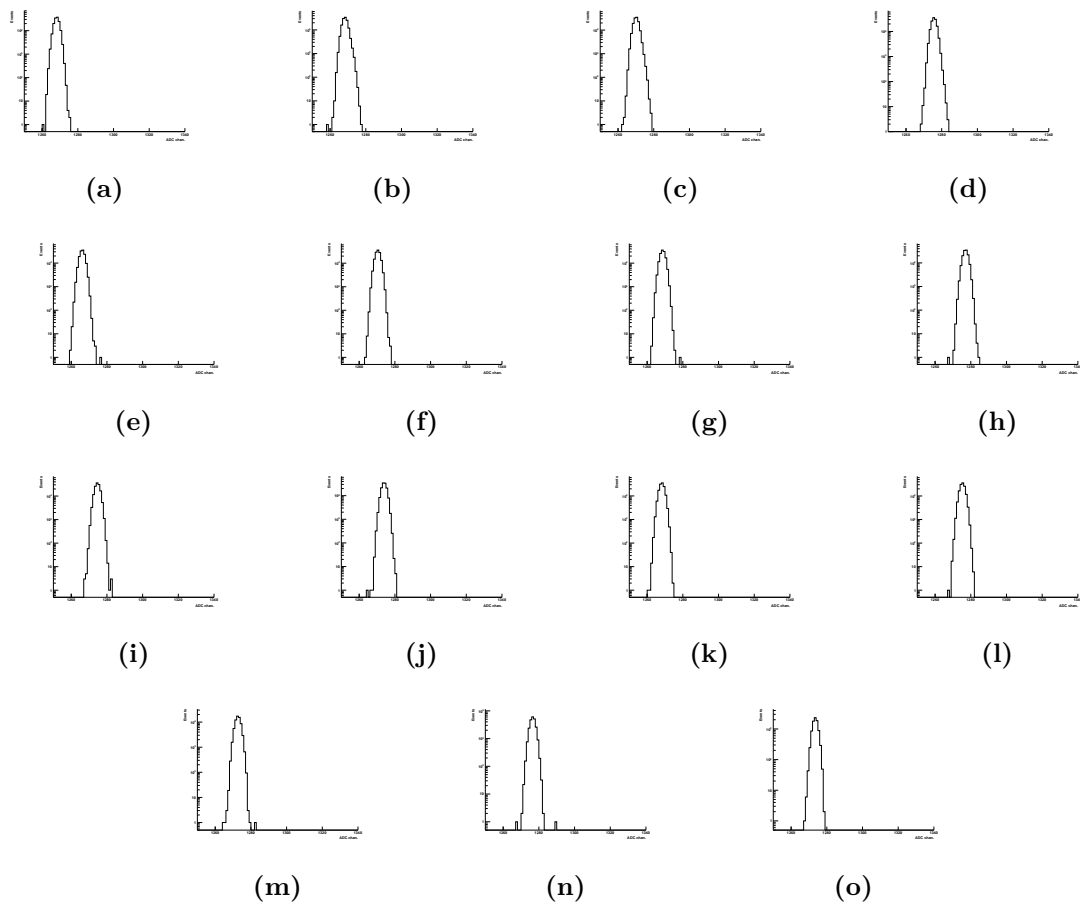


Figure C.1.: The data presented in Fig. 7.7 shown for all SCAs beginning by 0 (panel (a)) to SCA 14 (panel (o)). Shapes and gains are similar for all SCAs.

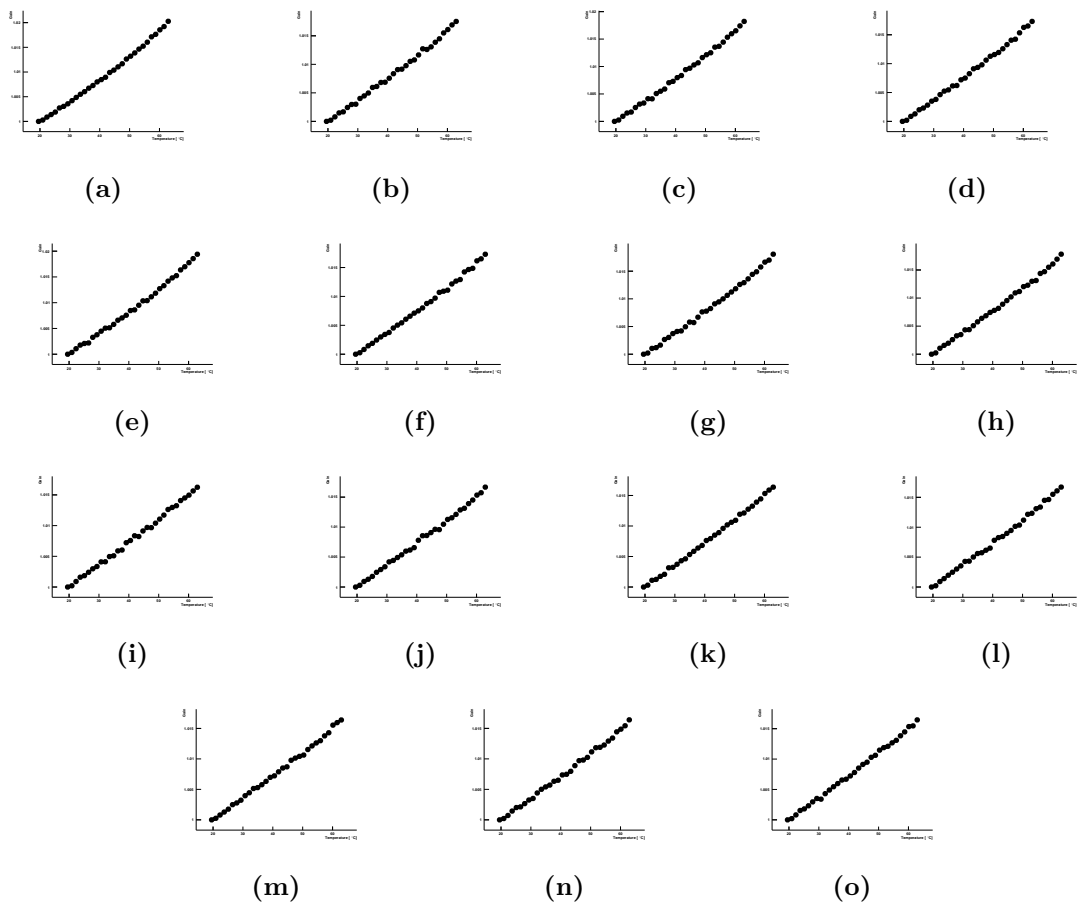


Figure C.2.: The data presented in Fig. 7.11 shown for all SCAs beginning by 0 (panel (a)) to SCA 14 (panel (o)).

Bibliography

- [Ada08] Adamczewski, J.; Essel, H.; Kurz, N. and Linev, S. *Data acquisition backbone core DABC*. Nuclear Science, IEEE Transactions on, 2008. 55, 251–255. doi: 10.1109/TNS.2007.913938.
- [Age18] Agency, I.E. *World Energy Outlook 2018*. 2018. doi: 10.1787/weo-2018-en.
- [Ago03] Agostinelli, S.; Allison, J.; Amako, K.; Apostolakis, J.; Araujo, H.; Arce, P.; Asai, M.; Axen, D.; Banerjee, S.; Barrand, G.; Behner, F.; Bellagamba, L.; Boudreau, J.; Broglia, L.; Brunengo, A.; Burkhardt, H.; Chauvie, S.; Chuma, J.; Chytracsek, R.; Cooperman, G.; Cosmo, G.; Degtyarenko, P.; Dell’Acqua, A.; Depaola, G.; Dietrich, D.; Enami, R.; Feliciello, A.; Ferguson, C.; Fesefeldt, H.; Folger, G.; Foppiano, F.; Forti, A.; Garelli, S.; Giani, S.; Giannitrapani, R.; Gibin, D.; Cadenas, J.G.; González, I.; Abril, G.G.; Greeniaus, G.; Greiner, W.; Grichine, V.; Grossheim, A.; Guatelli, S.; Gumplinger, P.; Hamatsu, R.; Hashimoto, K.; Hasui, H.; Heikkinen, A.; Howard, A.; Ivanchenko, V.; Johnson, A.; Jones, F.; Kallenbach, J.; Kanaya, N.; Kawabata, M.; Kawabata, Y.; Kawaguti, M.; Kelner, S.; Kent, P.; Kimura, A.; Kodama, T.; Kokoulin, R.; Kossov, M.; Kurashige, H.; Lamanna, E.; Lampén, T.; Lara, V.; Lefebure, V.; Lei, F.; Liendl, M.; Lockman, W.; Longo, F.; Magni, S.; Maire, M.; Medernach, E.; Minamimoto, K.; de Freitas, P.M.; Morita, Y.; Murakami, K.; Nagamatu, M.; Nartallo, R.; Nieminen, P.; Nishimura, T.; Ohtsubo, K.; Okamura, M.; O’Neale, S.; Oohata, Y.; Paech, K.; Perl, J.; Pfeiffer, A.; Pia, M.; Ranjard, F.; Rybin, A.; Sadilov, S.; Salvo, E.D.; Santin, G.; Sasaki, T.; Savvas, N.; Sawada, Y.; Scherer, S.; Sei, S.; Sirotenko, V.; Smith, D.; Starkov, N.; Stoecker, H.; Sulkimo, J.; Takahata, M.; Tanaka, S.; Tcherniaev, E.; Tehrani, E.S.; Tropeano, M.; Truscott, P.; Uno, H.; Urban, L.; Urban, P.; Verderi, M.; Walkden, A.; Wander, W.; Weber, H.; Wellisch, J.; Wenaus, T.; Williams, D.; Wright, D.; Yamada, T.; Yoshida, H. and Zschesche, D. *Geant4—a simulation toolkit*. Nuclear Instruments and Methods in Physics Research Section A: Accelerators, Spectrometers, Detectors and Associated Equipment, 2003. 506(3), 250 – 303. ISSN 0168-9002. doi: 10.1016/S0168-9002(03)01368-8.
- [Arm08] Armand, M. and Tarascon, J.M. *Building Better Batteries*. Nature, 2008. 451, 652–7. doi: 10.1038/451652a.
- [Ber20] Berner, C.; Werner, L. and Gernhäuser, R. *HI-TREX - A highly integrated transfer setup at REX-(HIE)ISOLDE*. Nuclear Instruments and Methods in Physics Research Section A: Accelerators, Spectrometers, Detectors and Associated Equipment, 2020. submitted.
- [Bie73] Biersack, J. and Fink, D. *Observation of the blocking effect after $6\text{Li}(n, t)4\text{He}$ reactions with thermal neutrons*. Nuclear Instruments and Methods, 1973. 108(2), 397 – 399. ISSN 0029-554X. doi: 10.1016/0029-554X(73)90621-6.
- [Bie81] Biersack, J.; Fink, D.; Lauch, J.; Henkelmann, R. and Müller, K. *An instrument for lattice location studies of light impurity atoms by means of (n, α) -reactions*. Nuclear

- Instruments and Methods in Physics Research, 1981. 188(2), 411 – 419. ISSN 0167-5087. doi: 10.1016/0029-554X(81)90522-X.
- [Bil12] Bildstein, V.; Gernhauser, R.; Kroll, T.; Krucken, R.; Wimmer, K.; van Duppen, P.; Huyse, M.; Patronis, N. and Raabe, R. *T-REX: A new setup for transfer experiments at REX-ISOLDE*. Eur. Phys. J. A, 2012. 48, 85. doi: 10.1140/epja/i2012-12085-6.
- [Blo33] Bloch, F. *Zur Bremsung rasch bewegter Teilchen beim Durchgang durch Materie*. Annalen der Physik, 1933. 408(3), 285–320. doi: 10.1002/andp.19334080303.
- [Boh39] Bohr, N. and Wheeler, J.A. *The Mechanism of Nuclear Fission*. Phys. Rev., 1939. 56, 426–450. doi: 10.1103/PhysRev.56.426.
- [Bru97] Brun, R. and Rademakers, F. *ROOT - An Object Oriented Data Analysis Framework*. Nuclear Instruments and Methods in Phys. Res. A, 1997. 389, 81 – 86. See also <http://root.cern.ch/>.
- [Buc88] Buck, B. and Merchant, A.C. 1988. 14(10), L211–L216. doi: 10.1088/0305-4616/14/10/002.
- [Cal11] Callier, S.; Dulucq, F.; de La Taille, C.; Martin-Chassard, G. and Seguin-Moreau, N. *SKIROC2, front end chip designed to readout the Electromagnetic CALorimeter at the ILC*. Journal of Instrumentation, 2011. 6(12), C12040.
- [Cau05] Caurier, E.; Martínez-Pinedo, G.; Nowacki, F.; Poves, A. and Zuker, A.P. *The shell model as a unified view of nuclear structure*. Reviews of Modern Physics, 2005. 77(2), 427–488. doi: 10.1103/RevModPhys.77.427.
- [Che09] Chen, H.; Cong, T.N.; Yang, W.; Tan, C.; Li, Y. and Ding, Y. *Progress in electrical energy storage system: A critical review*. Progress in natural science, 2009. 19(3), 291–312.
- [Che18] Chen, C.; Oudenhoven, J.F.; Danilov, D.L.; Vezhlev, E.; Gao, L.; Li, N.; Mulder, F.M.; Eichel, R.A. and Notten, P.H. *Origin of Degradation in Si-Based All-Solid-State Li-Ion Microbatteries*. Advanced Energy Materials, 2018. 8(30), 1801430.
- [Cor09] Coraggio, L.; Covello, A.; Gargano, A.; Itaco, N. and Kuo, T.T.S. *Shell-model calculations and realistic effective interactions*. Progress in Particle and Nuclear Physics, 2009. 62(1), 135–182. doi: 10.1016/j.pnpnp.2008.06.001.
- [Deu95] Deutscher, R.; Florence, T. and Woods, R. *Investigations on an aqueous lithium secondary cell*. Journal of Power Sources, 1995. 55(1), 41 – 46. ISSN 0378-7753. doi: [https://doi.org/10.1016/0378-7753\(94\)02166-Z](https://doi.org/10.1016/0378-7753(94)02166-Z).
- [Dia03] Dianoux, A.J. and Lander, G. *Neutron Data Booklet, Second edition*, 2003.
URL https://www.ill.eu/fileadmin/users_files/documents/links/documentation/NeutronDataBooklet.pdf
- [Dow93] Downing, R.G.; Lamaze, G.P.; Langland, J.K. and Hwang, S.T. *Neutron Depth Profiling: Overview and Description of NIST Facilities*. Journal of Research of the National Institute of Standards and Technology, 1993. 98, 109–126. doi: 10.6028/jres.098.008.
- [Dow95] Downing, R.G. and Lamaze, G.P. *Near-surface profiling of semiconductor materials using neutron depth profiling*. Semiconductor Science and Technology, 1995. 10(11), 1423.

- [Dun11] Dunn, B.; Kamath, H. and Tarascon, J.M. *Electrical Energy Storage for the Grid: A Battery of Choices*. Science, 2011. 334(6058), 928–935. ISSN 0036-8075. doi: 10.1126/science.1212741.
- [Eft01] Eftekhari, A. *Electrochemical behavior of thin-film LiMn_2O_4 electrode in aqueous media*. Electrochimica Acta, 2001. 47(3), 495 – 499. ISSN 0013-4686. doi: 10.1016/S0013-4686(01)00774-5.
- [Fin73] Finch, E. and Rodgers, A. *Measurements of the pulse height defect and its mass dependence for heavy-ion silicon detectors*. Nuclear Instruments and Methods, 1973. 113(1), 29 – 40. ISSN 0029-554X. doi: 10.1016/0029-554X(73)90474-6.
- [For05] Fortunato, L. and Vitturi, A. *Electromagnetic response and breakup of light weakly bound nuclei in a dicluster model*. The European Physical Journal A - Hadrons and Nuclei, 2005. 26(1), 33–40. ISSN 1434-601X. doi: 10.1140/epja/i2005-10118-y.
- [Fra20] Frankenberger, M.; Trunk, M.; Seidlmayer, S.; Dinter, A.; Dittloff, J.; Werner, L.; Gernhäuser, R.; Revay, Z.; Märkisch, B.; Gilles, R. et al. *SEI Growth Impacts of Lamination, Formation and Cycling in Lithium Ion Batteries*. Batteries, 2020. 6(2), 21.
- [Fre01] French, M.; Jones, L.; Morrissey, Q.; Neviani, A.; Turchetta, R.; Fulcher, J.; Hall, G.; Noah, E.; Raymond, M.; Cervelli, G.; Moreira, P. and Marseguerra, G. *Design and results from the APV25, a deep sub-micron CMOS front-end chip for the CMS tracker*. Nuclear Instruments and Methods in Physics Research Section A: Accelerators, Spectrometers, Detectors and Associated Equipment, 2001. 466(2), 359 – 365. ISSN 0168-9002. doi: 10.1016/S0168-9002(01)00589-7. 4th Int. Symp. on Development and Application of Semiconductor Tracking Detectors.
- [Gas08] Gasson, P.C. *The Superalloys: Fundamentals and Applications*, volume 112. Cambridge University Press, 2008. ISBN 0-521-85904-2. doi: 10.1017/S0001924000087509.
- [Gun76] Gunson, J. and Polychronopoulos, B. *Optimum design of a coded mask x-ray telescope for rocket applications*. Monthly Notices of the Royal Astronomical Society, 1976. 177(3), 485–497.
- [Han19] Han, F.; Westover, A.S.; Yue, J.; Fan, X.; Wang, F.; Chi, M.; Leonard, D.N.; Dudney, N.J.; Wang, H. and Wang, C. *High electronic conductivity as the origin of lithium dendrite formation within solid electrolytes*. Nature Energy, 2019. 4(3), 187.
- [Hav93] Havranek, V.; Hnatowicz, V.; Kvitek, J.; Vacik, J.; Hoffmann, J. and Fink, D. *Neutron depth profiling by large angle coincidence spectrometry*. Nuclear Instruments and Methods in Physics Research Section B: Beam Interactions with Materials and Atoms, 1993. 73(4), 523–530.
- [Hax49] Haxel, O.; Jensen, J.H.D. and Suess, H.E. *On the "Magic Numbers" in Nuclear Structure*. Phys. Rev., 1949. 75, 1766–1766. doi: 10.1103/PhysRev.75.1766.2.
- [He15a] He, Y.; Downing, R.G. and Wang, H. *3D mapping of lithium in battery electrodes using neutron activation*. Journal of Power Sources, 2015. 287, 226–230.
- [He15b] He, Y.; Downing, R.G. and Wang, H. *3D mapping of lithium in battery electrodes using neutron activation*. Journal of Power Sources, 2015. 287, 226 – 230. ISSN 0378-7753. doi: 10.1016/j.jpowsour.2015.03.176.

- [Hun39] Hunt, F. and Hickman, R. *On electronic voltage stabilizers*. Review of scientific Instruments, 1939. 10(1), 6–21.
- [Ibr08] Ibrahim, H.; Ilinca, A. and Perron, J. *Energy storage systems—Characteristics and comparisons*. Renewable and Sustainable Energy Reviews, 2008. 12(5), 1221 – 1250. ISSN 1364-0321. doi: 10.1016/j.rser.2007.01.023.
- [Kan06] Kang, K.; Meng, Y.S.; Bréger, J.; Grey, C.P. and Ceder, G. *Electrodes with High Power and High Capacity for Rechargeable Lithium Batteries*. Science, 2006. 311(5763), 977–980. ISSN 0036-8075. doi: 10.1126/science.1122152.
- [Kaw07] Kawabata, T.; Akimune, H.; Fujita, H.; Fujita, Y.; Fujiwara, M.; Hara, K.; Hatanaka, K.; Itoh, M.; Kanada-En'yo, Y.; Kishi, S.; Nakanishi, K.; Sakaguchi, H.; Shimbara, Y.; Tamii, A.; Terashima, S.; Uchida, M.; Wakasa, T.; Yasuda, Y.; Yoshida, H. and Yosoi, M. *$2\alpha+t$ cluster structure in $11B$* . Physics Letters B, 2007. 646(1), 6 – 11. ISSN 0370-2693. doi: 10.1016/j.physletb.2006.11.079.
- [Kaw08] Kawabata, T.; Sasamoto, Y.; Fujiwara, M.; Hashimoto, H.; Hatanaka, K.; Itoh, K.; Itoh, M.; Kanada-En'yo, Y.; Kawase, K.; Maeda, Y. et al. *Cluster states in $11B$ and $13C$* . 2008. 111(1), 012013.
- [Ket13] Ketzer, B. *A time projection chamber for high-rate experiments: Towards an upgrade of the ALICE TPC*. Nuclear Instruments and Methods in Physics Research Section A: Accelerators, Spectrometers, Detectors and Associated Equipment, 2013. 732, 237 – 240. ISSN 0168-9002. doi: <https://doi.org/10.1016/j.nima.2013.08.027>. Vienna Conference on Instrumentation 2013.
- [Kim14] Kim, H.; Hong, J.; Park, K.Y.; Kim, H.; Kim, S.W. and Kang, K. *Aqueous rechargeable Li and Na ion batteries*. Chemical reviews, 2014. 114(23), 11788–11827.
- [Kno00] Knoll, G. *Radiation Detection and Measurement*. John Wiley & Sons, Inc., New York, third edition, 2000. ISBN 0-471-07338-5.
- [Kol98] Kolarova, P.; Vacik, J.; Spirkova-Hradilova, J. and Cervena, J. *Neutron depth profiling study of lithium niobate optical waveguides*. Nuclear Instruments and Methods in Physics Research Section B: Beam Interactions with Materials and Atoms, 1998. 141(1-4), 498–500.
- [Kor] Korcyl, G.; Maier, L.; Michel, J.; Neiser, A.; Palka, M.; Penschuck, M.; Strzempek, P.; Traxler, M. and Ugur, C. *A Users Guide to the TRB3 and FPGA-TDC Based Platforms*. URL <http://trb.gsi.de/>
- [Krz08] Krzemien, W.; Frohlich, I.; Kajetanowicz, M.; Korcyl, K.; Palka, M.; Salabura, P.; Schrader, C.; Skott, P.; Strobele, H.; Stroth, J.; Tarantola, A.; Traxler, M. and Trebacz, R. *The TRB for HADES and FAIR experiments at GSI*. 2008. URL <https://arxiv.org/abs/0810.4723>
- [Lee04] Lee, J.W. and Pyun, S.I. *Investigation of lithium transport through $LiMn_2O_4$ film electrode in aqueous $LiNO_3$ solution*. Electrochimica Acta, 2004. 49(5), 753 – 761. ISSN 0013-4686. doi: <https://doi.org/10.1016/j.electacta.2003.09.029>.

- [Len86] Lennard, W.; Geissel, H.; Winterbon, K.; Phillips, D.; Alexander, T. and Forster, J. *Nonlinear response of Si detectors for low-Z ions*. Nuclear Instruments and Methods in Physics Research Section A: Accelerators, Spectrometers, Detectors and Associated Equipment, 1986. 248(2), 454 – 460. ISSN 0168-9002. doi: 10.1016/0168-9002(86)91033-8.
- [Len87] Lennard, W. and Winterbon, K. *Response of silicon detectors to 1H and 4He ions*. Nuclear Instruments and Methods in Physics Research Section B: Beam Interactions with Materials and Atoms, 1987. 24-25, 1035 – 1038. ISSN 0168-583X. doi: 10.1016/S0168-583X(87)80306-3.
URL <http://www.sciencedirect.com/science/article/pii/S0168583X87803063>
- [Li94] Li, W.; Dahn, J.R. and Wainwright, D.S. *Rechargeable Lithium Batteries with Aqueous Electrolytes*. Science, 1994. 264(5162), 1115–1118. ISSN 0036-8075. doi: 10.1126/science.264.5162.1115.
- [Li15] Li, R.d.; Yang, X.; Wang, G.b.; Dou, H.f.; Qian, D.z. and Wang, S.y. *Development of neutron depth profiling at CMRR*. Nuclear Instruments and Methods in Physics Research Section A: Accelerators, Spectrometers, Detectors and Associated Equipment, 2015. 788, 1–4.
- [Lia19] Liang, Z. *Construction of the new silicon microstrips tracker for the Phase-II ATLAS detector*. Nuclear Instruments and Methods in Physics Research Section A: Accelerators, Spectrometers, Detectors and Associated Equipment, 2019. 924, 265 – 269. ISSN 0168-9002. doi: 10.1016/j.nima.2018.09.014. 11th International Hiroshima Symposium on Development and Application of Semiconductor Tracking Detectors.
- [Lin20] Linsenmann, F.; Trunk, M.; Rapp, P.; Werner, L.; Gernhäuser, R.; Gilles, R.; Märkisch, B.; Revay, Z. and Gasteiger, H. *A Liquid Electrolyte-Based Lithium-Ion Battery Cell Design for Operando Neutron Depth Profiling*. Journal of the Electrochemical Society, 2020.
- [Liu14] Liu, D.X.; Wang, J.; Pan, K.; Qiu, J.; Canova, M.; Cao, L.R. and Co, A.C. *In situ quantification and visualization of lithium transport with neutrons*. Angewandte Chemie International Edition, 2014. 53(36), 9498–9502.
- [Liu16] Liu, D.X.; Cao, L.R. and Co, A.C. *Demonstrating the Feasibility of Al as Anode Current Collector in Li-Ion Batteries via In Situ Neutron Depth Profiling*. Chemistry of Materials, 2016. 28(2), 556–563.
- [Luo07] Luo, J.Y. and Xia, Y.Y. *Aqueous Lithium-ion Battery $\text{LiTi}_2(\text{PO}_4)_3/\text{LiMn}_2\text{O}_4$ with High Power and Energy Densities as well as Superior Cycling Stability***. Advanced Functional Materials, 2007. 17(18), 3877–3884. doi: 10.1002/adfm.200700638.
- [Lut17] Lutter, R.; Schaile, O.; Schoeffel, K.; K.Steinberger and Broude, C. *MARaBOU: MBS And Root based Online Offline Utility*, 2017.
URL <http://www.bl.physik.tu-muenchen.de/marabou/htmldoc/>
- [Lv18] Lv, S.; Verhallen, T.; Vasileiadis, A.; Ooms, F.; Xu, Y.; Li, Z.; Li, Z. and Wagemaker, M. *Operando monitoring the lithium spatial distribution of lithium metal anodes*. Nature communications, 2018. 9(1), 2152.

- [Mal19] Malzacher, P.; Iwasa, N. and Weick, H. *ATIMA*, 2019.
URL <https://web-docs.gsi.de/~weick/atima/>
- [Man06] Manickam, M.; Singh, P.; Thurgate, S. and Prince, K. *Redox behavior and surface characterization of LiFePO₄ in lithium hydroxide electrolyte*. *Journal of Power Sources*, 2006. 158(1), 646 – 649. ISSN 0378-7753. doi: <https://doi.org/10.1016/j.jpowsour.2005.08.059>.
- [Man11] Manjunatha, H.; Venkatesha, T. and Suresh, G. *Kinetics of electrochemical insertion of lithium ion into LiFePO₄ from aqueous 2M Li₂SO₄ solution studied by potentiostatic intermittent titration technique*. *Electrochimica Acta*, 2011. 58, 247 – 257. ISSN 0013-4686. doi: <https://doi.org/10.1016/j.electacta.2011.09.041>.
- [Mar] Marzak, P.; Moser, P.; Schreier, S.; Scieszka, D.; Yun, J.; Schneider, O. and Bandarenka, A.S. *A Cell for Controllable Formation and In Operando Electrochemical Characterization of Intercalation Materials for Aqueous Metal-Ion Batteries*. *Small Methods*. n/a(n/a), 1900445. doi: 10.1002/smt.201900445.
- [Mei39] Meitner, L. and Frisch, O. *The Mechanism of Nuclear Fission*. *Nature*, 1939. 143, 471–472. doi: 10.1038/143471a0.
- [Mic] Michel, J.; Adamczewski-Musch, J.; Böhmer, M.; Korcyl, G.; Palka, M.; Yurevich, S. and Traxler, M. *A Users Guide to the HADES DAQ System*.
URL <http://trb.gsi.de/>
- [Mil96] Miller, S. *Advanced materials mean advanced engines*. *Interdisciplinary Science Reviews*, 1996. 21(2), 117–129. doi: 10.1179/isr.1996.21.2.117.
- [MK84] Mayer-Kuckuk, T. *Kernphysik*. Teubner Studienbücher, Stuttgart, 1984.
- [Mol95] Moller, P.; Nix, J.; Myers, W. and Swiatecki, W. *Nuclear Ground-State Masses and Deformations*. *Atomic Data and Nuclear Data Tables*, 1995. 59(2), 185 – 381. ISSN 0092-640X. doi: 10.1006/adnd.1995.1002.
- [Möl09] Möller, P.; Sierk, A.J.; Ichikawa, T.; Iwamoto, A.; Bengtsson, R.; Uhrenholt, H. and Åberg, S. *Heavy-element fission barriers*. *Phys. Rev. C*, 2009. 79, 064304. doi: 10.1103/PhysRevC.79.064304.
- [Muk10] Mukherji, D.; Strunz, P.; Gilles, R.; Hofmann, M.; Schmitz, F. and Rösler, J. *Investigation of phase transformations by in-situ neutron diffraction in a Co–Re-based high temperature alloy*. *Materials Letters*, 2010. 64(23), 2608 – 2611. ISSN 0167-577X. doi: 10.1016/j.matlet.2010.08.066.
- [Muk12] Mukherji, D.; Rösler, J.; Krüger, M.; Heilmaier, M.; Bölit, M.C.; Völkl, R.; Glatzel, U. and Szentmiklósi, L. *The effects of boron addition on the microstructure and mechanical properties of Co–Re-based high-temperature alloys*. *Scripta Materialia*, 2012. 66(1), 60 – 63. ISSN 1359-6462. doi: <https://doi.org/10.1016/j.scriptamat.2011.10.007>.
- [Muk14] Mukherji, D.; Gilles, R.; Karge, L.; Strunz, P.; Beran, P.; Eckerlebe, H.; Stark, A.; Szentmiklósi, L.; Mácsik, Z.; Schumacher, G.; Zizak, I.; Hofmann, M.; Hoelzel, M. and Rösler, J. *Neutron and synchrotron probes in the development of Co–Re-based alloys for next generation gas turbines with an emphasis on the influence of boron additives*. *Journal of Applied Crystallography*, 2014. 47(4), 1417–1430. doi: 10.1107/S1600576714013624.

- [Mul12] Mulligan, P.; Cao, L. and Turkoglu, D. *A multi-detector, digitizer based neutron depth profiling device for characterizing thin film materials*. Review of Scientific Instruments, 2012. 83(7), 073303.
- [Nis79] Nishioka, H.; Saito, S. and Yasuno, M. *Structure Study of $2\alpha+t$ System by the Orthogonality Condition Model**. Progress of Theoretical Physics, 1979. 62(2), 424–439. ISSN 0033-068X. doi: 10.1143/PTP.62.424.
- [NK18] Nikolaus Kurz, Jörn Adamczewski-Musch, G. *Multi-Branch-System, MBS*, 2018.
URL <https://www.gsi.de/work/forschung/experimentelektronik/datenverarbeitung/datenerfassung/mbs.htm>
- [Oer06] von Oertzen, W.; Freer, M. and Kanada-En'yo, Y. *Nuclear clusters and nuclear molecules*. Physics Reports, 2006. 432(2), 43 – 113. ISSN 0370-1573. doi: 10.1016/j.physrep.2006.07.001.
- [Par14] Park, B.; Sun, G. and Choi, H. *Development of cold neutron depth profiling system at HANARO*. Nuclear Instruments and Methods in Physics Research Section A: Accelerators, Spectrometers, Detectors and Associated Equipment, 2014. 752, 20–26.
- [Per09] Perepezko, J.H. *The Hotter the Engine, the Better*. Science, 2009. 326(5956), 1068–1069. ISSN 0036-8075. doi: 10.1126/science.1179327.
- [Por17] Portenkirchner, E.; Neri, G.; Lichtinger, J.; Brumbarov, J.; Rudiger, C.; Gernhäuser, R. and Kunze-Liebhauser, J. *Tracking areal lithium densities from neutron activation - quantitative Li determination in self-organized TiO₂ nanotube anode materials for Li-ion batteries*. Phys. Chem. Chem. Phys., 2017. 19, 8602–8611. doi: 10.1039/C7CP00180K.
- [Pri11] Pritychenko, B.; Běták, E.; Kellett, M.; Singh, B. and Totans, J. *The Nuclear Science References (NSR) database and Web Retrieval System*. Nuclear Instruments and Methods in Physics Research Section A: Accelerators, Spectrometers, Detectors and Associated Equipment, 2011. 640(1), 213 – 218. ISSN 0168-9002. doi: 10.1016/j.nima.2011.03.018.
- [Res19] Resmi, P.K. *Construction and quality assurance of the Belle II Silicon Vertex Detector*. arXiv e-prints, 2019. arXiv:1901.09549.
- [Rev15] Revay, Z.; Kudejova, P.; Kleszcz, K.; Söllradl, S. and Genreith, C. *In-beam activation analysis facility at MLZ, Garching*. Nuclear Instruments and Methods in Physics Research Section A Accelerators Spectrometers Detectors and Associated Equipment, 2015. 799, 114–123.
- [Sau08] Sauvage, F.; Laffont, L.; Tarascon, J.M. and Baudrin, E. *Factors affecting the electrochemical reactivity vs. lithium of carbon-free LiFePO₄ thin films*. Journal of Power Sources, 2008. 175(1), 495 – 501. ISSN 0378-7753. doi: <https://doi.org/10.1016/j.jpowsour.2007.09.085>.
- [Sly04] Slyusar, V. *A method of investigation of the linear dynamic range of reception channels in a digital antenna array*. Radioelectronics and Communications Systems, 2004. 47(9), 20–25. ISSN 1934-8061.
- [Sol11] Soloveichik, G.L. *Battery Technologies for Large-Scale Stationary Energy Storage*. Annual Review of Chemical and Biomolecular Engineering, 2011. 2(1), 503–527. doi: 10.1146/annurev-chembioeng-061010-114116. PMID: 22432629.

- [Tan13] Tang, W.; Zhu, Y.; Hou, Y.; Liu, L.; Wu, Y.; Loh, K.P.; Zhang, H. and Zhu, K. *Aqueous rechargeable lithium batteries as an energy storage system of superfast charging*. Energy Environ. Sci., 2013. 6, 2093–2104. doi: 10.1039/C3EE24249H.
- [Tar01] Tarascon, J. and Armand, M. *Issues and Challenges Facing Rechargeable Lithium Batteries*. Nature, 2001. 414, 359–67. doi: 10.1038/35104644.
- [Til02] Tilley, D.; Cheves, C.; Godwin, J.; Hale, G.; Hofmann, H.; Kelley, J.; Sheu, C. and Weller, H. *Energy levels of light nuclei $A=5, 6, 7$* . Nuclear Physics A, 2002. 708(1), 3 – 163. ISSN 0375-9474. doi: [https://doi.org/10.1016/S0375-9474\(02\)00597-3](https://doi.org/10.1016/S0375-9474(02)00597-3).
- [Tom17] Tomandl, I.; Vacík, J.; Mora Sierra, Y.; Granja, C. and Kraus, V. *High resolution imaging of 2D distribution of lithium in thin samples measured with multipixel detectors in sandwich geometry*. Review of Scientific Instruments, 2017. 88(2), 023706. doi: 10.1063/1.4977217.
- [Ton97] Tonelli, G. *The silicon tracking system of CMS*. Nuclear Instruments and Methods in Physics Research Section A: Accelerators, Spectrometers, Detectors and Associated Equipment, 1997. 386(1), 129 – 137. ISSN 0168-9002. doi: 10.1016/S0168-9002(96)01106-0. Proceedings of the 5th International Workshop on Vertex Detectors.
- [Tru18] Trunk, M.; Wetjen, M.; Werner, L.; Gernhäuser, R.; Märkisch, B.; Revay, Z.; Gasteiger, H. and Gilles, R. *Materials science applications of Neutron Depth Profiling at the PGAA facility of Heinz Maier-Leibnitz Zentrum*. Materials Characterization, 2018. 146, 127 – 134. ISSN 1044-5803. doi: 10.1016/j.matchar.2018.09.030.
- [Ube03] Ubertini, P.; Lebrun, F.; Di Cocco, G.; Bazzano, A.; Bird, A.; Broenstad, K.; Goldwurm, A.; La Rosa, G.; Labanti, C.; Laurent, P. et al. *IBIS: The Imager on-board INTEGRAL*. Astronomy & Astrophysics, 2003. 411(1), L131–L139.
- [Ver18] Verhallen, T.W.; Lv, S. and Wagemaker, M. *Operando Neutron Depth Profiling to Determine the Spatial Distribution of Li in Li-ion Batteries*. Frontiers in Energy Research, 2018. 6, 62.
- [Wal85] Walliser, H. and Fliessbach, T. *Cluster picture of ${}^7\text{Li}$* . Phys. Rev. C, 1985. 31, 2242–2250. doi: 10.1103/PhysRevC.31.2242.
- [Wer18] Werner, L.; Trunk, M.; Gernhäuser, R.; Gilles, R.; Märkisch, B. and Revay, Z. *The new neutron depth profiling instrument N_4DP at the Heinz Maier-Leibnitz Zentrum*. Nuclear Instruments and Methods in Physics Research Section A: Accelerators, Spectrometers, Detectors and Associated Equipment, 2018. 911, 30 – 36. ISSN 0168-9002. doi: 10.1016/j.nima.2018.09.113.
- [Wes11] Wessells, C.D.; Peddada, S.V.; McDowell, M.T.; Huggins, R.A. and Cui, Y. *The effect of insertion species on nanostructured open framework hexacyanoferrate battery electrodes*. Journal of the Electrochemical Society, 2011. 159(2), A98–A103.
- [Wet18a] Wetjen, M.; Solchenbach, S.; Pritzl, D.; Hou, J.; Tileli, V. and Gasteiger, H.A. *Morphological Changes of Silicon Nanoparticles and the Influence of Cutoff Potentials in Silicon-Graphite Electrodes*. Journal of The Electrochemical Society, 2018. 165(7), A1503–A1514. doi: 10.1149/2.1261807jes.

- [Wet18b] Wetjen, M.; Trunk, M.; Werner, L.; Gernhäuser, R.; Märkisch, B.; Revay, Z.; Gilles, R. and Gasteiger, H.A. *Quantifying the Distribution of Electrolyte Decomposition Products in Silicon-Graphite Electrodes by Neutron Depth Profiling*. Journal of The Electrochemical Society, 2018. 165, A2340 – A2348. ISSN 10. doi: 10.1149/2.1341810jes.
- [Wet19] Wetjen, Morten and Trunk, Markus and Werner, Lukas and Gasteiger, Hubert A. and Gernhäuser, Roman and Gilles, Ralph and Märkisch, Bastian and Révay, Zsolt. *Monitoring the Lithium Concentration across the Thickness of Silicon-Graphite Electrodes during the First (De-)Lithiation*. Journal of The Electrochemical Society, 2019. 166(8), A1408–A1411. doi: 10.1149/2.0581908jes.
- [Win98] Winter, M.; Besenhard, J.; Spahr, M. and Novak, P. *Insertion electrode materials for rechargeable lithium batteries*. Advanced Materials, 1998. 10, 725–725. ISSN 0935-9648.
- [Yan11] Yang, Z.; Zhang, J.; Kintner-Meyer, M.C.W.; Lu, X.; Choi, D.; Lemmon, J.P. and Liu, J. *Electrochemical Energy Storage for Green Grid*. Chemical Reviews, 2011. 111(5), 3577–3613. doi: 10.1021/cr100290v. PMID: 21375330.
- [Zie72] Ziegler, J.F.; Crowder, B.L.; Cole, G.W.; Baglin, J.E.E. and Masters, B.J. *Boron atom distributions in ion-implanted silicon by the ($n,^4\text{He}$) nuclear reaction*. Applied Physics Letters, 1972. 21, 16–17. doi: 10.1063/1.1654197.
- [Zie04] Ziegler, J.F. *SRIM-2003*. Nuclear Instruments and Methods in Physics Research Section B: Beam Interactions with Materials and Atoms, 2004. 219-220, 1027 – 1036. ISSN 0168-583X. doi: 10.1016/j.nimb.2004.01.208. Proceedings of the Sixteenth International Conference on Ion Beam Analysis.